Transverse Optical Magnetism

by

William Fisher

A dissertation submitted in partial fulfillment
of the requirements for the degree of
Doctor of Philosophy
(Applied Physics)
in The University of Michigan
2012

Doctoral Committee:
Professor Stephen C. Rand, Chair
Professor Roy Clarke
Professor Noel C. Perkins
Research Scientist John A. Nees

To Granddad - an engineer born a bit too soon
Derek Blume - always tinker

Acknowledgments

Meredith - For letting me complain about grading and everything else in graduate school

My parents - For putting up with my persistence to study physics

The Applied Theory Group

Forrest Doss - For general mathematical brilliance and discussions

Franklin Dollar - For data from the Hercules laser

The Applied Physics Program - For supporting me financially when money was tight

Prof Wehe - For supporting our research from across the street

The Committee - For taking the time to read my work

Prof Rand - For allowing me to explore tangents and all your support

Table of Contents

List of Tables

Table

List of Figures

Figure

List of Appendices

Appendix

Abstract

This thesis reports the first observations and theory of transverse magnetic response at optical frequencies under non-relativistic conditions. The nonlinear optical process responsible for magnetic dipole scattering is identified and analyzed with classical and quantum treatments. The intensity dependence of nonlinear magnetic dipole scattering is found to be quadratic in a centrosymmetric liquid, indicating that this must be a new nonlinear effect not described by traditional nonlinear optics. Contrary to standard treatments of non-relativistic, nonlinear optics, strong effects due to the optical magnetic field are predicted and verified experimentally. Saturation behavior of the magneto-electric response is measured in carbon tetrachloride, water, and benzene well below the threshold of relativistic optics and is shown to depend on their molecular structure. Magnetic saturation intensities of these three liquids are reported here for the first time.

Several mutually consistent theoretical descriptions of Transverse Optical Magnetism are developed. The classical Lorentz Oscillator Model is extended to include Lorentz forces and the equations of motion are solved perturbatively to establish that second order dynamics result from their inclusion. It is found that the equations of motion support unstable motion and are expressible as a system of sinusoidally coupled Mathieu equations. Quantum mechanical theories based on the density matrix and Heisenberg formalisms are also presented. The quantum mechanical results agree quantitatively with the classical theory.

Thus, a new class of nonlinear optical phenomena is uncovered, and in particular, magneto-electric optical rectification is foreseen. If used in the transient regime with pulsed sources this effect holds promise for generating intense terahertz radiation in unbiased dielectrics. This effect is also capable of producing a static voltage and analysis is presented showing that it may be useful for laser beam energy conversion or for solar power generation. With numerical modeling this interaction is shown to be robust enough to be potentially efficient even for incoherent light sources like the sun.

Chapter 1
Introduction

The goal of this thesis is to expand the model of the interaction of light and matter in the non-relativistic regime to include the action of the magnetic field of the light and present the first experimental observations of nonlinearities due to the optical magnetic field. The need for a concise model began with the observation of strong magnetic dipole scattering reported by Oliveira [1][2]. This thesis therefore develops classical and quantum models, and makes detailed comparisons with the first experiments on this topic. Non-relativistic magneto-electric optical effects have not previously been measured due to the perpendicular geometry necessary to observe them, unexpected requirements for material symmetry, and the need for intermediate optical intensities that have been of little recent interest.

The perpendicular geometry used for the present experiments is uncommon in coherent nonlinear optics because no beam can form at right angles to the input light. If one searched for magnetic dipole effects in the forward direction, no conclusion could be reached. The polarization and frequency of coherent electric dipole (ED) and magnetic dipole (MD) responses are indistinguishable in the forward direction. This is expanded upon and exploited in Chapter 3 to exclude the possibility of observing mixed electric and magnetic signals. The symmetry requirements of magnetic processes are different than those of electric processes due to the axial nature of the magnetic field. Second order polarizations are not possible in centrosymmetric media, whereas second order magnetizations are allowed. Finally, the intensity regime of the experiments reported here has been considered to be too low to be of current interest. The process of Transverse Optical Magnetism reaches saturation in the range of 10^7 to $10^{10} W/cm^2$ in the materials studied as part of this dissertation. This regime is below the threshold for electric-field-based nonlinear effects in most materials yet much higher than the typical intensity range for linear effects. It is also beyond the capability of most continuous wave (CW) sources, even with strong focusing, but is only a fraction of the peak intensity of modern Chirped Pulse Amplified laser systems. Thus, many laboratories either exploit the stability and narrow bandwidth of CW systems, or the high peak intensity and wide bandwidth capabilities of femtosecond laser systems. This combination of factors

has apparently deterred prior detection of non-relativistic magnetic effects at optical frequencies. The implications of this work therefore include a large number of new nonlinear optical effects, new methods of terahertz radiation and solar power generation, and relevance to pre-pulse interactions in high-field physics.

While geometric optics has been studied and understood for thousands of years, quantitative models of the nature and effect of light have only been developed in the last 150 years. The work of James Clerk Maxwell showed that light is the oscillation of electric and magnetic fields and H.A. Lorentz developed the early classical theory of light-matter interaction [3] [4]. Quantitative descriptions of optics developed rapidly, particularly in the years after the invention of the laser, into the pervading and useful field we know today. Modern optics spans a wide range of wavelengths, interaction times, and intensities from single photon interaction to laser pulses so intense that they accelerate charges to nearly the speed of light. The extension of the original basic models into new regimes has worked remarkably well over this vast set of regimes but has also engrained a set of assumptions into several generations of scientists. It is one of these assumptions, that the magnetic field of light is too small to effect the dynamics at non-relativistic intensities [5], that is explored in this dissertation.

1.1 Wave Nature of Light

The small magnitude of the magnetic component of a plane wave relative to the electric component can be established by deriving the spatial and temporal dependences of the electric and magnetic fields. In the absence of charges, Maxwell's equations take the form

$$\nabla \times \vec{E} = -\mu_0 \frac{\partial \vec{H}}{\partial t} \tag{1.1}$$

$$\nabla \times \vec{H} = \varepsilon_0 \frac{\partial \vec{E}}{\partial t} \tag{1.2}$$

$$\nabla \cdot \vec{E} = 0 \tag{1.3}$$

$$\nabla \cdot \vec{H} = 0 \tag{1.4}$$

These equations can be put into the form of wave equations for the electric field and the magnetic field. Taking the curl of (1.1) and the time derivative of (1.2) and vise versa results

in

$$\nabla \times (\nabla \times \vec{E}) = -\mu_0 \varepsilon_0 \frac{\partial^2 \vec{E}}{\partial t^2} \tag{1.5}$$

$$\nabla \times (\nabla \times \vec{H}) = -\mu_0 \varepsilon_0 \frac{\partial^2 \vec{H}}{\partial t^2} \tag{1.6}$$

Using the vector identity and Eqs. (1.3) and (1.4)

$$\nabla \times (\nabla \times \vec{X}) = \nabla(\nabla \cdot \vec{X}) - \nabla^2 \vec{X} \tag{1.7}$$

we obtain

$$\nabla^2 \vec{E} = \frac{1}{c^2} \frac{\partial^2 \vec{E}}{\partial t^2} \tag{1.8}$$

$$\nabla^2 \vec{H} = \frac{1}{c^2} \frac{\partial^2 \vec{H}}{\partial t^2} \tag{1.9}$$

where $c = (\mu_0 \varepsilon_0)^{-1/2}$ is the speed of propagation of the wave, or, the speed of light. Thus, both the electric and the magnetic field obey a wave equation in free space. A solution to the wave equations is the plane wave where the fields are given by the expressions

$$\vec{E} = \vec{E}_0 e^{i(\vec{k}\cdot\vec{r} - \omega t)} \tag{1.10}$$

$$\vec{H} = \vec{H}_0 e^{i(\vec{k}\cdot\vec{r} - \omega t)} \tag{1.11}$$

$$\vec{E} \times \vec{H} \propto \vec{k} \tag{1.12}$$

This solution shows that the light can be linearly polarized and that in this case the direction of propagation, the electric field, and the magnetic field are perpendicular. The relative magnitude of the electric and magnetic fields may be found directly from Eq. (1.2) by substitution of Eqs. (1.10) and (1.11): $B = \mu_0 H = E/c$.

1.2 Electric Interaction of Light and Matter

Accurate modeling of the interaction of bound electrons with light requires a quantum mechanical description. However, if the light is non-resonant, a classical model is very accurate. Here we begin by considering a classical model in the point dipole limit and consider the total macroscopic response of the medium to be simply N times the atomic dipole response, where N is the number density of atoms.

The combination of the Coulomb potential and the angular momentum of the orbiting electron creates a potential landscape with a minimum. As with any minimum, this potential can be approximated by a parabola as long as the displacement of the electron is small. This means that as long as the electric field of our incident light is small compared to the binding field, which is almost always the case, the electron acts as if it is bound to the nucleus by a spring. We can include any possible energy losses as a velocity dependent damping term.

$$m_e\ddot{\vec{r}} + \gamma\dot{\vec{r}} + k_0\vec{r} = 0 \tag{1.13}$$

Combining the local field with the light fields we model the response of a material to the light and therefore have sources for the re-emmitted light. The force due to the light is dominated by the electric field because it is a factor of c, eight orders of magnitude, larger than the magnetic field. Combining the internal forces (1.13) with the force due to the electric field of the light we find the expression

$$m_e\ddot{\vec{r}} + \gamma\dot{\vec{r}} + k_0\vec{r} = -e\vec{E}_0 e^{i(\vec{k}\cdot\vec{r}-\omega t)} \tag{1.14}$$

In the visible and infrared regime the wavelength of the light is much longer than the size of a single atom so the term $\vec{k}\cdot\vec{r}$ can be ignored, resulting in a damped, sinusoidally driven simple harmonic oscillator.

$$m_e\ddot{\vec{r}} + \gamma\dot{\vec{r}} + k_0\vec{r} = -e\vec{E}_0 e^{-i\omega t} \tag{1.15}$$

This is commonly known as the Lorentz Oscillator Model (LOM) and it is the basis for the theory of dispersion in dielectric materials. The sources of radiation are time dependent polarizations

$$\vec{P} = -Ne\vec{r} \tag{1.16}$$

To solve the equation we notice that the driving force is harmonic, therefore we assume the solution will also be harmonic at the same frequency. This changes all of the time derivatives to ω

$$\left(-m_e\omega^2 - i\omega m_e\gamma + k_0\right)\vec{r} = -e\vec{E} \tag{1.17}$$

and we can multiply through by N and solve for $\vec{P}$

$$\vec{P} = \frac{Ne^2/m_e}{\omega_0^2 - \omega^2 - i\omega\gamma}\vec{E} \tag{1.18}$$

where $\omega_0 = \sqrt{k_0/m_e}$ is the natural frequency.

In a medium the wave equation contains source terms.

$$\nabla \times (\nabla \times \vec{E}) + \frac{1}{c^2}\frac{\partial^2 \vec{E}}{\partial t^2} = -\mu_0 \frac{\partial^2 \vec{P}}{\partial t^2} \tag{1.19}$$

Substituting the polarization from Eq. (1.18) into Eq. (1.19) and using the vector identity (1.7) we obtain

$$\nabla^2 \vec{E} = \frac{1}{c^2}\left(1 + \frac{Ne^2}{m_e\varepsilon_0}\frac{1}{\omega_0^2 - \omega^2 - i\omega\gamma}\right)\frac{\partial^2 \vec{E}}{\partial t^2} \tag{1.20}$$

which again has a plane wave solution of the form

$$\vec{E} = \vec{E}_0 e^{i(Kz - \omega t)} \tag{1.21}$$

but with a complex wavenumber K. By substitution of Eq. (1.21) into (1.20), the requirement for a solution of the given form

$$K^2 = \frac{\omega^2}{c^2}\left(1 + \frac{Ne^2}{m_e\varepsilon_0}\frac{1}{\omega_0^2 - \omega^2 - i\omega\gamma}\right) \tag{1.22}$$

We can write this complex wavenumber in real and imaginary parts

$$K = k + i\alpha \tag{1.23}$$

which allows us to write our plane wave solution as

$$\vec{E} = \vec{E}_0 e^{-\alpha z} e^{i(kz - \omega t)} \tag{1.24}$$

This form shows that the amplitude of the wave decreases exponentially with distance and is known as Beer's Law.

Rather than using a complex wavenumber, K, we can also use a complex refractive index $N = \frac{c}{\omega}K$. Equating the real and imaginary parts yields a set of equations from which the functions $n(\omega)$ and $\kappa(\omega)$ can be found.

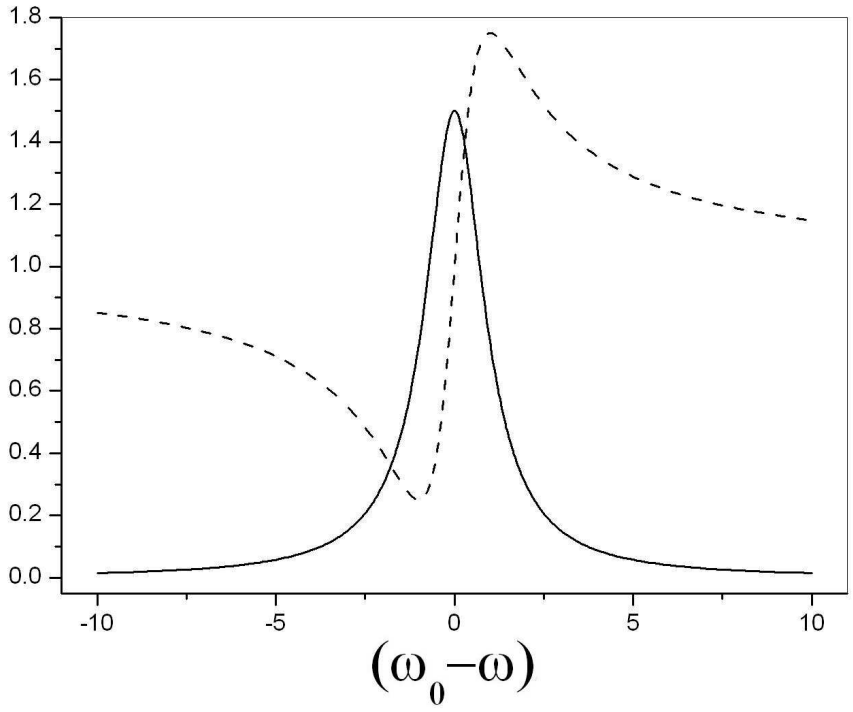

Figure 1.1 Frequency dependence of $n(\omega)$ (solid curve) and $\kappa(\omega)$ (dashed curve). The damping parameter γ corresponds to the full width at half maximum of $n(\omega)$.

The solution for the dispersion relation given by Eq. (1.22) displays the familiar properties of dispersion and resonant absorption. If the incoming light is oscillating at a frequency near the natural frequency ω_0, a significant fraction of the light is absorbed and the index of refraction is significantly different than one as shown in Fig. 1.1 [6]. In this model the dispersion is entirely due to electric polarization because magnetic response has been ignored. In the next section the model is extended to include magnetic response and magnetic contributions to the dispersion.

1.3 Magneto-Optics

Magnetic fields can be included in this type of analysis. Ignoring damping for simplicity, we again assume the electron is bound to the nucleus as if by a spring. The external forces now include both electric and magnetic fields.

$$m_e\ddot{\vec{r}} + \gamma\dot{\vec{r}} + k\vec{r} = -e\vec{E} - e\vec{r}\times\vec{B} \tag{1.25}$$

In this situation the electric field is still due to the light field and therefore we still have a solution of such a form that both the electric field term and $\vec{r}$ vary sinusoidally in time. The magnetic field is a DC field applied externally. This allows us to again convert all time derivatives to $i\omega$

$$\left(-m_e\omega^2+k\right)\vec{r} = -e\vec{E} + i\omega e\vec{r}\times\vec{B} \tag{1.26}$$

We still want to find the polarization, so collecting terms of $\vec{P} = -Ne\vec{r}$

$$\left(-m_e\omega^2+k\right)\vec{P} = Ne^2\vec{E} + i\omega e\vec{P}\times\vec{B} \tag{1.27}$$

This equation allows us to extend our basic model of optics into magneto-optics, optics in the presence of a large magnetic field. Applying a magnetic field in a certain direction can change how light propagates through the material. If we choose the magnetic field to be parallel to the direction of propagation of the light, i.e. the $\hat{z}$ direction, we can solve (1.27) in component form.

$$\left(-m_e\omega^2+k\right)P_x = Ne^2E_x + i\omega eP_yB_z \tag{1.28}$$

$$\left(-m_e\omega^2+k\right)P_y = Ne^2E_y + i\omega eP_xB_z \tag{1.29}$$

$$\left(-m_e\omega^2+k\right)P_z = Ne^2E_z \tag{1.30}$$

This system of equations can be put in a more illuminating form showing the polarization generated for a given electric field input

$$\vec{P} = \varepsilon_0\vec{\chi}\vec{E} \tag{1.31}$$

This system of equations then takes the form

$$\vec{P} = \varepsilon_0\begin{pmatrix}\chi_{11} & i\chi_{12} & 0\\ -i\chi_{12} & \chi_{11} & 0\\ 0 & 0 & \chi_{33}\end{pmatrix}\vec{E} \tag{1.32}$$

where

$$\chi_{11} = \frac{Ne^2}{m_e \varepsilon_0} \left(\frac{\omega^2 - \omega^2}{(\omega_0^2 - \omega^2)^2 - \omega^2 \omega_c^2} \right) \tag{1.33}$$

$$\chi_{33} = \frac{Ne^2}{m_e \varepsilon_0} \left(\frac{1}{(\omega_0^2 - \omega^2)} \right) \tag{1.34}$$

$$\chi_{12} = \frac{Ne^2}{m_e \varepsilon_0} \left(\frac{\omega \omega_c}{(\omega_0^2 - \omega^2)^2 - \omega^2 \omega_c^2} \right) \tag{1.35}$$

$$\omega_c \equiv \frac{eB}{m_e} \tag{1.36}$$

Looking at the susceptibility tensor in (1.32) we see that applying a magnetic field makes the material anisotropic. This illustrates that fact that applying a magnetic field parallel to the direction of propagation of the light, the material becomes optically active and it develops magnetic dispersion. As the light propagates through the medium its polarization rotates. This is known as the Faraday effect and it is used in many ways, perhaps most notably in Faraday isolators. These devices are often used to prevent reflections from damaging delicate optical components by rotating the polarization of reflections to an orientation perpendicular to the original beam and rejecting them with polarization sensitive filters.

A more general analysis of dispersion needs to be set in the context of nonlinear optics. As the intensity of the incident light increases, the amplitude of motion of the electrons increases beyond that which is allowed by the simple harmonic approximation. As a consequence, new contributions to dispersion appear.

In what follows we limit ourselves to dielectric media in which there are no free charges or currents, allowing us to set $\vec{J}_f = 0$ and $\rho_f = 0$. In the absence of light the medium is assumed to be non-magnetic. Hence $\vec{B} = \mu_0 \vec{H}$ and $\vec{D} = \varepsilon_0 \vec{E} + \vec{P}$ but $\vec{P}$ may contain terms proportional to more than one field. This does not exclude the possibility of the development of magnetic response on individual atoms in a dilute medium. In this case Maxwell's equations are

$$\nabla \cdot \vec{D} = 0 \tag{1.37}$$

$$\nabla \cdot \vec{H} = 0 \tag{1.38}$$

$$\nabla \times \vec{E} = -\frac{\partial \vec{H}}{\partial t} \tag{1.39}$$

$$\nabla \times \vec{H} = \frac{\partial \vec{D}}{\partial t} \tag{1.40}$$

Following the same procedure as in Section 1.1, we take the curl of one curl equation,

the time derivative of the other and apply the curl identity (1.7). This results in the wave equation for propagation in matter.

$$\nabla^2\vec{E} - \frac{1}{\varepsilon_0 c^2}\frac{\partial^2\vec{D}}{\partial t^2} = 0 \tag{1.41}$$

In order to include the nonlinear effects of driving the electrons beyond the simple harmonic approximation we allow for the polarization to have a nonlinear component

$$\vec{D} = \varepsilon_0\left(1+\chi^{(1)}\right)\vec{E} + \vec{P}^{NL} \tag{1.42}$$

giving us a wave equation for the electric field due to nonlinear polarization [7].

$$\nabla^2\vec{E} - \frac{\left(1+\vec{\chi}^{(1)}\right)}{c^2}\frac{\partial^2\vec{E}}{\partial t^2} = \frac{1}{\varepsilon_0 c^2}\frac{\partial^2\vec{P}^{NL}}{\partial t^2} \tag{1.43}$$

Polarization can be expanded as a power series in the electric field.

$$\vec{P} = \varepsilon_0\left(\chi^{(1)}\vec{E} + \chi^{(2)}\vec{E}^2 + \chi^{(3)}\vec{E}^3 + \ldots\right) \tag{1.44}$$

The susceptibility $\chi^{(n)}$ is a tensor. This allows the electric field direction to the generate polarizations in directions other than parallel to the electric field. The susceptibility tensor effectively contains the symmetry of the nonlinear medium and thus dictates which directions of motion and therefore polarizations are allowed. Group theory allows us to determine the possible susceptibility tensors due to the symmetry of the medium. Even without group theory we can make one important deduction regarding which terms of (1.44) contribute in an important type of material, a centrosymmetric medium.

A centrosymmetric medium is one in which a reversal of all position vectors causes no change. This means that $\chi(x) = \chi(-x)$. We apply such a symmetry by inverting all parameters in the interaction

$$\begin{gathered}\vec{E}(-\vec{x}) = -\vec{E}(\vec{x}) \\ \vec{P} = \varepsilon_0\left(\chi^{(1)}\vec{E} + \chi^{(2)}\vec{E}^2 + \ldots\right) \rightarrow -\vec{P} = \varepsilon_0\left(\chi^{(1)}(-\vec{E}) + \chi^{(2)}(-\vec{E})(-\vec{E}) + \ldots\right)\end{gathered} \tag{1.45}$$

We see that for the linear term, and therefore for all odd order terms, both sides of the equation changed signs. However, the quadtratic term, and therefore all even order terms, must be identically zero because $\vec{P} = -\vec{P}$. This means that any materials with centrosym-

metry cannot support second order nonlinear effects. The first nonlinear optical effect to be discovered was frequency doubling or second harmonc generation (SHG). Historically, even after the prediction of nonlinear effects in optics the first experiments to measure them were performed in silica, a centrosymmetric medium. It was the insight of Weinreich that the material must lack inversion symmetry that allowed SHG to be measured for the first time in crystaline quartz [8].

An extension of this argument that is not typically considered is very important to the results of this thesis. Polarizations are only one of the possible responses of a medium under the influence of electromagnetic fields. It is also possible, in principle, to induce magnetizations and magnetizations have different symmetry properties. While polarizations are vectors, they are functions of the position vector, magnetizations are pseudovectors, the result of the cross product of two vectors. An inversion of coordinates does not change the sign of a pseudovector [9]. Thus, since magnetizations are even under inversion, it is possible to have a second order nonlinear effect that generates a magnetization in a centrosymmetric medium.

$$\vec{M} = \varepsilon\left(\chi^{(1)}\vec{E} + \chi^{(2)}\vec{E}\vec{H} + \ldots\right) \rightarrow \vec{M} = \varepsilon\left(\chi^{(1)}(-\vec{E}) + \chi^{(2)}(-\vec{E})(-\vec{H}) + \ldots\right) \quad (1.46)$$

We see in this situation that for the linear term, and therefore for all odd order terms, the magnetization does not change sign. However, the even order terms are non-zero. This implies that materials with centrosymmetry *can* support second order nonlinear effects, but only to generate nonlinear magnetizations, not polarizations. This being said, the preceding sections have followed tradition by pointing out the small magnitude of B relative to E and omitting magnetization from Maxwell's equations altogether.

A further generalization of nonlinear optics into the relativistic regime is presented in Appendix A

1.4 Magnetization at Optical Frequencies

When the magnetic field is ignored, linearly polarized light causes the electrons of a material to oscillate, at the light frequency, along the direction of the electric field. Since the nucleus is many orders of magnitude more massive it is assumed to remain stationary. This creates a time-varying electric dipole that oscillates at the light frequency.

$$\vec{p}(t) = p_0 \cos \omega t \hat{z} \tag{1.47}$$

If we assume that the dipole oscillation is small compared to the wavelength of the light and that we are observing the light from a distance much larger than both the size of the dipole and the wavelength of the light, the radiated fields and power from the electric dipole source are given by

$$\vec{E} = -\frac{\mu_0 p_0 \omega^2}{4\pi} \left(\frac{\sin\theta}{r} \right) \cos\left[\omega(t - r/c)\right] \hat{\theta} \tag{1.48}$$

$$\vec{B} = -\frac{\mu_0 p_0 \omega^2}{4\pi c} \left(\frac{\sin\theta}{r} \right) \cos\left[\omega(t - r/c)\right] \hat{\phi} \tag{1.49}$$

$$\vec{S} = \frac{\mu_0}{c} \left[\frac{p_0 \omega^2}{4\pi} \left(\frac{\sin\theta}{r} \right) \cos\left[\omega(t - r/c)\right] \right]^2 \hat{r} \tag{1.50}$$

where $\hat{r}$ is the radial unit vector, $\hat{\theta}$ is the polar angle unit vector measured from the $\hat{z}$ axis and $\hat{\phi}$ is the axial angle unit vector measured from the $\hat{x}$ axis. These relations are valid when the wavelength of UV, visible, and IR light is both several orders of magnitude larger than atoms and several orders of magnitude smaller than typical measuring distances. We see that power is radiated away from the dipole radially but in a $\sin\theta^2$ pattern. The polarization, the orientation of the electric field, is in the $\hat{\theta}$ direction which will appear parallel to the dipole from the point of view of a distant observer.

A similar oscillation can be imagined in which a charge is induced to move in a circle about the $\hat{z}$ axis. Viewed from along the $\hat{x}$ axis the charge is seen to oscillate. This motion is that of a magnetic dipole.

$$\vec{m}(t) = m_0 \cos \omega t \hat{z} \tag{1.51}$$

Under the same assumptions as those above, the radiated fields and intensity can be re-calculated for a magnetic dipole source.

$$\vec{E} = -\frac{\mu_0 m_0 \omega^2}{4\pi c}\left(\frac{\sin\theta}{r}\right)\cos\left[\omega(t-r/c)\right]\hat{\phi} \tag{1.52}$$

$$\vec{B} = -\frac{\mu_0 m_0 \omega^2}{4\pi c^2}\left(\frac{\sin\theta}{r}\right)\cos\left[\omega(t-r/c)\right]\hat{\theta} \tag{1.53}$$

$$\vec{S} = \frac{\mu_0}{c}\left[\frac{m_0\omega^2}{4\pi c}\left(\frac{\sin\theta}{r}\right)\cos\left[\omega(t-r/c)\right]\right]^2\hat{r} \tag{1.54}$$

Again, we see that power is radiated radially in a dipole pattern. However, this time the polarization is in the $\hat{\phi}$ direction which will appear perpendicular to the dipole when viewed by a distant observer. This is the key distinguishing feature between magnetic and electric dipoles [10]. Next, the question of whether the magnitude m_0 of an induced magnetic dipole like the one in Eq. (1.51) can be large at optical frequencies is considered.

A famous argument by Landau and Lifshitz attempts to prove that no material has a significant magnetic susceptibility at optical frequencies [5]. Magnetic susceptibility implies generating a magnetic moment, defined as

$$\vec{m} = \frac{1}{2}\int \vec{x}\times\vec{J}(\vec{x})d^3x \tag{1.55}$$

The physical quantity required is $\vec{J}$, the current due to the moving charge. Current appears in the the curl of B Maxwell equation

$$\nabla\times\vec{B} = \mu_0\vec{J} + \mu_0\varepsilon_0\frac{\partial\vec{E}}{\partial t} \tag{1.56}$$

which can also be written in terms of free current

$$\nabla\times\vec{H} = \vec{J}_f + \frac{\partial\vec{D}}{\partial t} \tag{1.57}$$

In order to expose the magnetization $\vec{M} = \vec{B}/\mu_0 - \vec{H}$, the magnetic response of the medium, we subtract (1.57) from (1.56). Doing so leaves us with an expression for the bound current

$$\vec{J}_b = \nabla\times\vec{M} + \frac{\partial\vec{P}}{\partial t} \tag{1.58}$$

however, the integral (1.55) can only be put in the form $\int\vec{M}dV$ if $\vec{J} = \nabla\times\vec{M}$ and $\vec{M} = 0$ outside the volume of integration. In other words, $\vec{M}$ is only well defined if the term $\frac{\partial\vec{P}}{\partial t}$ can

be neglected. Landau and Lifshitz present the following dimensional agrument against such a situation:

> For a given frequency, the most favourable conditions for measuring the susceptibility are those where the body is as small as possible (to increase the space derivatives in $\nabla \times \vec{M}$) and the electric field is as weak as possible (to reduce $\vec{P}$). The field of an electromagnetic wave does not satisfy the latter condition, because E$\tilde{\text{H}}$. Let us therefore consider a variable field, say in a solenoid, with the body under investigation placed on the axis. The electric field is due only to induction by the variable magnetic field, and the order of magnitude of E inside the body can be obtained by estimating the terms in the equation $\nabla \times \vec{E} = -(1/c)\frac{\partial \vec{B}}{\partial t}$, whence $E/l \sim \omega H/c$ or $E \sim (\omega l/c)H$, where l is the dimension of the body. Putting $\varepsilon - 1 \sim 1$, we have $\frac{\partial P}{\partial t} \sim \omega E \sim \omega^2 l H/c$. For the space derivatives of the magnetic moment $\vec{M} = \chi \vec{H}$ we have $|c\nabla \times \vec{M}| \sim c\chi H/l$. If $|\frac{\partial \vec{P}}{\partial t}|$ is small compared with $|c\nabla \times \vec{M}|$, we have
>
> $$l^2 \ll \chi c^2/\omega^2 \tag{1.59}$$
>
> It is evident that the concept of magnetic susceptibility can be meaningful only if this inequality allows dimensions of the body which are (at least) just macroscopic, i.e. if it is compatible with the inequality $l \gg a$, where a is the atomic dimension. This condition is certainly not fulfilled for the optical frequency range; for such frequencies, the magnetic susceptibility is always $\sim v^2/c^2$, where v is the electron velocity in the atom; but the optical frequencies themselves are $\sim v/a$, and therefore the right-hand side of the inequality (1.59) is $\sim a^2$.
>
> Thus there is no meaning in using the magnetic susceptibility from optical frequencies onward, and in discussing such phenomena we must put $\mu = 1$. To distinguish between $\vec{B}$ and $\vec{E}$ in this frequency range would be an overrefinement. Actually, the same is true for many phenomena even at frequencies well below the optical range.

This argument [5] and other less rigorous versions have discouraged all research into magnetic effects at optical frequencies except in the relativistic optics regime where $v^2/c^2 \sim 1$. In this thesis, not only are large magnetic effects discovered experimentally at optical frequencies under non-relativistic conditions, but the flaw in the argument of Landau and Lifshitz is exposed.

In Chapter II, theoretical work is presented in two main parts, classical and quantum. In the classical section 2.1, the sources of radiation are examined, particularly the multipole expansion of radiation from oscillating sources of interest to us in optics. This leads to the realization that all radiation is caused by the position of charges as a function of time. The

Complete Lorentz Oscillator Model (CLOM) is developed and solved by several methods to provide different insights. The position versus time of the electron cloud and therefore the sources of radiation are found.

In the quantum section 2.2, a density matrix model of the optical magnetic interaction is developed. The expectation values of position of the electric and magnetic dipole operators are found to have the same form as the solutions from the classical model. The quantum model is then extended to include the symmetry of the system in order to predict which materials, namely symmetry groups, will show a large suceptibility to the optical magnetic interaction. This result will guide future research toward finding materials of interest in the study of Transverse Optical Magnetism and the development of optical processes and devices exploiting Transverse Optical Magnetism.

In Chapter III, the experimental setup and techniques for measuring large magnetic dipole scattering are discussed. Particular focus is placed on the choice of samples and measurement techniques to exclude the possibility of other nonlinear processes obscuring our signal. Chapter IV presents the experimental results. Chapter V discusses the experimental results and examines the possibility of exploitation for expanding nonlinear optics and developing new technology. Comments are made about future research both in the short and long term as well as the possible impact of this research on other fields of research and development.

Chapter 2

Theory

In this chapter a new class of non-linear optical effects associated with Transverse Optical Magnetism is considered. The purpose of this section is to examine the possible mechanisms for the generation of strong magnetic response at optical frequencies. This response includes magnetic dipole scattering, generating large magnetizations in non-magnetic materials, collinear optical rectification, and more.

2.1 Classical Theory

2.1.1 Magnetic Response at Optical Frequencies

First, we revisit the argument against magnetic response at optical frequencies by Landau and Lifshitz. Based on experimental observation of optical magnetization to be presented in Chapter 4, it is clear that the argument must have a flaw.

Magnetic dipole radiation is generated by time-dependent magnetic dipoles. As stated by Landau and Lifshitz, the definition of a magnetic dipole is given by:

$$\vec{m} = \frac{1}{2}\int \vec{x}\times\vec{J}(\vec{x})d^3x \tag{2.1}$$

$$= \frac{1}{2}\int \vec{x}\times\left(\nabla\times\vec{M}+\frac{\partial\vec{P}}{\partial t}\right)d^3x \tag{2.2}$$

where, in the case of dielectrics, the current can only be bound current defined in Eq. (1.58). Written in tensor form for ease of manipulation

$$\frac{1}{2}\varepsilon_{ijk}\int_V r_j J_k d^3\vec{r} = \frac{1}{2}\varepsilon_{ijk}\int_V r_j \frac{\partial P_k}{\partial t} d^3\vec{r} + \frac{1}{2}\varepsilon_{ijk}\varepsilon_{klm}\int_V r_j \frac{\partial M_m}{\partial r_l} d^3\vec{r}$$
$$= \frac{1}{2}\frac{\partial}{\partial t}\varepsilon_{ijk}\int_V r_j P_k d^3\vec{r} + \frac{1}{2}(\delta_{il}\delta_{jm} - \delta_{im}\delta_{jl})\left[\int_S r_j M_m d^2 r_{n\neq l} - \delta_{jl}\int_V M_m d^3\vec{r}\right] \tag{2.3}$$

where the indices can take three values indicating the cartesian vector direction, δ_{ij} is a Kronecker delta function that equals 1 if $i = j$ and 0 if $i \neq j$, and ε_{ijk} is the Levi-Civita tensor that equals 0 if any two indicies are equal, 1 if the indices are an even permutation of ijk, and -1 if the indices are an odd permutation of ijk. The integral over the surface is zero because we assume that the magnetization is zero outside the medium. This yields, in vector form,

$$\frac{1}{2}\int_V \vec{r}\times\vec{J}_b d^3\vec{r} = \frac{1}{2}\frac{\partial}{\partial t}\int_V \vec{r}\times\vec{P} d^3\vec{r} + \int_V \vec{M} d^3\vec{r} \tag{2.4}$$

It is common to drop the first term on the right hand side since we are most often considering steady state solutions. In that situation, the time dependence would be zero. However, in the case of illumination by light, the polarization *is* time dependent! Thus, as the polarization changes in time to follow the electromagnetic fields of the light, it can contribute to the generation of magnetic dipoles directly! The only restriction is due to the cross product. The time derivative of polarization must have a non-zero value away from the origin that is due to axial, not radial, motion. We will see later in this chapter that this is precisely what occurs in the presence of the Lorentz force.

2.1.2 Sources of Radiation in the Multipole Expansion

With the possibility of magnetic response at optical frequencies confirmed, we need to find the sources of such magnetization. We begin by looking at light scattering in dielectrics. When light passes through a material, the electric and magnetic fields of the light exert forces on the charges of which the matter is made. In the far field of the light source we can approximate the incident fields to take the form of a plane wave, meaning that the fields and therefore the charges in the material, oscillate sinusoidally in time. Since each frequency component of the light wave can be handled separately, we lose no generality by considering a single frequency component [11].

$$\rho(\vec{x},t) = \rho(\vec{x})e^{-i\omega t} \tag{2.5}$$

$$\vec{J}(\vec{x},t) = \vec{J}(\vec{x})e^{-i\omega t} \tag{2.6}$$

As is well known the choice of gauge is arbitrary [11] in developing a multipole expansion for the vector potential. Following convention we use the Lorenz gauge in which the vector potential generated by moving charges can be written as

$$\vec{A}(\vec{x},t) = \frac{\mu_0}{4\pi}\int d^3x' \int \frac{\vec{J}(\vec{x}',t')}{|\vec{x}-\vec{x}'|}\delta\left(t' + \frac{|\vec{x}-\vec{x}'|}{c} - t\right)dt' \tag{2.7}$$

where primes indicate integration coordinates.

The sinusoidal time dependence simplifies this equation to

$$\vec{A}(\vec{x}) = \frac{\mu_0}{4\pi}\int \vec{J}(\vec{x}')\frac{e^{ik|\vec{x}-\vec{x}'|}}{|\vec{x}-\vec{x}'|}d^3x' \tag{2.8}$$

In the far field, where we will operating, the exponential in (2.8) can be approximated by

$$|\vec{x}-\vec{x}'| \simeq r - \vec{n}\cdot\vec{x}' \tag{2.9}$$

If we want only the leading term in kr, the inverse distance $\frac{1}{|\vec{x}-\vec{x}'|}$ can be replaced with r and the vector potential becomes

$$\lim_{kr\to\infty}\vec{A}(\vec{x}) = \frac{\mu_0}{4\pi}\frac{e^{ikr}}{r}\int \vec{J}(\vec{x}')e^{-ik\vec{n}\cdot\vec{x}'}d^3x' \tag{2.10}$$

If the source dimensions are small compared to the wavelength as they are in optics, we can expand the integral in powers of k

$$\lim_{kr\to\infty}\vec{A}(\vec{x}) = \frac{\mu_0}{4\pi}\sum_n \frac{(-ik)^n}{n!}\int \vec{J}(\vec{x}')(\vec{n}\cdot\vec{x}')^n d^3x' \tag{2.11}$$

This result is the common multipole expansion for radiation.

We are interested in the largest effects so we take only the first term

$$\vec{A}(\vec{x}) = \frac{\mu_0}{4\pi}\frac{e^{ikr}}{r}\int \vec{J}(\vec{x}')d^3x' \tag{2.12}$$

of the multipole expansion. We examine the typical derivation of the result that only the electric dipole, $\vec{p}$, contributes to the vector potential at first order.

The integral of the current cannot in and of itself be solved because no information is given about the current. However, it should be possible to recast this integral into a different form using integration by parts. We note that the goal of this integration by parts is to find a tensor product expressed as a pure derivative that evaluates to two terms, one of the form we already have

$$\int \vec{J}(\vec{x}')d^3x' \tag{2.13}$$

and another of a form which can be evaluated either directly or indirectly.

Similar to an equation found in chapter 9 of [11],

$$\int \vec{J}(\vec{x}')d^3x' = -\int \vec{x}'(\nabla' \cdot \vec{J})d^3x' \tag{2.14}$$

It is common to choose a tensor product for integration by parts of the form

$$\nabla \cdot (\vec{x}\vec{J}) = \vec{J} + \vec{x}(\nabla \cdot \vec{J}) \tag{2.15}$$

where we note that the second term on the right hand side contains the term $\vec{x}(\nabla \cdot \vec{J})$ used in its primed form in (2.14). We perform an integration by parts on this product. Integrating both sides of (2.15) we apply the divergence theorem to the left hand side

$$\int (\nabla \cdot (\vec{x}\vec{J}))d^3x = \int \vec{J}d^3x + \int \vec{x}(\nabla \cdot \vec{J})d^3x \tag{2.16}$$

$$\oint_{S(\infty)} (\hat{n} \cdot (\vec{x}\vec{J}))d^2x = \int \vec{J}d^3x + \int \vec{x}(\nabla \cdot \vec{J})d^3x \tag{2.17}$$

Assuming the current is localized, i.e. there is no current on the surface at infinity, the surface term on the left hand side goes to zero

$$0 = \int \vec{J}d^3x + \int \vec{x}(\nabla \cdot \vec{J})d^3x \tag{2.18}$$

$$\int \vec{J}d^3x = -\int \vec{x}(\nabla \cdot \vec{J})d^3x \tag{2.19}$$

The left hand side is an integral of the current, as we needed, and the right hand side involves

the divergence of the current. We can learn about the form of the divergence of the current from Maxwell's equations. Beginning with Ampere's Law because it contains current

$$\nabla \times \vec{B} = \mu_0 \left(\vec{J}_f + \frac{\partial \vec{D}}{\partial t} \right) \tag{2.20}$$

we take the divergence of both sides to have a divergence of current term. On the left hand side, the divergence of a curl is zero so we can quickly simplify.

$$\nabla \cdot \nabla \times \vec{B} = \mu_0 \left(\nabla \cdot \vec{J}_f + \frac{\partial \nabla \cdot \vec{D}}{\partial t} \right) = 0 \tag{2.21}$$

$$\nabla \cdot \vec{J}_f = - \left(\frac{\partial \nabla \cdot \vec{D}}{\partial t} \right) \tag{2.22}$$

The divergence of $\vec{D}$ is also a Maxwell equation $\nabla \cdot \vec{D} = \rho_f$, so we substitute

$$-\frac{\partial \rho_f}{\partial t} = \nabla \cdot \vec{J}_f \tag{2.23}$$

This says that if the current is diverging through surface there must be a time rate of change of the current density within that surface. This is the Law of Conservation of Charge. Following standard procedure again, we assume the charges and currents vary sinusoidally in time, so the time derivative can be evaluated

$$i\omega\rho = \nabla \cdot \vec{J} \tag{2.24}$$

and we plug this result into our integral (2.15)

$$\int \vec{J}(\vec{x}')d^3x' = -\int \vec{x}'(\nabla' \cdot \vec{J})d^3x' = -i\omega \int \vec{x}'\rho(\vec{x}')d^3x' \tag{2.25}$$

The final integral in (2.25) is the electric dipole moment

$$\vec{p} = \int \vec{x}'\rho(\vec{x}')d^3x' \tag{2.26}$$

allowing the first term of the multipole expansion of the vector potential (2.12) to be

re-expressed in the form

$$\vec{A}(\vec{x}) = -\frac{i\mu_0\omega}{4\pi}\vec{p}\frac{e^{ikr}}{r} \tag{2.27}$$

It appears from this result that only the electric dipole contributes to the vector potential at first order.

This result, while technically correct has three flaws. First, the choice of $\nabla\cdot(\vec{x}\vec{J})$ as the tensor product to begin with is arbitrary. There are other products that contain $\vec{J}$ as a term in their expanded form. This leads immediately to the second flaw. While it is commonplace to call the identity

$$\int \nabla\cdot\vec{A}d^3x = \oint \hat{n}\cdot\vec{A}d^2x \tag{2.28}$$

the Divergence Theorem, it is in fact only one of a family of identities in which the volume integral of any gradient operator applied to a tensor can be transformed into a surface integral of the normal vector performing the same operation on the tensor. For example

$$\int \nabla\times\vec{A}d^3x = \oint \hat{n}\times\vec{A}d^2x \tag{2.29}$$

is another Divergence Theorem. This allows us to explore many other tensor products that might be chosen to make an integration by parts. The third flaw results from not treating the current as a full vector field. We know from Helmholtz theory that any vector field can be described by its divergence and its curl. However, by using the continuity equation, we have implicity assumed that the current is curl free. The continuity equation describes the divergence of a current, which is a vector field, but makes no comment about its curl. This makes sense physically since a purely solenoidal, i.e. only curl, vector field will not have any net flow through a bounding surface. The continuity equation cannot describe the curl of the current. If the current does have a solenoidal component, we have failed to account for it in this derivation.

Beginning with equation (2.12) we will now proceed with these flaws in mind. We will choose a new tensor product which may contain more terms. We will use a different version of the Divergence Theorem if required, and we will not assume the curl of the current, implicitly or explicitly, is identically zero. First we must choose a vector product whose expanded form contains $\vec{J}$ as a term; but what products are available? We begin by considering a vector J, three-dimensional postion vector x, and derivative ∇. We construct a general combination of these in standard index notation, $A_{abc} = \partial_a(x_b J_c)$. In order to use the Divergence Theorem and eliminate A_{abc} through $\oint A_{abc}d^2x = 0$, the derivative must be

outside the product $x_b J_c$. Furthermore, the expanded terms must be rank one so contraction must occur over two of the indices. Only one free parameter, a, b, or c, is left uncontracted yielding a vector.

Our first possible product is $\partial_j(x_i J_j)$ which amounts to contracting the derivative with the J term of a tensor Jx

$$\begin{aligned}
\partial_j(x_i J_j) &= x_i \partial_j J_j + J_j \partial_j x_i \\
&= x_i \partial_j J_j + J_j \delta_{ij} \\
&= x_i \partial_j J_j + J_i \\
&= x \nabla \cdot J + J \\
0 &= \int x \nabla \cdot J + \int J \\
\int J &= -\int x \nabla \cdot J
\end{aligned} \tag{2.30}$$

This result is (2.25). It represents a divergence of J and can be replaced by the electric dipole term.

The second possible product is $\partial_j(x_j J_i)$ where we use the transpose of the tensor from the previous choice.

$$\begin{aligned}
\partial_j(x_j J_i) &= x_j \partial_j J_i + J_i \partial_j x_j \\
&= x_j \partial_j J_i + J_i \delta_{jj} \\
&= (x \cdot \nabla) J + 3J \\
0 &= \int (x \cdot \nabla) J + 3 \int J \\
\int J &= -\frac{1}{3} \int (x \cdot \nabla) J
\end{aligned} \tag{2.31}$$

This result is more difficult to interpret geometrically. It is not clear what type of current distribution this describes.

A third product is possible in which $\vec{J}$ is represented by a contraction over the product itself, $\partial_i(x_j J_j)$.

$$\begin{aligned}
\partial_i(x_j J_j) &= x_j \partial_i J_j + J_j \partial_i x_j \\
&= x_j \partial_i J_j + J_j \delta_{ij} \\
&= x_j \partial_i J_j + J_i
\end{aligned} \tag{2.32}$$

In order to write the first term on the right hand side in vector form we must eliminate the

contraction across the derivative. Our strategy is to introduce Kronecker deltas to move the uncontracted index i off of the derivative. The only free parameter is which of the two j indices is left unchanged. This corresponds to which of two commonly available vector identities are used to expand the term $\nabla(x\cdot J)$.

If we leave the x_j alone the term $x_j\partial_i J_j$ can be rewritten as $\delta_{il}\delta_{jm}x_j\partial_l J_m$. We then move the uncontracted index by adding and subtracting the term $x_j\partial_j J_i = \delta_{im}\delta_{jl}x_j\partial_l J_m$

$$\begin{aligned}
\partial_i(x_jJ_j) &= \delta_{il}\delta_{jm}x_j\partial_l J_m - \delta_{im}\delta_{jl}x_j\partial_l J_m + x_j\partial_j J_i + J_i \\
&= (\delta_{il}\delta_{jm} - \delta_{im}\delta_{jl})x_j\partial_l J_m + x_j\partial_j J_i J_i \\
&= \varepsilon_{ijk}x_j\varepsilon_{klm}\partial_l J_m + x_j\partial_j J_i + J_i \\
&= x\times(\nabla\times J) + (x\cdot\nabla)J + J \\
0 &= \int x\times(\nabla\times J) - 2J \\
\int J &= \frac{1}{2}\int x\times(\nabla\times J)
\end{aligned} \tag{2.33}$$

This form depends directly on the curl of the current and is the natural description of a ring antenna. Equation (2.33) is the main result of this section.

If we leave the J_j alone the term $x_j\partial_i J_j$ can be rewritten as $\delta_{im}\delta_{jl}x_l\partial_m J_j$. We then move the uncontracted index by adding and subtracting the term $x_i\partial_j J_j = \delta_{il}\delta_{jm}x_l\partial_m J_j$

$$\begin{aligned}
\partial_i(x_jJ_j) &= \delta_{im}\delta_{jl}x_l\partial_m J_j - \delta_{il}\delta_{jm}x_l\partial_m J_j + x_i\partial_j J_j + J_i \\
&= -(\delta_{il}\delta_{jm} - \delta_{im}\delta_{jl})x_l\partial_m J_j + x_i\partial_j J_j + J_i \\
&= -\varepsilon_{ijk}\varepsilon_{klm}x_l\partial_m J_j + x_i\partial_j J_j + J_i \\
&= (x\times\nabla)\times J + x(\nabla\cdot J) + J \\
0 &= \int (x\times\nabla)\times J + \int x(\nabla\cdot J) + \int J
\end{aligned} \tag{2.34}$$

Using (2.15) we can see that $\int(x\times\nabla)\times J = 0$.

In summary,

$$\int J = \int -x(\nabla\cdot J) \tag{2.35}$$

$$= \int -\frac{1}{3}(x\cdot\nabla)J \tag{2.36}$$

$$= \int \frac{1}{2}x\times(\nabla\times J) \tag{2.37}$$

$$\int (x\times\nabla)\times J = 0 \tag{2.38}$$

The three approaches, Eqs. (2.35), (2.36), and (2.37), furnish alternative ways of representing the integral of current density. (2.36) is similar to (2.35) but with a different grouping of operations that changes the magnitude of the result by a factor of three. The third result, (2.37) is the most important since it provides a way to write the integral of J as a curl rather than a divergence. This means that solenoidal currents can contribute to the first order multipole expansion as much as divergent currents. If we can find a mechanism for generating solenoidal in optics, it should be possible to generate new magneto-optic effects that are large because they occur in the first term of the multipole expansion.

2.1.3 Maximum Solenoidal Current

In this section the question of the maximum possible magnetic current is considered. If a solenoidal current can be developed, how large can it be? These results summarize the earlier arguments made in Ref. [2].

In a dielectric there are no free charges or currents. The Maxwell equation including current is Ampere's Law, which without free current, is written

$$\nabla \times \vec{B} = \mu_0 \left(\varepsilon_0 \frac{\partial \vec{E}}{\partial t} + \vec{J}_M + \vec{J}_P \right) \tag{2.39}$$

If we imagine a plane wave, polarized along the $\hat{x}$ direction, incident on a spherical volume of atoms containing N bound electrons, we know the electrons will be set into motion. Some fraction of the current will be parallel to the polarization direction and some fraction perpendicular.

$$\vec{J}_P = \vec{J}_{P,\perp} + \vec{J}_{P,\parallel} \tag{2.40}$$

$$\vec{J}_M = \vec{J}_{M,\perp} + \vec{J}_{M,\parallel} \tag{2.41}$$

Integrating Ampere's law over the surface S

$$\int_S \left(\nabla \times \vec{B} \right) \cdot d\hat{n}_S = \varepsilon_0 \int_S \frac{\partial \vec{E}}{\partial t} \cdot d\hat{n}_S + \int_S \vec{J}_{p,\parallel} \cdot d\hat{n}_S + \int_S \vec{J}_{M,\parallel} \cdot d\hat{n}_S \tag{2.42}$$

To deduce a relationship between optically induced currents $\vec{J}_P$ and $\vec{J}_M$, one can specialize the calulation to optical frequencies by substituting Faraday's Law $(\nabla \times \vec{E})/i\omega\mu$ for $\vec{H}$ in (2.42). Furthermore we set $\mu = \mu_0(1+\chi_m)$, and consider $\chi_m \ll 1$, which ostensibly limits the estimate of our ratio to transparent media with small polarization and magnetization far

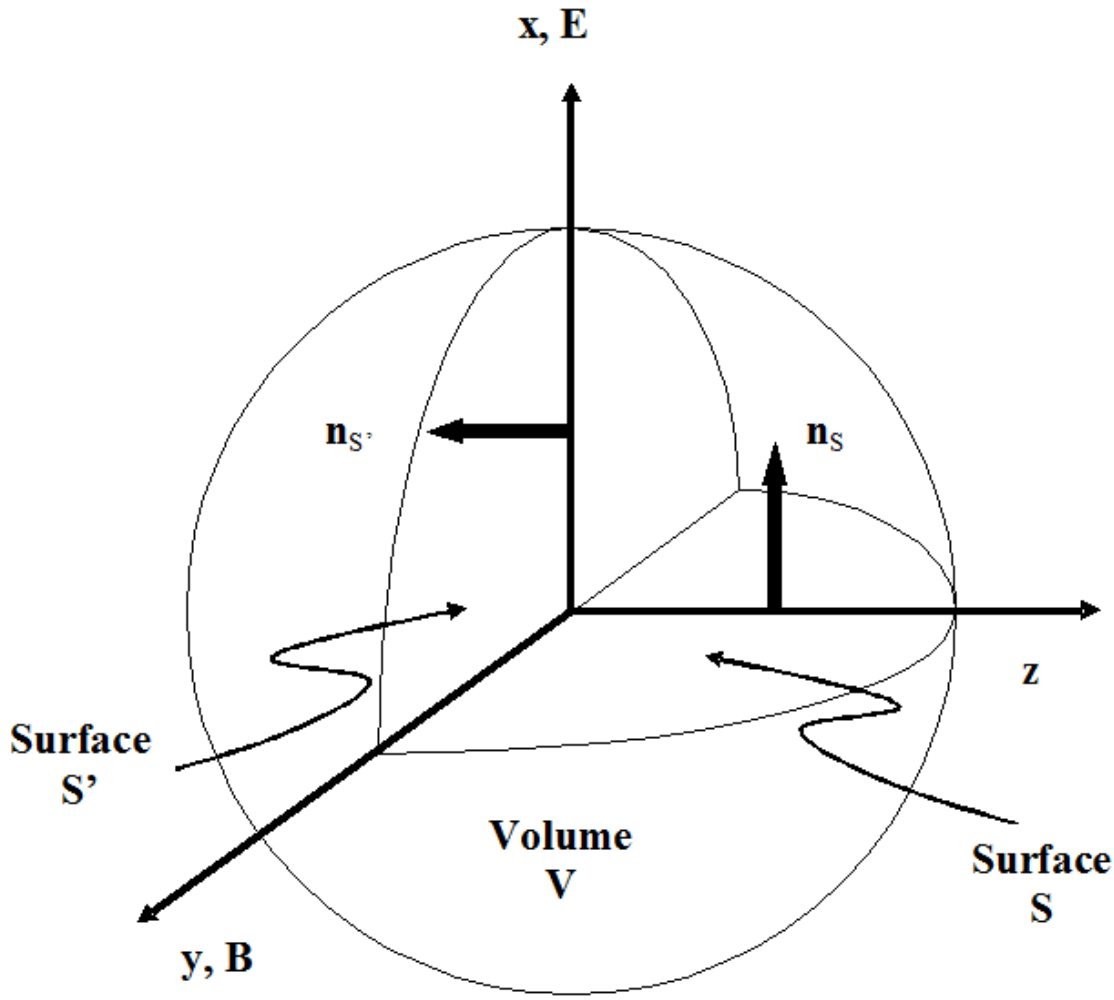

Figure 2.1 Geometry for integration of Ampere's law to determine relative magnitudes and phases of electric and magnetic current density

from resonance. While our experiments were indeed performed in this limit, the theoretical result obtained is more general, as will become evident.

With these approximations, the integral on the left side of (2.42) is equal to the first term on the right. Hence one obtains

$$0 = \int_S \vec{J}_{P,\|} \cdot d\hat{n}_S + \int_S \vec{J}_{M,\|} \cdot d\hat{n}_S \tag{2.43}$$

or

$$\int_S \vec{J}_{M,\|} \cdot d\hat{n}_S = -\int_S \vec{J}_{P,\|} \cdot d\hat{n}_S \tag{2.44}$$

A similar integration over surface S' in Figure 2.1 yields

$$\int_{S'} \vec{J}_{M,\perp} \cdot d\hat{n}_S = -\int_{S'} \vec{J}_{P,\perp} \cdot d\hat{n}_S \tag{2.45}$$

Because $\vec{J}_M$ is by definition a solenoidal current, the amplitudes of $\vec{J}_{M,\parallel}$ and $\vec{J}_{M,\perp}$ are equal $J_{M,\parallel} = J_{M,\perp} = J_M$, the addition of the integrals yields the result

$$J_M = -\frac{1}{2}[J_P]_{tot} = -\frac{1}{2}J_E \tag{2.46}$$

Since the input electric and magnetic fields are in phase, the sign in (2.46) is a phase factor indicating that the magnetic moment opposes the optical magnetic field. The ratio $R_{max} = J_M/J_E = 1/2$ is the same as the ratio of magnetic to electric dipole moments of a perfectly conducting sphere in magnetostatics [11], but here it is obtained in a classical model that treats bound electrons as the carriers of electric and magnetic displacement current densities at optical frequencies. It indicates that of all the charges displaced along $\hat{x}$ by $\vec{E}$, at most half can turn in the $\vec{B}$ field and contribute to positive magnetic current by passing through the surface S'.

Scattered electromagnetic fields in the radiation zone may be calculated using the expressions [12]

$$\vec{E}_{rad} = \frac{1}{4\pi\varepsilon_0 c^2}\int \frac{([\dot{\vec{J}}] \times \hat{r}) \times \hat{r}}{r} dV \tag{2.47}$$

$$\vec{H}_{rad} = \frac{1}{4\pi c}\int \frac{[\dot{\vec{J}}] \times \hat{r}}{r} dV \tag{2.48}$$

where square brackets indicate evaluation at the retarded time and the integration is performed over source volume V. $\hat{r}$ is a unit vector in the direction in the direction of the point of observation at a distance r from the scattering volume. Knowledge of the vector current denisities $\vec{J}_E$ and $\vec{J}_M$ (assumed to be uniform in this continuum model) associated with the time-varying ED and MD moments is enough to determine the electric and magnetic dipole components of light radiated from the sample. This can be seen explicitly by calculating the ratio of the magnitudes of the Poynting vector $\vec{S} = \vec{E}_{rad} \times \vec{H}_{rad}$ for electric and magnetic

radiation, namely S_M/S_E, given by

$$\begin{aligned}\frac{S_M}{S_E} &= \left|\int \frac{\omega(\vec{J}_M \times \hat{r}) \times \hat{r}}{r} dV' \times \int \frac{\omega(\vec{J}_M \times \hat{r})}{r} dV'\right| \Big/ \left|\int \frac{\omega(\vec{J}_E \times \hat{r}) \times \hat{r}}{r} dV' \times \int \frac{\omega(\vec{J}_E \times \hat{r})}{r} dV'\right| \\ &= \frac{J_M^2}{J_E^2}\left|\int \frac{(\vec{J}_M \times \hat{r}) \times \hat{r}}{r} dV' \times \int \frac{(\vec{J}_M \times \hat{r})}{r} dV'\right| \Big/ \left|\int \frac{(\vec{J}_E \times \hat{r}) \times \hat{r}}{r} dV' \times \int \frac{(\vec{J}_E \times \hat{r})}{r} dV'\right| \\ &= \frac{J_M^2}{J_E^2} \end{aligned} \tag{2.49}$$

Since the maximum magnetic current density is $[J_M]_{max} = R_{max} J_E = (1/2) J_E$, it follows that the ratio of the far-field intensities cannot exceed

$$\frac{S_M}{S_E} = R_{max}^2 = \frac{1}{4} \tag{2.50}$$

This is the maximum possible value of the ratio R of magnetic dipole to electric dipole emission intensity in dielectric materials. Even in the non-relativistic limit, the dynamic magnetic dipole moment due to the passage of light may be as large as one half the electric dipole moment. If a mechanism for generating solenoidal currents can be found, it is possible to generate a magnetic current up to one half of the size of the electric current.

2.1.4 Origin of Solenoidal Current

One mechanism for generating current with a curl at optical frequencies is via the Lorentz force. Magnetic fields induce curvature, and therefore curl, in currents. The light in optics already contains a magnetic field that is in phase with the electric field. Our goal is to include the magnetic field of light in the interaction of the light and matter. The Lorentz Oscillator Model (LOM) of optics is based on a picture in which an electron is bound to the nucleus by a harmonic potential and undergoes forced motion subject to internal damping. The external forces are due to components of electromagnetic fields in the form of a plane wave. Since the forces exerted on a charge by electric and magnetic fields are well known, the equations of motion follow directly from Newton's Law.

$$\begin{pmatrix} m & 0 & 0 \\ 0 & m & 0 \\ 0 & 0 & m \end{pmatrix} \begin{pmatrix} \ddot{x} \\ \ddot{y} \\ \ddot{z} \end{pmatrix} + \begin{pmatrix} \gamma_x & 0 & 0 \\ 0 & \gamma_y & 0 \\ 0 & 0 & \gamma_z \end{pmatrix} \begin{pmatrix} \dot{x} \\ \dot{y} \\ \dot{z} \end{pmatrix} + \begin{pmatrix} \omega_x^2 & 0 & 0 \\ 0 & \omega_y^2 & 0 \\ 0 & 0 & \omega_z^2 \end{pmatrix} \begin{pmatrix} x \\ y \\ z \end{pmatrix} = \begin{pmatrix} qE_x + q\dot{y}B_z - q\dot{z}B_y \\ qE_y + q\dot{z}B_x - q\dot{x}B_z \\ qE_z + q\dot{x}B_y - q\dot{y}B_x \end{pmatrix} \tag{2.51}$$

The z axis is defined to be the direction of propagation of the plane wave and the x axis to be parallel to the electric field. This requires that the magnitc field be parallel to the y axis. The fields are also sinusoidal in time. In component form, the equations of motion can be written

$$\ddot{x} + \gamma_x \dot{x} + \omega_x^2 x = \frac{qE_0}{m}\cos(\omega t) - \frac{qB_0}{m}\cos(\omega t)\dot{z} \tag{2.52}$$

$$\ddot{z} + \gamma_z \dot{z} + \omega_z^2 z = \frac{qB_0}{m}\cos(\omega t)\dot{x} \tag{2.53}$$

where γ_i is the damping coefficient in the i^{th} direction, $\omega_i \equiv \sqrt{\frac{k_i}{m}}$ is the natural oscillation frequency in the i^{th} direction, m is the mass of the electron and q is the charge of the electron. E_0 and B_0 are the amplitudes of the electric and magnetic components of the field. In a departure from earlier work [13], these equations are left in component form to avoid dropping any terms that couple motion between the x and z directions. A perturbation solution to them may then be sought and thoroughly checked by numerical integration as described in the next section. Through agreement between perturbation and numerical approaches, it will be shown that dynamic coupling between the electric and magnetic degrees of freedom in an oscillator model with Lorentz forces yields dramatically enhanced magnetic response at modest intensities. In section 2.1.7 the enhancement mechanism is explored by reducing the equations of motion to a Mathieu equation. Solutions are plotted in a stability diagram which illustrates the relaxed conditions under which parametric enhancement is expected. Excellent agreement is thereby reached with the experimental results presented in Chapter 4 and quantum theory of Section 2.2.

2.1.5 A Lorentz Model Including Magnetic Forces

Maxwell's equations show that the ratio of the electric to magnetic field amplitudes for a plane wave in free space is $E_0/B_0 = c$. Thus, the electric field amplitude E_0 is eight orders of magnitude larger than the magnetic field amplitude B_0. It is therefore common practice to drop the final term in (2.52) and in (2.53) involving the magnetic field amplitude. This simplification results in a single driven equation of motion

$$\ddot{x} + \gamma_x \dot{x} + \omega_x^2 x = \frac{qE_0}{m}\cos(\omega t) \tag{2.54}$$

for the x coordinate alone (see for example Ref.[14]). Eq. (2.54) is the starting relation for the standard LOM. In this thesis the LOM is adopted as the zeroth order description of the

system (following [15]) and an expansion is used to examine the consequences of retaining the magnetic terms in the description of the driven motion of bound electrons.

If the magnetic field terms in (2.52) and in (2.53) are small, they can be considered a perturbation of the motion. Introducing the order parameter λ, it is assumed that solutions then take the form

$$x(t) = x_0(t) + \lambda x_1(t) + \lambda^2 x_2(t) + \ldots \tag{2.55}$$

$$z(t) = z_0(t) + \lambda z_1(t) + \lambda^2 z_2(t) + \ldots \tag{2.56}$$

where $x_1, x_2 \ldots$ are amplitudes associated with orders 1,2.... In the present treatment the electric field is considered in zero order and the magnetic field is considered in first order. We substitute (2.55) and (2.56) into the equations of motion, namely (2.52) and (2.53), and collecting terms of like order in λ.

Collecting terms that are zeroth order in λ, one finds

$$\ddot{x_0} + \gamma_x \dot{x_0} + \omega_x^2 x_0 = \frac{qE_0}{m} \cos(\omega t) \tag{2.57}$$

$$\ddot{z_0} + \gamma_z \dot{z_0} + \omega_z^2 z_0 = 0 \tag{2.58}$$

These equations of motion constitute the standard LOM and have been well studied in the past. For an electron initially at rest at the origin, they yield the solutions

$$x_0(t) = \frac{qE_0}{m\sqrt{((\omega_x^2 - \omega^2)^2 + \gamma_x^2 \omega^2)}} \cos(\omega t + \phi_0) \tag{2.59}$$

$$z_0(t) = 0 \tag{2.60}$$

where $\phi_0 = \tan^{-1}\left(\frac{-\gamma_x \omega}{(\omega_x^2 - \omega^2)}\right)$. The solution for motion along the electric field is proportional to the amplitude of the applied field E_0 and oscillates harmonically at the driving frequency ω. The amplitude is enhanced near resonance by a factor that depends on the detuning, $(\omega_x - \omega)$, and the damping, γ_x, of the linear motion along $\hat{x}$.

Collecting terms that are first order in λ yields the equations

$$\ddot{x}_1 + \gamma_x \dot{x}_1 + \omega_x^2 x_1 = -\frac{qB_0}{m} \cos(\omega t) \dot{z}_0 \tag{2.61}$$

$$\ddot{z}_1 + \gamma_z \dot{z}_1 + \omega_z^2 z_1 = \frac{qB_0}{m} \cos(\omega t) \dot{x}_0 \tag{2.62}$$

The driving terms of these equations depend on the derivatives of the zeroth order solutions. Consequently, the derivatives of the zeroth order solutions are needed.

$$\dot{x}_0 = -\frac{\omega q E_0}{m\sqrt{((\omega_x^2-\omega^2)^2+\gamma_x^2\omega^2)}}\sin(\omega t+\phi_0) \tag{2.63}$$

$$\dot{z}_0 = 0 \tag{2.64}$$

To solve the system of equations (2.61)-(2.64), the homogeneous version of the x_1 equation is considered first.

$$\ddot{x}_1 + \gamma_x \dot{x}_1 + \omega_x^2 x_1 = 0 \tag{2.65}$$

The solution to this equation with our initial conditions is simply

$$x_1(t) = 0 \tag{2.66}$$

Equation (2.66) confirms the expected result that there is no additional response in the x direction at first order.

The z_1 equation is solved next. The homogeneous solution is the same as the previous order, so only the particular solution needs to be found. Substituting (2.63) into (2.62), one finds

$$\ddot{z}_1 + \gamma_z \dot{z}_1 + \omega_z^2 z_1 = -\frac{\omega q^2 E_0 B_0}{m^2\sqrt{((\omega_x^2-\omega^2)^2+\gamma_x^2\omega^2)}}\cos(\omega t)\sin(\omega t+\phi_0) \tag{2.67}$$

in which a product of sine and cosine functions at the optical frequencies appears. Using the trigonometric identity $\cos(a)\sin(b) = \frac{1}{2}(\sin(a+b)-\sin(a-b))$ this may be simplified to

$$\ddot{z}_1 + \gamma_z \dot{z}_1 + \omega_z^2 z_1 = -\frac{\omega q^2 E_0 B_0}{2m^2\sqrt{((\omega_x^2-\omega^2)^2+\gamma_x^2\omega^2)}}[\sin(2\omega t+\phi_0)-\sin(\phi_0)] \tag{2.68}$$

Because this equation is linear, a particular solution of the entire equation of motion for $z(t)$ can be found by analyzing each of the two driving terms in square brackets on the right side of (2.68) separately and then adding the results. The solution for $z(t)$, complete to first order,

is

$$
\begin{aligned}
z(t) &= z_1(0,t) + z_1(2\omega,t) \\
&= \frac{-\omega q^2 E_0 B_0}{2m^2\omega_z^2\sqrt{(\omega_x^2-\omega^2)^2+\gamma_x^2\omega^2}}\sin(\phi_0) \\
&+ \frac{1}{\sqrt{\left(\left(\omega_z^2-(2\omega)^2\right)^2+\gamma_z^2(2\omega)^2\right.}}\frac{\omega q^2 E_0 B_0}{2m^2\sqrt{(\omega_x^2-\omega^2)^2+\gamma_x^2\omega^2}}\sin\left(2\omega t+\phi_0-\phi_1\right)
\end{aligned}
\tag{2.69}
$$

where $\phi_1 = \tan^{-1}\left(\frac{-\gamma_z 2\omega}{\left(\omega_z^2-(2\omega)^2\right)}\right)$. Similarly, the solution for $x(t)$, correct to first order, is

$$
\begin{aligned}
x(t) &= x_0(\omega,t) \\
&= \frac{qE_0}{m\sqrt{((\omega_x^2-\omega^2)^2+\gamma_x^2\omega^2)}}\cos\left(\omega t+\phi_0\right)
\end{aligned}
\tag{2.70}
$$

It is possible to derive any term in the expansion by the method outlined in Appendix B.

Eqs. (2.69) and (2.70) are the main results of this section. Superficially it appears that the solutions do not contain a magnetic dipole. However, if the motion is examined in the $x-z$ plane as seen in Fig. 5.2 we notice that the electron follows a curved trajectory. The electron traces this arc at the driving frequency ω. The projection of this motion onto the x axis is then, clearly, at the driving frequency. However, because the motion does not form a closed loop, the projection of the arcing motion at ω onto the z axis is at 2ω. Thus, we see the ω solution in x and the 2ω solution in z are both due to a curved motion at ω. The torsional oscillation about the y-axis at ω is a magnetic dipole that will radiate at ω. This result will play an important role in experimental design in Chapter 3.

2.1.6 Numerical Simulations

The perturbation solutions given by (2.69) and (2.70) can be checked by comparing their predictions to numeric solutions. Using a fourth order Runge-Kutta integration method, equations (2.52) and (2.53) are solved and the motion of the electron is plotted to examine transient and steady state response. In Figs. 2.4-2.6, projections of electron trajectories on the laboratory x and z axes are computed by direct integration of these force equations and amplitudes of motion along these two directions plotted as a function of field intensity and natural oscillation frequency for comparison with (2.69) and (2.70). Fig. 2.2 is a reference

plot showing the position of the electron plotted with all parameters set to unity except B_0, which is set to $1/(3\times10^8)$ to preserve the ratio $E_0/B_0 = c$ of a plane wave. Thus, the electric field amplitude is $E_0 = 1V/m$.

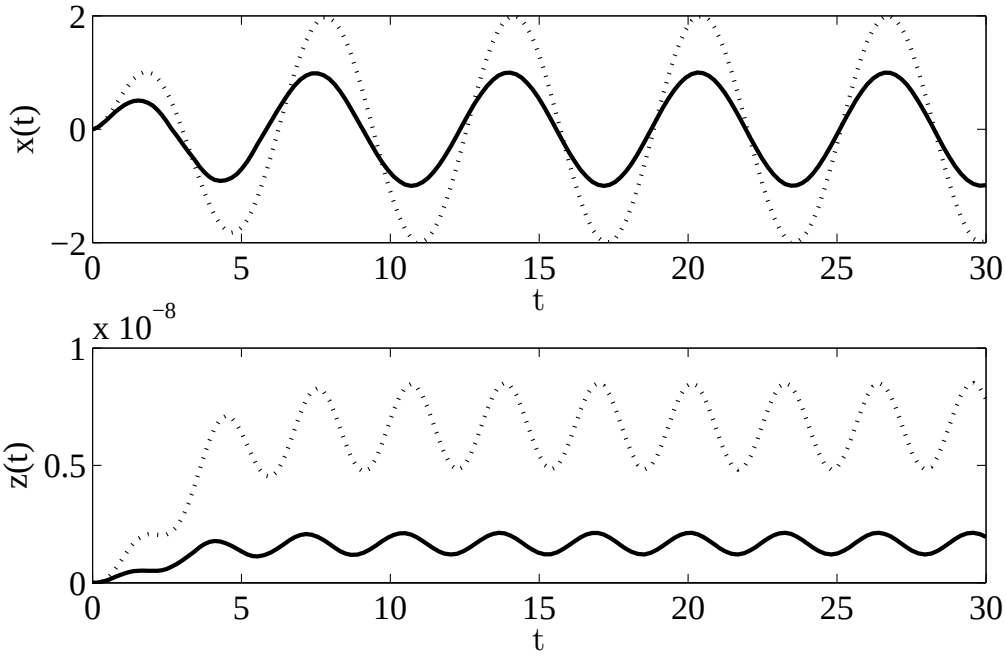

Figure 2.2 Solid lines are reference plots of electron motion for all parameters set to unity while preserving $E_0 = 1V/m$ and $B_0 = 1/c\,T$. Dashed lines are plots of electron motion with the fields doubled to $E_0 = 2V/m$ and $B_0 = 2/c\,T$.

In Fig. 2.2, both the x and z motions reach steady-state oscillation after a short transient period. The period of the x motion in Fig. 2.2 is 2π and the period of the z motion in Fig. 2.2 is π. Hence, the frequency ratio is $1/2$, as predicted in the perturbation result of Eq. (2.69). It can also be seen that the x motion is centered about zero, whereas the z motion is offset by a constant amount in the steady state as predicted by the zero frequency term of the perturbation solution. While the amplitude of motion at low intensity is nine orders of magnitude greater in the x direction than in the z direction, at higher intensity, corresponding to $E_0 = 10^8 V/m$ and $B_0 = 10^8/c\,T$, the amplitude of motion along these two directions becomes comparable as seen in Fig. 2.3.

Numerous additional checks of the perturbation solution and its predictions were made using this method of numerical integration of the equations of motion. For this purpose, a single parameter in Eqs. (2.69) and (2.70) was chosen and all others were fixed at their reference value. The chosen parameter was then varied over a wide range of values and the steady state values of the x amplitude, z amplitude, and the z offset were plotted versus the parameter. As an example, the solid curve in figure 2.2 was calculated with all param-

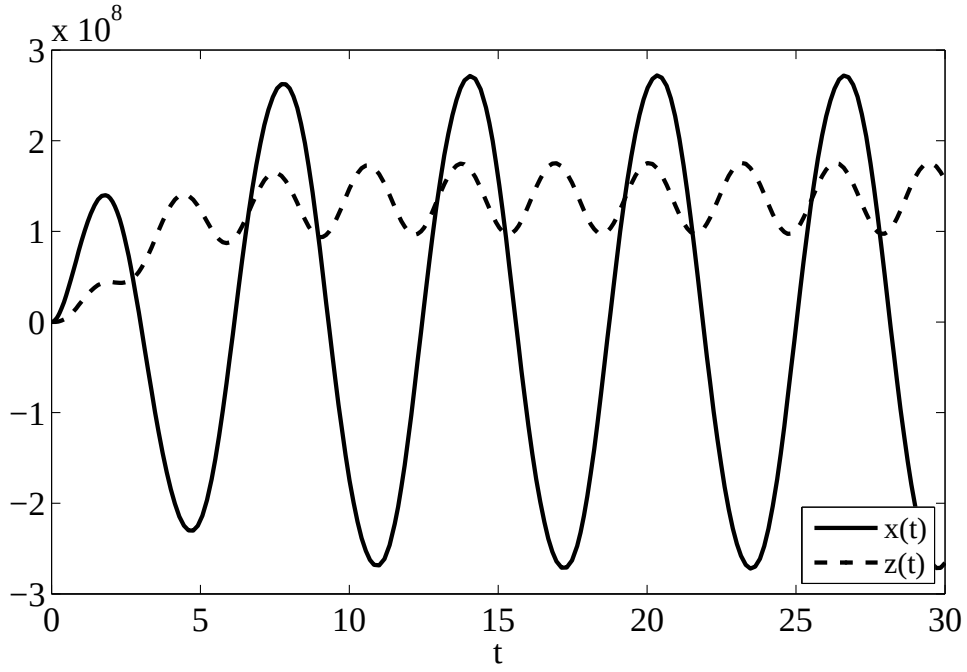

Figure 2.3 Plots of electron motion in both x and z directions on the same scale for all parameters set to unity while $E_0 = 10^8\, V/m$ and $B_0 = 10^8/c\,T$

eters set to the default values of unity whereas the dashed curves were obtained with all parameters *except* E_0 and B_0 set to the default values and E_0 and B_0 set to twice the default value. Clearly the x amplitude in Fig. 2.2 increases linearly with this change, but both the z offset and z amplitude increase quadratically. This procedure was repeated for a wide range of values of E_0 and B_0 to generate figure 2.4. The resulting log-log plot shows that the amplitude of the x motion grows linearly with increasing field. The slope of the fitted curve is one. The amplitude of z motion and the offset of z motion increase quadratically with the field. The slopes of their fitted curves are both two.

Figure 2.5 shows that both z amplitude and z offset have a resonance at $\omega_x = 1$ as predicted by the perturbation solution. The x amplitude also has a resonance at $\omega_x = 1$ but this result was not included in the figure because it is predicted by the standard LOM. Figure 2.6 shows that the z amplitude has a resonance at $\omega_z = 2$ as predicted by the perturbation solution. It also shows that the z offset obeys a $1/\omega_z^2$ dependence, indicated by the slope of -2. Thus, all of the major features of response amplitude predicted by the perturbation calculation are confirmed by numeric integration of the equations of motion.

The first order solution for $x_1(t)$ is unchanged with respect to the linear response expression for $x_0(t)$. Hence, it still shows a linear dependence on the input field, together with damped resonance about the natural frequency ω_x and a damping dependent phase shift

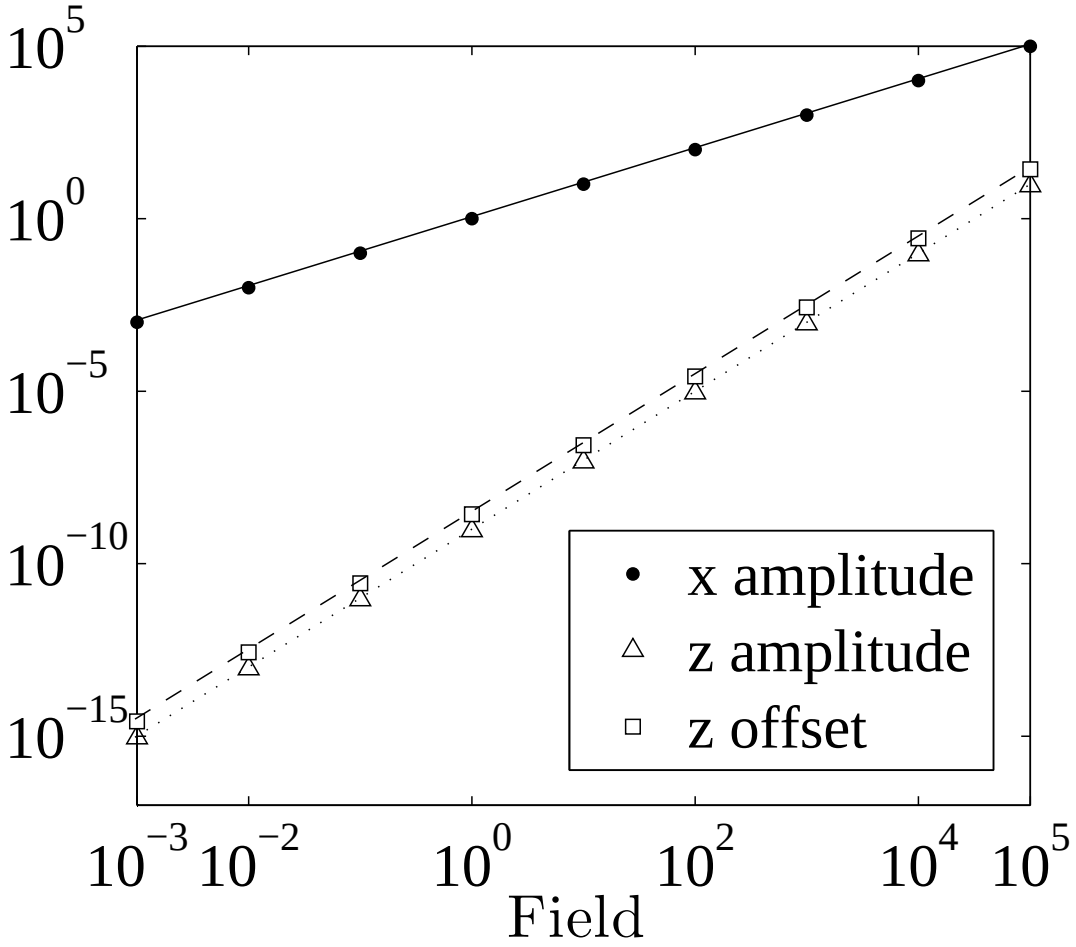

Figure 2.4 Behavior of x and z amplitudes and z offset versus the input field. All parameters fixed at unity *except* E_0 and B_0 which are varied to generate the plot. Note that the x amplitude shows a linear dependence on field whereas the z amplitude and offset both exhibit quadratic dependences.

ϕ_0. The motion in the z direction, given by $z_1(t)$, is much more complicated. First, there are two different frequency components in the response, one at zero frequency and another that oscillates at twice the driving frequency. However, both components show a quadratic dependence on the input fields as is expected for a magneto-optic non-linearity. Both terms also show a resonance at the natural frequency ω_x, but the second, frequency-doubled 2ω term shows an additional resonance at $\omega = \omega_z/2$.

It was shown that charge motion induced by an incident plane wave is no longer linear when magnetic forces are included. In particular, motion along the direction of propagation is much larger at high intensities than expected due to magnetic coupling between the motion in the x and z directions. Even though the coupling strength is dependent on the magnetic field amplitude, which is small, it is evident that large amplitude, complex dynamics which are magnetic in origin arise at moderate field strengths of the order of

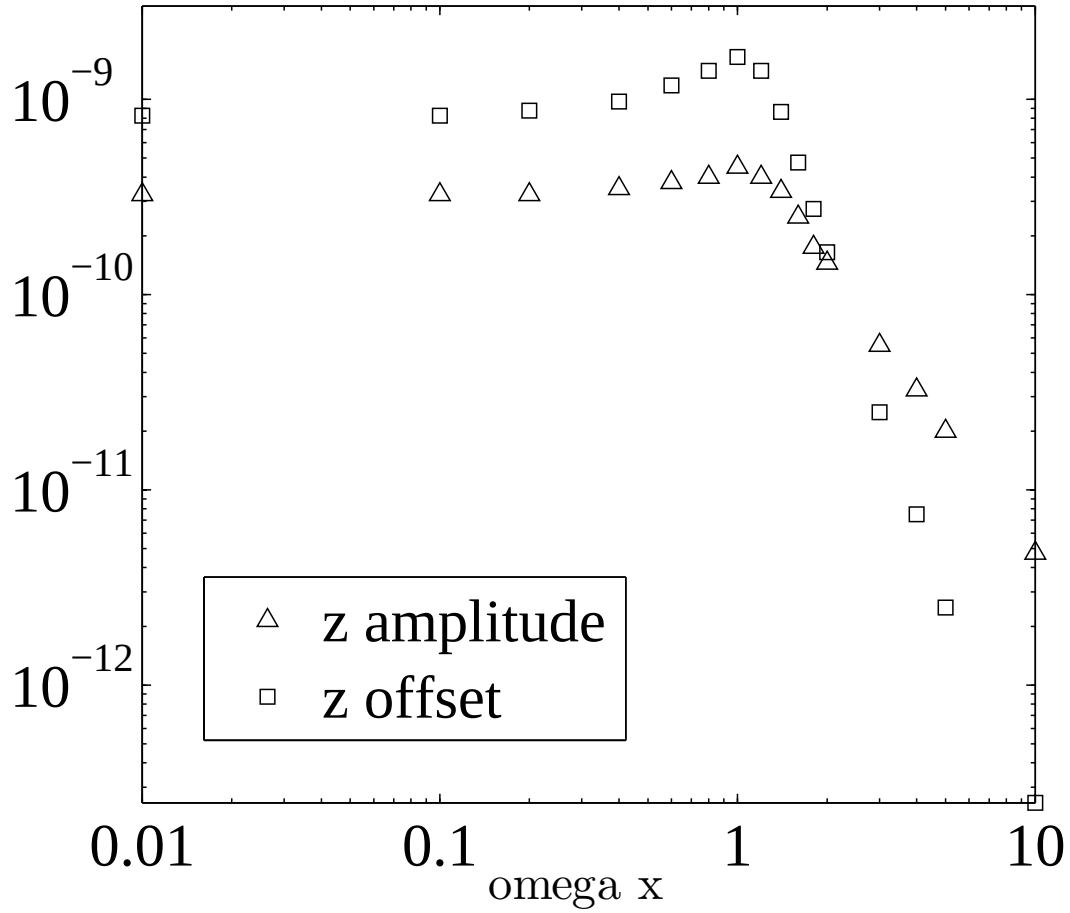

Figure 2.5 Behavior of z amplitude and z offset versus ω_x. All parameters fixed at unity *except* ω_x which is varied to generate the plot. Note that both have a resonance at $\omega_x = 1$.

$E = 10^8 V/m$. This result calls for analysis to clarify the origin of large amplitude magnetic dynamics at non-relativistic intensities.

2.1.7 A Mathieu Model of Optical Interactions

Solving the equations of motion of the Complete Lorentz Oscillator Model by perturbation to high order, one will eventually find a solution that depends directly on time, such as $t\sin(t)$. These terms indicate growth of the solution without bound. Such a result is a classic behavior of unstable systems in which the solutions grow exponentially in time. A classic equation in the study of instability is the Mathieu equation. Since we know that terms directly dependent on time will appear at high order, we will now attempt to write the equations of motion in a Mathieu-like form.

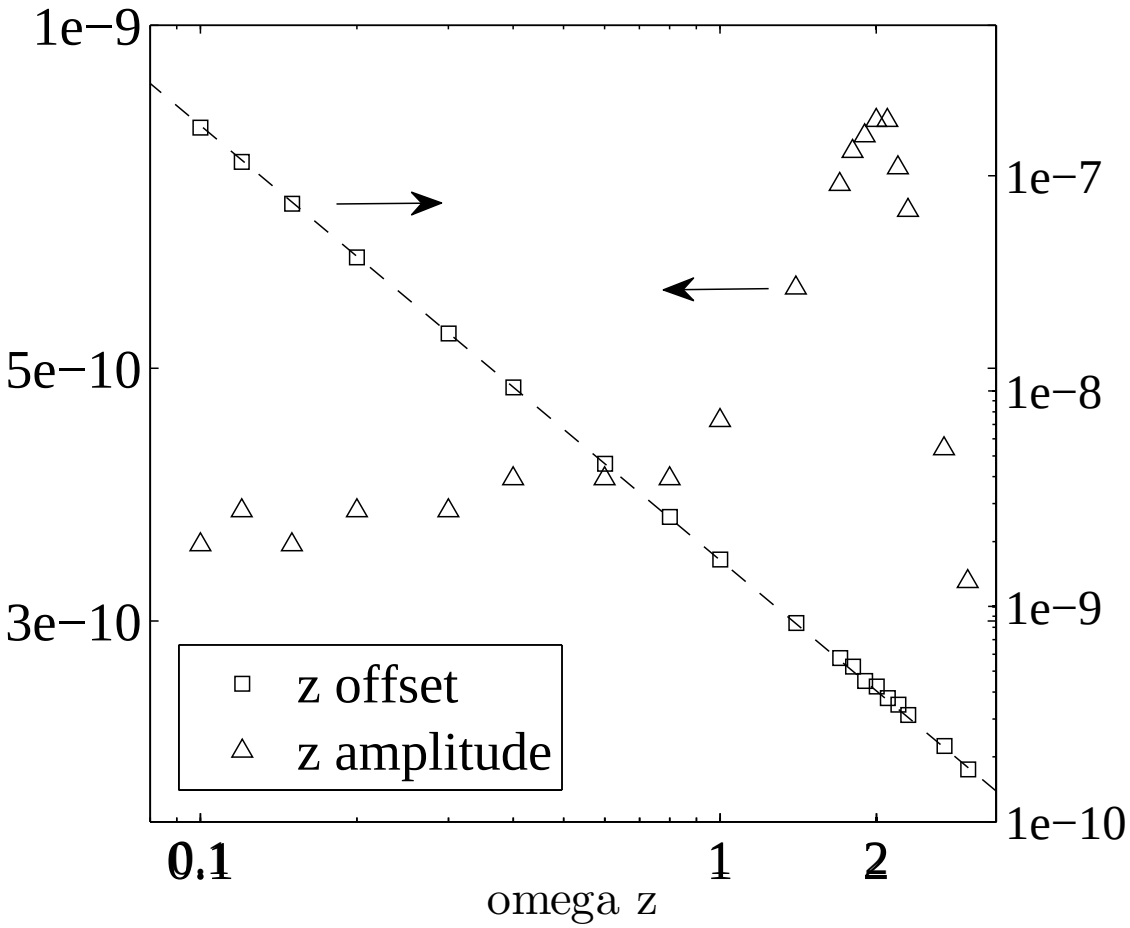

Figure 2.6 Behavior of z amplitude and z offset versus ω_z. All parameters fixed at unity *except* ω_z which is varied to generate the plot. Note that the z amplitude has a resonance at $\omega_z = 2$ and that the z offset follows an inverse quadratic behavior (slope=-2).

By rearranging equations (2.52) and (2.53) into a form so that all terms that depend on the coordinates are on the left hand side and the external driving terms are on the right hand side, the underlying structure can be more clearly seen.

$$\ddot{x} + \gamma_x \dot{x} + \frac{qB_0}{m}\cos(\omega t)\dot{z} + \omega_x^2 x = \frac{qE_0}{m}\cos(\omega t) \tag{2.71}$$

$$\ddot{z} + \gamma_z \dot{z} - \frac{qB_0}{m}\cos(\omega t)\dot{x} + \omega_z^2 z = 0 \tag{2.72}$$

The non-autonomous terms whose coefficients depend on the independent variable t are of main interest here. All terms in Eqs. (2.71) and (2.72) have constant coefficients except for the coupling terms. The Lorentz force terms add to the equations an effective sinusoidal, time-varying damping coefficient. Equations with sinusoidally-varying coefficients are of

particular interest in the study of instability and it is this aspect of the equations that is of particular interest here [16].

To set the discussion of instabilities in appropriate context, we briefly review dynamics described by a traditional Mathieu Equation. The Mathieu Equation is a simple model for a classic problem in instability, namely the vertically driven pendulum. In the prototypical problem, a rigid, massless rod is fixed to a pivot at one end and a mass at the other. The fixed point is then moved vertically, sinusoidally at some amplitude. The linearized equation of motion of the pendulum can then be reduced to

$$\frac{d^2u}{dt^2} + (a - b\cos(2t))\,u = 0 \tag{2.73}$$

The sinusoidally time-dependent spring constant, known as the "parametric excitation", acts as an energy source causing the amplitude of motion, u, to grow to a value dependent on the values a and b. For certain values of a and b, the amplitude of the pendulum grows exponentially to infinity. These regions are said to undergo unstable motion because they are in parametric resonance. More discussion of this topic can be found in many differential equation texts, including [16], [17]. For an intuitive introduction, see Ref [18].

In the case of the vertically-driven pendulum, the system spends more time in unstable motion as the amplitude of the parametric excitation grows. The addition of damping does not remove the regions of instability, though it does make them smaller. Only nonlinearities in the system formally prevent the amplitude from growing to infinity exponentially. For sufficiently large amplitude motion it should be admitted however that Eq. (2.73) ceases to be the equation of motion since the approximation of a harmonic restoring force eventually breaks down. Ionization is one way that breakdown of this kind can occur in our system of interest.

For the LOM augmented by magnetic forces, it was shown that z motion is enhanced dynamically by eight orders of magnitude at moderate intensities in the previous section. We now turn to an examination of predictions for parametrically-resonant stable and unstable motions in this model. For ease of mathematical analysis, we use dimensionless forms of the complete equations of motion (2.52) and (2.53)

$$\frac{d^2\chi}{d\tau^2} + \frac{\gamma_x}{\omega}\frac{d\chi}{d\tau} + \frac{\omega_x^2}{\omega^2}\chi = \cos(\tau) - \frac{qB_0}{m\omega}\cos(\tau)\frac{d\zeta}{d\tau} \tag{2.74}$$

$$\frac{d^2\zeta}{d\tau^2} + \frac{\gamma_z}{\omega}\frac{d\zeta}{d\tau} + \frac{\omega_z^2}{\omega^2}\zeta = \frac{qB_0}{m\omega}\cos(\tau)\frac{d\chi}{d\tau} \tag{2.75}$$

which contain the following constants

$$a = \frac{\gamma_x}{\omega}; b = \frac{\omega_x^2}{\omega^2}; c = \frac{\gamma_z}{\omega}; d = \frac{\omega_z^2}{\omega^2}; e = \frac{qB_0}{m\omega} \tag{2.76}$$

The constants a and c represent dimensionless damping parameters, b and d represent dimensionless natural frequencies, and e represents the dimensionless cyclotron frequency due to the magnetic field of the incident plane wave. First, consider a spherically symmetric molecule in which the x and z directions are equivalent, resulting in $a = c$ and $b = d$. For ease of interpretation, these constants maybe be redefined with symbols that are in standard use, namely

$$\gamma = a = c \tag{2.77}$$

$$\omega^2 = b = d \tag{2.78}$$

$$f_c = e \tag{2.79}$$

where we now refer to γ as the dimensionless damping constant, ω as the dimensionless natural frequency, and f_c as the dimensionless cyclotron frequency. The equations of motion then take on the dimensionless form

$$\frac{d^2\chi}{d\tau^2} + \gamma\frac{d\chi}{d\tau} + \omega^2\chi = \cos(\tau) - f_c\cos(\tau)\frac{d\zeta}{d\tau} \tag{2.80}$$

$$\frac{d^2\zeta}{d\tau^2} + \gamma\frac{d\zeta}{d\tau} + \omega^2\zeta = f_c\cos(\tau)\frac{d\chi}{d\tau} \tag{2.81}$$

This process has effectively absorbed the electric field into the coordinates. The problem can now be seen as in the frame of the electric field. The nondimensionalization of the classical equations of motion is very similar to using the dressed state formalism in quantum mechanics. Dressed states are a re-diagonalization of the problem with the effects of the light field included in the Hamiltonian. This creates new basis states that take the light field into account, effectively absorbing the electric field into the basis states. That method will be used in Section 2.2 as one method to calculate the Transverse Optical Magnetic response quantum mechanically.

It will now be shown that these equations of motion can exhibit unstable motion. This conclusion may be reached by considering the equations of motion with only the terms that depend on the coordinates [16]. Dropping the $\cos(\tau)$ factor which is an external forcing

term (i.e. it does not depend on the coordinates of the system) Eq. (2.80) reduces to

$$\frac{d^2\chi}{d\tau^2} + \gamma\frac{d\chi}{d\tau} + \omega^2\chi = -f_c\cos(\tau)\frac{d\zeta}{d\tau} \tag{2.82}$$

and Eq. (2.81) does not change. To proceed, we first make use of the Energy-Rate method [19] to plot a stability diagram of the dimensionless system of equations as shown in Figure 2.7. Wide regions of parameter space are shown to couple energy between the x and z directions of motion.

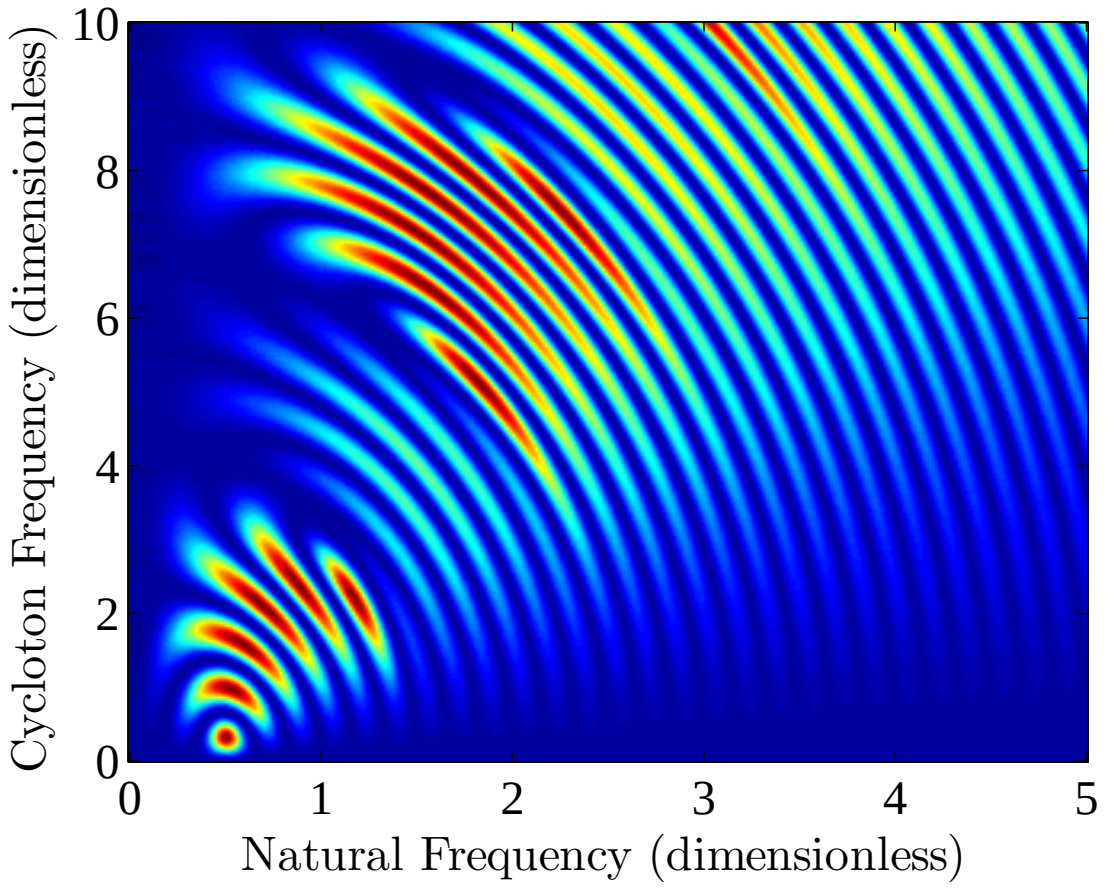

Figure 2.7 Stability diagram of parameter space for the Complex Mathieu Equation evaluated over a 6π integration period using the Energy-Rate Method. Red areas indicate rapid transfer of energy from x (electric) to z (magnetic) degrees of freedom. Blue areas indicate no energy transfer.

Second, the two equations (2.81) and (2.82) can be combined into a single complex equation of motion of the variable $y = (\chi + i\zeta)$. Multiplying Eq. (2.81) by i, adding it to Eq.

(2.82) , and collecting terms results in a single, sinusoidally damped oscillator equation.

$$\frac{d^2y}{d\tau^2} + (\gamma - if_c\cos(\tau))\frac{dy}{d\tau} + \omega^2 y = 0 \tag{2.83}$$

The stability of the Mathieu equation itself is well studied, so a key result of the present work is that this latter equation can be rewritten in the form of a Mathieu equation. By comparing (2.83) and (2.73) it is clear that the damping terms must be eliminated for them to be formally identical. Mathematically, this may be done by modifying (2.83) with an integral transformation [20]. The transformed variable is defined to be $y(t) = w(t)e^{\frac{1}{2}\int_0^t \gamma - if_c\cos(\tau)d\tau}$. Substituting this into the complex equation of motion and collecting terms, one finds

$$\ddot{w}(t) + \frac{1}{8}\left(-2\gamma^2 + 8\omega^2 + f_c^2 + 4if_c\left(\gamma\cos(t) - \sin(t)\right) + f_c^2\cos(2t)\right)w(t) = 0 \tag{2.84}$$

This is a Mathieu type equation of the complex variable $w(t)$. The quantity $\frac{1}{8}(-2\gamma^2 + 8\omega^2 + f_c^2)$ acts as the Mathieu constant a and the quantity $\frac{1}{8}f_c^2$ acts as the Mathieu constant b. The successful transformation of the Complete Lorentz Oscillator Model to a Mathieu type differential equation confirms that the equations of motion support complex dynamics. In particular, the electric and magnetic degrees of freedom of the system can exchange energy due to the magnetic modulation at doubled frequency $2t$ that is governed by the constant f_c (Fig. 2.7).

It should be noted that the quantity f_c which represents the Lorentz force strength appears in all time dependent coefficeients of the equation indicating that it is the source of unexpected, magnetically-induced behavior. If f_c were zero, as applicable to the customary LOM, the equations of motion could not be written as a Mathieu type differential equation. On the other hand, the imaginary, sinusoidal, time-dependent excitation terms in Eq. (2.84) appear to offer novel degrees of freedom and dynamic behavior worthy of additional study.

A similar analysis that is more illuminating can be performed on the dimensionless system of equations (2.80) and (2.81). Rather than transforming the pair of equations into a single complex equation, we rewrite them as a matrix equation. Dropping the external driving force since it plays no role in system stability we end up with

$$\begin{pmatrix} 1 & 0 \\ 0 & 1 \end{pmatrix}\begin{pmatrix} \ddot{x} \\ \ddot{z} \end{pmatrix} + \begin{pmatrix} \gamma_x & f_c\cos(\tau) \\ -f_c\cos(\tau) & \gamma_z \end{pmatrix}\begin{pmatrix} \dot{x} \\ \dot{z} \end{pmatrix} + \begin{pmatrix} \omega_x^2 & 0 \\ 0 & \omega_z^2 \end{pmatrix}\begin{pmatrix} x \\ z \end{pmatrix} = \begin{pmatrix} 0 \\ 0 \end{pmatrix} \tag{2.85}$$

We define some new variables to similify the following derivation.

$$q(t) = q = \begin{pmatrix} 1 & 0 \\ 0 & 1 \end{pmatrix} \quad r(t) = \begin{pmatrix} \gamma_x & f_c\cos(\tau) \\ -f_c\cos(\tau) & \gamma_z \end{pmatrix} s(t) = s = \begin{pmatrix} \omega_x^2 & 0 \\ 0 & \omega_z^2 \end{pmatrix} \quad x = \begin{pmatrix} x \\ z \end{pmatrix} \tag{2.86}$$

This gives us the matrix equation

$$q\ddot{x} + r(t)\dot{x} + sx = 0 \tag{2.87}$$

We will perform a similar integral transformation to the one found above. Assuming $r(t)$ has an antiderivative $R(t)$ and an initial condition $R(0) = 0$ we can define our transformed coordinates y

$$x = e^{-\frac{1}{2}R(t)}y \tag{2.88}$$

$$\dot{x} = -\frac{1}{2}r(t)e^{-\frac{1}{2}R(t)}y + e^{-\frac{1}{2}R(t)}\dot{y} \tag{2.89}$$

$$\ddot{x} = -\frac{1}{2}\dot{r}(t)e^{-\frac{1}{2}R(t)}y + \frac{1}{4}r^2(t)e^{-\frac{1}{2}R(t)}y - r(t)e^{-\frac{1}{2}R(t)}\dot{y} + e^{-\frac{1}{2}R(t)}\ddot{y} \tag{2.90}$$

There is an exponential $e^{-\frac{1}{2}R(t)}$ in each term so we drop it. Putting all of the terms together

$$\ddot{y} - r(t)\dot{y} - \frac{1}{2}\dot{r}(t)y + \frac{1}{4}r^2(t)y + r(t)\dot{y} - \frac{1}{2}r^2(t)y + sy = 0 \tag{2.91}$$

Simplifying this equation we find that there is no longer a term proportional to $\dot{y}$

$$\ddot{y} + \left(-\frac{1}{2}\dot{r}(t) - \frac{1}{4}r^2(t) + s(t)\right)y = 0 \tag{2.92}$$

$$\dot{r}(t) = \begin{pmatrix} 0 & -f_c \sin(t) \\ f_c \sin(t) & 0 \end{pmatrix} \tag{2.93}$$

$$r^2(t) = \begin{pmatrix} \gamma_x^2 - f_c^2 \cos^2(t) & (\gamma_x + \gamma_z) f_c \cos(t) \\ -(\gamma_x + \gamma_z) f_c \cos(t) & \gamma_z^2 - f_c^2 \cos^2(t) \end{pmatrix} \tag{2.94}$$

This system of equations is identical to a damped simple harmonic oscillator when $f_c = 0$ so we can recover the Lorentz Model in the low intensity limit. We can rewrite this equation so that it has the features of a Mathieu equation, particularly a $\cos(2t)$ term, using trigonometric identities

$$\ddot{y} + \begin{pmatrix} \left(-\frac{\gamma_x^2}{4} + \omega_x^2 + \frac{f_c^2}{8}\right) + \frac{f_c^2}{8}\cos(2t) & \frac{f_c}{2}\sqrt{1 + \frac{1}{4}(\gamma_x + \gamma_z)^2}\sin(t+\phi) \\ -\frac{f_c}{2}\sqrt{1 + \frac{1}{4}(\gamma_x + \gamma_z)^2}\sin(t+\phi) & \left(-\frac{\gamma_z^2}{4} + \omega_z^2 + \frac{f_c^2}{8}\right) + \frac{f_c^2}{8}\cos(2t) \end{pmatrix} y = 0 \tag{2.95}$$

where $\phi = \arcsin\left(\frac{-\frac{1}{2}(\gamma_x+\gamma_z)}{\sqrt{1+\frac{1}{4}(\gamma_x+\gamma_z)^2}}\right)$ is a phase shift due to damping. Collecting like groups of parameters we find that the set of equations has the form

$$\ddot{y} + \begin{pmatrix} \alpha_x + \beta\cos(2t) & \delta\sin(t+\phi) \\ -\delta\sin(t+\phi) & \alpha_z + \beta\cos(2t) \end{pmatrix} y = 0 \tag{2.96}$$

$$\alpha_i = -\frac{\gamma_i^2}{4} + \omega_i^2 + \frac{f_c^2}{8} \tag{2.97}$$

$$\beta = \frac{f_c^2}{8} \tag{2.98}$$

$$\delta = \frac{f_c}{2}\sqrt{1 + \frac{1}{4}(\gamma_x + \gamma_z)^2} \tag{2.99}$$

We can see now that this system of equations is a Mathieu equation in each direction that is coupled by a sinusoidal term $\pm\delta\sin(t+\phi)$. The stability of such systems can be studied by multi-scale analysis [21].

2.2 Density Matrix Analysis

2.2.1 Density Matrix Analysis

The purpose of this section is to formulate a quantum mechanical theory of the intense transverse magnetic dipole moments and static electric dipole moments that form in bound electron systems as the result of irradiation with coherent light of moderate intensity. The development closely follows Ref. [22].

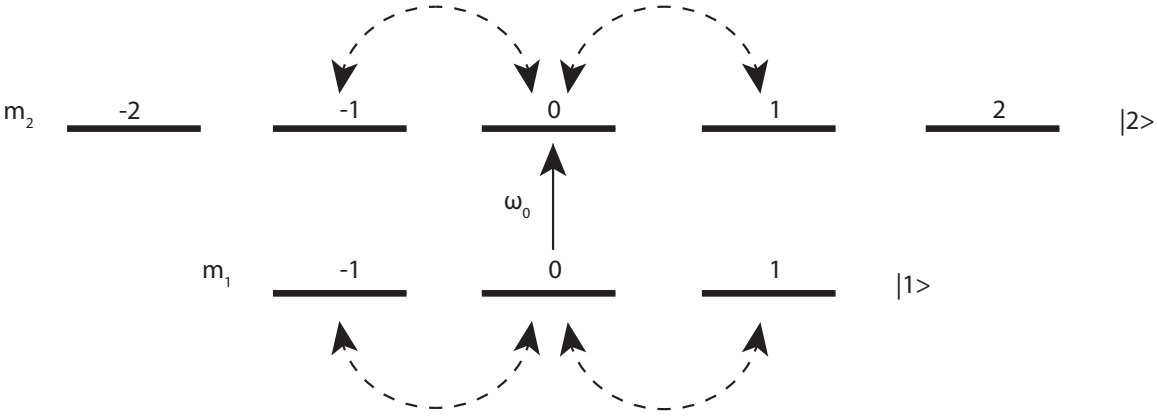

Figure 2.8 Example of an energy level system that permits a combination of electric and magnetic dipole transitions

We begin by considering a system of identical 2-level atoms or molecules with a resonance frequency $\omega_0 = (\omega_2 - \omega_1)$ subjected to an electromagnetic plane wave of frequency ω that propagates in the positive $\hat{z}$ direction (Fig.2.8). The light is linearly polarized along $\hat{x}$ and detuned from resonance by $\delta = \omega_0 - \omega$. Population dynamics and coherences are found using the density matrix equation of motion

$$i\hbar\dot{\rho} = [H,\rho] - i\hbar\dot{\rho}_{relax} \tag{2.100}$$

The system Hamiltonian $H = H_0 + V(t)$ is assumed to consist of a static part,

$$H_0 = \hbar\omega_1|1\rangle\langle 1| + \hbar\omega_2|2\rangle\langle 2|, \tag{2.101}$$

which describes the unperturbed diagonal matrix elements of the static Hamiltonian and an optical interaction V of the combined dipole form

$$V = -\vec{\mu}_e \cdot \vec{E} - \vec{\mu}_m \cdot \vec{B} \tag{2.102}$$

In the semiclassical approach used here, $\dot{\rho}_{relax}$ describes phenomenological relaxation of

individual density matrix elements in the Schrodinger picture. Uppercase rate constants Γ_{ij} are used to describe coherence decay between levels i and j and lowercase constants γ_{ii} give the total population decay rate of a particular level i. The irreducible representations of the (polar) electric and (axial) magnetic components of the optical wave are

$$\vec{E}(t) = -\frac{1}{2}[E_+\hat{\varepsilon}_- + E_-\hat{\varepsilon}_+]e^{i\phi} + h.c. \tag{2.103}$$

$$\vec{B}(t) = -\frac{i}{2}[B_+\hat{\varepsilon}_- - B_-\hat{\varepsilon}_+]e^{i\phi} + h.c. \tag{2.104}$$

In these expressions $\phi = \omega t - kz$ is the optical phase and the circular basis vectors $\varepsilon_\pm = -(\hat{x} \pm i\hat{y})/\sqrt{2}$ are components of the rank one spherical tensor. $h.c.$ is an abbreviation for Hermitian conjugate. Carets are used to denote unit basis vectors. In the case of linear polarization along $\hat{x}$, we note the correspondences

$$E_+ = E_- = E_0/\sqrt{2} \tag{2.105}$$

$$B_+ = B_- = B_0/\sqrt{2} \tag{2.106}$$

which assume the circular components have equal amplitudes. The irreducible electric and magnetic dipole moments induced by the field have magnitudes and directions given by

$$\vec{\mu}^{(e)} = -\left(\mu_-^{(e)}\hat{\varepsilon}_+ + \mu_+^{(e)}\hat{\varepsilon}_-\right) \tag{2.107}$$

$$\vec{\mu}^{(m)} = -i\left(\mu_+^{(m)}\hat{\varepsilon}_- + \mu_-^{(m)}\hat{\varepsilon}_+\right) \tag{2.108}$$

respectively. When the circular componenets $\mu_\pm$ of these moments are equal, the electric and magnetic moments themselves point along $\hat{x}$ and $\hat{y}$ – parallel to the inducing fields. Combining all of these definitions with the Hamiltonian (2.102) gives us the irreducible form of the interaction Hamiltonian. The goal of this work is then to determine the induced electric and magnetic dipole moments, $\mu^{(e)}(t)$ and $\mu^{(m)}(t)$ in the medium. This is done by finding the expectation values which in the density matrix formalism take the form $< \mu^{(e)}(t) >= Tr[\mu^{(e)}, \rho(t)]$ and $< \mu^{(m)}(t) >= Tr[\mu^{(m)}, \rho(t)]$ respectively.

2.2.2 Matrix Elements of Transverse Magnetic Moments

Before proceeding to solve the equation of motion for the density matrix, a discussion of the calculation of expectation values is warranted due to the transverse nature of the magnetic dipole moment to be considered here. Individual light quanta carry spin angular momentum with projections on the axis of propagation given by -$\hbar$,+$\hbar$,or 0, depending on whether their

state is left-circular, right-circular, or linear polarization respectively. In linear single-field MD interactions, the angular momentum needed to create or destroy a magnetic dipole moment is therefore provided by an appropriate state of circularly polarized incident light. However, in what follows, the induced angular momentum is not along $\hat{z}$, which denotes the propagation axis, but along the optical B field (chosen here to point along the transverse $\hat{y}$ direction). The induced transverse moment, therefore, has no projection on the axis of propagation and can be generated without the transfer of any angular momentum from the optical field. For the quadratic interaction of interest here, it will be shown that when the angular momentum of the light field is zero (the case of linearly polarized light), a large magnetic moment that oscillates at the optical frequency itself can be induced perpendicular to $\hat{z}$. The time average value of this orbital angular momentum is zero so that angular momentum is conserved overall. However, this process gives rise to intense, radiant magnetic dipole fields.

To facilitate a comparison of longitudinal and transverse magnetic moments, it is convenient to consider two coordinate systems in which the polar axis is either parallel or perpendicular to the wavevector $\hat{k} = k\hat{z}$. First we discuss longitudinal magnetic moments by considering the coordinate system (r, θ, ϕ) in which the polar and quantization axes are parallel to $\hat{k} = \hat{z}$, and the azimuthal angle ϕ is measured with respect to the x axis. This is the geometry of conventional magnetic dipole transitions. The electric dipole transition moment on a single atom is

$$\begin{aligned} < \vec{\mu}^{(e)}(t) >_{12} &= \hat{r} < \mu^{(e)}(t) >_{12} \\ &= \hat{r} \int \psi_1^*(r,t) er \psi_2(r,t) + h.c. dV \\ &= \hat{r} \int c_1^*(t) \psi_1^*(r) er c_2(t) \psi_2(r) + h.c. dV \\ &= \hat{r} < 1|\mu^{(e)}|2 > \rho_{21}(t) + h.c. \end{aligned} \tag{2.109}$$

The electric field along $\hat{x}$ changes only the radial coordinate r of charge position. Thus $\hat{r} = \hat{x}$, and the expectation value of the electric dipole is

$$< \vec{\mu}^{(e)} >= Tr\left(\vec{\mu}^{(e)}, \rho\right) = \hat{x}(\mu_{12}\rho_{21} + \mu_{21}\rho_{12}) \tag{2.110}$$

where $\mu_{12}^{(e)} =< 1|\mu^{(e)}|2 >$ and $\rho_{21}(t) = c_1^*(t)c_2(t)$. The trace in Eq. (2.110) is, in general, a sum over all states of the system. Here however, we assume that the dynamics are dominated by only two states. State 1 is the ground state and state 2 denotes the particular excited state that has minimum detuning from the incident light frequency and opposite parity with

respect to state 1. The quantities c_1 and c_2 are the probability amplitudes of state 1 and state 2, respectively.

The magnetic dipole transition moment for a one-photon interaction connecting states 2 and 3 is

$$\begin{aligned} <\vec{\mu}^{(m)}(t)>_{23} &= (e/2m)\int \psi_2^*(r,\theta,\phi,t)\vec{r}\times\vec{p}\psi_3(r,\theta,\phi,t)dV + h.c. \\ &= (e/2m)\int c_1^*(t)\psi_2^*(r,\theta,\phi)\vec{L}c_2(t)\psi_3(r,\theta,\phi)dV + h.c. \end{aligned} \tag{2.111}$$

in terms of the angular momentum operator $\vec{L} = \vec{r}\times\vec{p}$. It is important to note that states 2 and 3 may be excited sub-states or may be excited state admixtures into the ground state, as examined in more detail in the Heisenberg theory. In this case, the expectation value is given by the trace of the magnetic dipole operator $\vec{\mu}^{(m)} = (e/2m)\vec{L}$ with the density matrix:

$$<\vec{\mu}^{(m)}> = <2|\vec{\mu}^{(m)}|3>\rho_{32}(t) + h.c. = Tr\left(\vec{\mu}^{(m)},\rho\right) \tag{2.112}$$

At low intensities the magnetic moment is negligible for linear polarization, because the linear momentum $\vec{p}$ of the electron is very nearly parallel to its displacement. The Lorentz force is negligible compared to the force of the electric field at nonrelativistic intensities. The cross product in the integrand of Eq. (2.111) and the associated angular momentum are therefore nearly zero. Only an electric dipole oriented along $\hat{x}$ is induced. In the case of circular polarization, the electron follows the electric field adiabatically, circulating around the propagation axis, inducing a steady magnetic moment oriented along the z axis ($\vec{r}\times\vec{p}\neq 0$). This motion mediates the inverse Faraday effect caused by circularly polarized light [23], which is not of interest in this thesis. Consequently, in one-photon, electric-field-mediated interactions, only the angular momentum carried by the field $E(z,t)$, where z is the quantization axis, can be transferred to the atom. The initial and final states $|1>$ and $|2>$ must have the same magnetic quantum number m in the case of linear polarization, and must differ when the polarization is circular with $m_2 = m_1 \pm 1$.

In the case of an interaction mediated jointly by the E and B components of a linearly polarized field, the orientation of the magnetic moment is along the laboratory y axis, and its calculation is significantly different because two driving forces contribute to the motion. The Lorentz force causes the linear momentum induced by the electric field E to acquire a small transverse component that is azimuthal with respect to the B component of the optical field. We therefore introduce new source coordinates (r',θ',ϕ') with a polar axis along $B(z' = y')$. As before E defines the $\hat{x}' = \hat{x}$ axis. The third basis vector is $\hat{y}' = -\hat{z}$, and ϕ'

is considered to be measured from the $\hat{y}'$ axis. In this primed coordinate system the linear momentum may be written as $\vec{p}' = \hat{r}' p'_r + \hat{\theta}' p_{\theta'} + \hat{\phi}' p_{\phi'}$. The expression for the magnetic moment in Eq. (2.111) becomes

$$\begin{aligned} < \vec{\mu}^{(m)}(t) >_{23} &= (e/2m) \int \psi_2^*(r',\theta',\phi',t) \vec{r}' \times (\vec{p}_{r'} + \vec{p}_{\theta'} + \vec{p}_{\phi'}) \psi_3(r',\theta',\phi',t) dV' + h.c. \\ &= \frac{-e}{2m} \hat{y} \int \psi_2'(r',\theta',\psi',t) \vec{r}' p_{\phi'} \psi_3(r',\theta',\phi',t) dV' + h.c. \end{aligned} \tag{2.113}$$

since $\vec{r}' \times \vec{p}_{r'} = 0$ and $\hat{r}' \times (p_{\phi'} \hat{\phi}') = -p_{\phi'} \hat{y}$. Here the assumptions have been made that $p_{\theta'} \simeq 0$ (since neither field drives motion in the $\hat{\theta}'$ direction) and that r' is sufficiently slowly varying so that the amplitude of an oscillatory magnetic moment can be well defined and slowly varying too. Equation (2.113) is implicitly written in the rotating frame where the rapid time dependence is associated with the azimuthal momentum $p_{\phi'}$ and the magnetic moment points in the expected direction anti-parallel to the B field (along $-\hat{y}$).

Under the action of the forces due to orthogonal fields E and B, the time dependence of radial ($\hat{r}'$) and azimuthal ($\hat{\phi}'$) motions may differ. Hence we assume the wavefunction is separable according to $\psi(r',\theta',\phi',t) = \psi(r',t)\psi(\theta',\phi',t)$ and introduce separate c coefficients for the radial and angular parts of the wavefunction as follows: $\psi(r',t) = c^{(e)}(t)\psi(r')$ and $\psi(\theta',\phi',t) = c^{(m)}(t)\psi(\theta',\phi')$. Correspondingly, we define electric and magnetic density submatrices by $\rho_{ij}^{(e)} = c_j^{*(e)} c_i^{(e)}$ and $\rho_{ij}^{(m)} = c_j^{*(m)} c_i^{(m)}$ in the laboratory reference frame. The time development of $\rho_{ij}^{(e)}$ is determined by E, and that of $\rho_{ij}^{(m)}$ is determined by B. Both fields oscillate at the optical frequency, so by invoking the slowly varying envelope approximation (SVEA) the two submatrices can be written in the lab frame as

$$\rho^{(e)}(t) = \tilde{\rho}^{(e)} e^{i\omega t} \tag{2.114}$$

$$\rho^{(m)}(t) = \tilde{\rho}^{(m)} e^{\pm i\omega t} \tag{2.115}$$

where $\tilde{\rho}^{(e)}$ and $\tilde{\rho}^{(m)}$ designate the slowly varying amplitudes of the electric and magnetic coherences.

In terms of these quantities, the expression for the transverse magnetic moment in Eq (2.113) becomes

$$< \vec{\mu}^{(m)}(t) >= -\hat{y} < 2|\mu^{(m)}|3 > \rho_{32}^{(m)}(t) \tilde{\rho}_{21}^{(e)} + h.c. \tag{2.116}$$

where we have made the replacement $< 2|\mu^{(m)}|3 >=< 2|(e/2m) r' p_{\phi'}|3 >$. According to

Eq. (2.116), when the direction of the magnetic field is fixed along $\hat{y}$, the expectation value for the transverse magnetic moment is given by

$$< \vec{\mu}^{(m)}(t) >= -\hat{y}Tr(\mu^{(m)}, \rho^{(m)}\tilde{\rho}^{(e)}) \tag{2.117}$$

The main time dependence in this expression for the magnetic moment is associated with $\rho_{32}^{(m)}(t)$ in the rotating frame. The envelope of the electric contribution designated by $\tilde{\rho}_{21}^{(e)}$ is assumed to vary little during an optical period. The submatrices $\rho^{(m)}$ and $\rho^{(e)}$ are designated as magnetic and electric, using the superscripts m and e, because the former describes temporal evolution that is azimuthal with respect to the axis of the optical H field, while the latter describes radial oscillations of the wavefunction in the direction of E.

Note that the expectation value of the magnetic moment in Eq. (2.116) is second order in the wavefunction as expected, not fourth order. The full density matrix is just the product of the submatrices $\rho^{(m)}(t)$ and $\rho^{(e)}(t)$, given explicitly by

$$\rho = |\psi\rangle\langle\psi| = |\psi(r,t)\rangle|\psi(\theta,\phi,t)\rangle\langle\psi(\theta,\phi,t)|\langle\psi(r,t)| = \rho^{(m)}(t)\rho^{(e)}(t) \tag{2.118}$$

The submatrices $\rho^{(e)}(t)$ and $\rho^{(m)}(t)$ merely describe important degrees of freedom in the overall motion driven by applied fields E and B. In the next section these kinematically distinct submatrices are separately evaluated in order to calculate the induced magnetization and other moments that result from combined electric and magnetic forces.

2.2.3 Steady-state Solution of the Density Matrix

To write the total magneto-optical interaction consistent with any particular choice of reference frame requires some care. The reason for this is that interactions driven by EB involve motional effects of two orthogonal fields, one of which is a polar vector $(E(t))$ and the other of which $(B(t))$ is axial. The rotating frame of linear optical interactions governed by $E(t)$ alone, for example, has an axis along $\hat{z}$, whereas the magnetic moment induced by the combined action of $E(t)$ and $B(t)$ involves currents circulating about the $\hat{y}$ axis. In this thesis the joint effect of the electric and magnetic interactions will ultimately be described in the lab frame of reference, but to provide perspective on the kinematics, use will be made of a sequence of three reference frames. The calculation of dynamics begins in the rotating frame, is next transformed to the ordinary lab frame, and finally ends up in a z-adjusted lab frame.

Customarily, the rotating wave approximation is introduced in optical analysis to solve

for system dynamics. One result of this is that in the frame co-rotating with a circular component of $E(t)$, the induced electric dipole is a constant. For this reason the electric dipole interaction is written as $-\vec{\mu}^{(e)} \cdot \vec{E}(t)$, where only the field varies with time. However, in the same reference frame, the magnetic moment oscillates at the optical frequency. This is implied by Eq. (2.116) where magnetic charge oscillation varies rapidly with time as $\rho_{21}^{(m)} \propto exp(\pm i\omega t)$ whereas the electric coherence is only slowly varying. To include electric and magnetic interactions in an atom-field Hamiltonian referenced to a single frame, this must be taken into account.

The interaction Hamiltoniam in the rotating frame has the form

$$V(t) = -\frac{1}{2}\hbar \left[(\Omega_+^{*(m)} + \Omega_-^{*(m)}) + (\Omega_+^{(e)} + \Omega_+^{(m)} e^{i\phi}) e^{i\phi} + (\Omega_-^{(e)} + \Omega_-^{(m)} e^{-i\phi} \right] + h.c. \quad (2.119)$$

Here $\Omega_\pm^{(e)} \equiv \mu_\pm^{(e)} E_\pm/\hbar$ and $\Omega_\pm^{(m)} \equiv \mu_\pm^{(m)} B_\pm/\hbar$ are the electric and magnetic interaction terms for positive or negative $(\pm)$ helicity. The time dependence of the magnetic interaction either adds to or subtracts from that of the electric field, and produces interaction terms at frequencies of 0 and 2ω as shown by Eq. (2.119). The electric and magnetic transition matrix elements of V are therefore

$$V_{12}^{(e)} \equiv < 1|V^{(e)}|2 > = -\frac{1}{2}\hbar < 1|[\Omega_+^{(e)} + \Omega_-^{*(e)}]e^{i\phi} + h.c.|2 > \quad (2.120)$$

$$V_{23}^{(m)} \equiv < 2|V^{(m)}|3 > = -\frac{1}{2}\hbar < 2|[\Omega_+^{*(m)} + \Omega_-^{*(m)}] + h.c.|3 > -\frac{1}{2}\hbar < 2|[\Omega_+^{(m)} + \Omega_-^{*(m)}]e^{2i\phi} + h.c.|3 > \quad (2.121)$$

The charge oscillations induced by an electric field acting alone follow the time dependence of E. Hence the electric fieldeld induced coherence has the form $\rho_{12}^{(e)}(t) = \tilde{\rho}_{12}^{(e)} e^{i\phi}$ in the lab frame or $\rho_{12}^{(e)}(t) = \tilde{\rho}_{12}^{(e)}$ in the rotating frame. Charge oscillations that are jointly driven by electric and magnetic forces similarly follow the time dependence of the applied fields, and this gives rise to three distinct frequencies of oscillation in the lab frame, namely, 0 and $\pm 2\omega$, because there are combination terms in the product of the driving fields E and B.

$$\begin{aligned} E(t)B(t) &= \left(\frac{1}{2}E_0 e^{i\phi} + h.c.\right)\left(\frac{1}{2}B_0 e^{i\phi} + h.c.\right) \\ &= \frac{1}{4}(E_0 B_0 e^{2i\omega} + E_0^* B_0^* e^{-2i\omega} + E_0 B_0 + E_0^* B_0) \end{aligned} \quad (2.122)$$

The coherence between levels 1 and 3 is therefore expected to take the form

$$\rho_{13}(t) = \tilde{\rho}_{12}^{(e)}(\omega)\tilde{\rho}_{23}^{*(m)} + \tilde{\rho}_{12}^{(e)}(\omega)\tilde{\rho}_{23}^{(m)}(\omega)e^{2i\phi}$$
$$= \tilde{\rho}_{13}(\omega = 0) + \tilde{\rho}_{13}(2\omega)e^{2i\phi} \tag{2.123}$$

in the lab frame. Notice that the terms on the right hand side have the same time dependence as those in the magnetic interaction Hamiltonian of Eq. (2.121) and agree with the lab frame product of the magnetic and electric subma- trices given by Eqs. (2.115).

Equation (2.100) may now be solved directly for steady-state solutions by setting $\dot{\tilde{\rho}}_{12}^{(e)} = \dot{\tilde{\rho}}_{13}^{(m)} = 0$. We treat the electric interaction exactly, by applying it as a strong field in zeroth order ($V^{(0)}(t) = -\vec{\mu}^{(e)} \cdot \vec{E}(t)$). The magnetic dipole interaction is then applied as a perturbation in concert with the electric dipole interaction in first order ($V^{(1)} = -\vec{\mu}^{(e)} \cdot \vec{E}(t) - \vec{\mu}^{(m)}(t) \cdot \vec{B}(t)$), and the equation of motion is solved for the submatrix coherences by collecting terms at each frequency.

This procedure yields first-order results for the coherences, which are

$$\rho_{12}^{(e)} = \frac{1}{2}\left(\frac{(\Omega_+^{(e)} + \Omega_-^{*(e)})_{12}}{(\Delta_1 + i\Gamma_{12})}e^{i\omega t}\right)(\rho_{11} - \rho_{22}) \tag{2.124}$$

$$\rho_{23}^{(m)} = \frac{1}{2}\left(\frac{(\Omega_+^{'(m)} + \Omega_-^{'(m)})_{23}}{(\omega_0 + i\Gamma_{23}^{(m)})}e^{-i\omega t} + \frac{\Omega_+^{(m)} + \Omega_-^{*(m)})_{23}}{(\Delta_2 + i\Gamma_{23}^{(m)})}e^{i\omega t}\right)(\rho_{11}^0 - \rho_{22}^0) \tag{2.125}$$

in the lab frame. Here the counter-rotating magnetic amplitude that gives rise to the time-independent term in is designated by $\Omega_\pm^{'(m)} \equiv \mu_\mp^{(m)} B_\pm^*/\hbar$. The detunings in the resonant denominators are defined by $\Delta_1 \equiv \omega_0 - \omega$ and $\Delta_2 \equiv \omega_0 - 2\omega$ if the magnetic transitions are assumed to take place in the excited state. For ground state magnetic transitions, the denominators in Eq. (2.125) are $\omega_\phi + i\Gamma_{23}$ and $\Delta_2 + i\Gamma_{23}$ with $\Delta_2 \equiv \omega_\phi - 2\omega$. In obtaining Eq. (2.125) the magnetic interaction has been treated as a perturbation, so the population difference equals the initial value, which may be assumed to correspond to the ground state $(\rho_{11}^{(0)} - \rho_{22}^{(0)}) = 1$. Population saturation effects due to the electric interaction are nevertheless taken into account when the electric field interaction is applied a second time to obtain the first-order result. The population difference $(\rho_{11} - \rho_{22})$ that appears in Eq. (2.125) is then given by

$$\rho_{11}-\rho_{22}=\left(1+\frac{\Gamma_{12}^{(e)}|\Omega_{+}^{(e)}+\Omega_{-}^{*(e)}|^2}{\gamma_{22}(\Delta_1^2+\Gamma_{12}^{(e)2})}\right)^{-1} \tag{2.126}$$

2.2.4 Calculation of Transverse Optical Magnetization

The steady-state solution for the magnetization $\vec{M}$the same macroscopic magnetization that appears in the constitutive relation $\vec{B}=\mu_0(\vec{H}+\vec{M})$ associated with Maxwells equationsis given in the lab frame by

$$\begin{aligned}\vec{M} &= NTr(\vec{\mu}^{(m)}(t),\rho(t)) \\ &= NTr(\vec{\mu}^{(m)}(t),\rho^{(m)}(t)\rho^{(e)}(t)) \\ &= -N\hat{y}(<3|\mu^{(m)}(t)|2>\rho_{23}^{(m)}(t)\rho_{12}^{(e)}(t)+h.c.)\end{aligned} \tag{2.127}$$

Here $\vec{M}$ is referenced to laboratory coordinates (x,y,z), which parallel the directions of E, B, and the propagation axis, respectively. Shortly we shall transform to a z-corrected lab frame with coordinates (x,y,z) in which the theory can be compared directly with experiments that involve projections of circular currents on the x and z axes.

With the results of Eqs. (2.125) in hand, we now specialize to the case of linear polarization. Upon substitution of the coherences (2.125) into , the magnetization yields the result

$$\begin{aligned}\vec{M}(t) = -\hat{y}\left(\frac{Ne}{2m}\right)\Bigg(\frac{1}{2}\Bigg(&\frac{<3|L_y|2>(\Omega_0^{(e)})_{12}(\Omega_0^{(m)})_{23}}{(\Delta_1+i\Gamma_{12}^{(e)})(\Delta_2+i\Gamma_{23}^{(m)})}e^{i\omega t} \\ &+\frac{<2|L_y|1>(\Omega_0^{(e)})_{12}(\Omega_0^{'(m)})_{23}}{(\omega_0+i\Gamma_{12}^{(e)})(\Delta_2+i\Gamma_{23}^{(m)})}e^{-i\omega t}\Bigg)+h.c.\Bigg)(\rho_{11}-\rho_{22})\end{aligned} \tag{2.128}$$

This expression is valid in the lab frame where $\mu_{21}^{(m)}\propto e^{-i\omega t}$. The field factors are $\Omega_0^{'(m)}=\mu_0^{(m)}B_0^*/\hbar$, $\Omega_0^{(m)}=\mu_0^{(m)}B_0/\hbar$, and $\Omega_0^{(e)}=\mu_0^{(e)}E_0/\hbar$. Only one circular component of the electric field interaction contributes to $\vec{M}(t)$, whereas both circular components of the magnetic interaction participate. Hence the specific replacement $\Omega_0^{(m)}=(\Omega_+^{(m)}+\Omega_-^{*(m)})$ has been made for the magnetic term, and $\Omega_0^{(e)}=1/2(\Omega_+^{(e)}+\Omega_-^{*(e)})$ for the electric term. This

consideration removes one factor of 2 from the denominator of the expression for $\vec{M}$.

The magnetization has the general form

$$\vec{M} = \frac{1}{2}\tilde{M}e^{i\phi} + h.c. \tag{2.129}$$

where the slowly varying amplitude $\tilde{M}$ is given by

$$\tilde{M} = -\hat{y}\left(\frac{Ne}{m}\right)\frac{1}{2}\left(\frac{<3|L_y|2>(\Omega_0^{(e)})_{12}(\Omega_0^{(m)})_{23}}{(\delta_1 + i\Gamma_{12}^{(e)})(\Delta_2 + i\Gamma_{23}^{(m)})} + \frac{<3|L_y|2>^*(\Omega_0^{*(e)})_{12}(\Omega_0^{'(m)*})_{23}}{(\omega_0 - i\Gamma_{12}^{(e)})(\Delta_2 - i\Gamma_{23}^{(m)})}\right)(\rho_{11} - \rho_{22}) \tag{2.130}$$

Notice that although the process giving rise to this magnetization is second order in the incident fields, the magnetic dipole oscillates at the fundamental frequency ω not 2ω.

Before we can determine the dimensionless ratio R of magnetic to electric-dipole moments as a function of incident field strength, we must account for the axial versus polar nature of MD and ED moments. An adjustment is needed to account for the fact that of all the electrons that can be set in motion by the electric field to produce polarization P within a given volume, at most one half can be deflected to contribute to a magnetic moment M in the same volume [2]. For a given number of charges per unit volume, the amplitude of the oscillatory magnetization must therefore be corrected by another factor of 2 before direct comparison with the amplitude of electric polarization is possible.

This correction is equivalent to a transformation $(x,y,z) \rightarrow (x,y,2z)$ that rescales the laboratory z coordinate, since oscillatory motion in an arc about B resolves itself differently on the Cartesian x and z axes (See [2] for further discussion). Circular arc motion projected onto $\hat{z}$ reverses twice as often as the same motion projected on $\hat{x}$. As a result, the amplitude of magnetic charge oscillations projected onto the propagation axis must be halved for comparison with the amplitude of electric dipole oscillation measured along $\hat{x}$. The halving of the z amplitude may be taken into account with the substitution $L_y \rightarrow 2L_y$ in Eq. (2.130). We also note that the second term in Eq. (2.130) is much smaller than the first due to the ω_0 factor in the denominator. To an excellent approximation our expression for the radiant magnetization at the optical frequency therefore reduces to

$$\tilde{M} = -\hat{y}M\left(\frac{e}{m}\right)\frac{<3|L_y|2>\Omega_0^{(e)}\Omega_0^{(m)}}{(\Delta_1 + i\Gamma_{12}^{(e)})(\Delta_2 + i\Gamma_{23}^{(m)})}(\rho_{11} - \rho_{22}) \tag{2.131}$$

The dimensionless ratio of magnetic to electric moments is therefore given by

$$R = \left|\frac{\tilde{M}}{c\tilde{P}}\right| = \left|\left(\frac{e}{mc}\right)\frac{<3|L_y|2>\tilde{\rho}_{12}^{(e)}\tilde{\rho}_{23}^{(m)}}{<2|ex|1>\tilde{\rho}_{12}^{(e)}}\right|$$
$$= \left|\left(\frac{<2|x(p_\phi/mc)|1>}{<2|x|1>}\right)\tilde{\rho}_{23}^{(m)}\right| \tag{2.132}$$

Since the momentum $< p_\phi >$ of charge motion cannot exceed $< p_\phi >= mc$, the ratio of matrix elements in parentheses on the right side of Eq. (2.2.4) cannot exceed unity. Also, the maximum value of the off-diagonal matrix element $\tilde{\rho}_{23}^{(m)}$ is 1/2 (see [22]). So the ratio R has a maximum value that is also 1/2. Though not obvious from the form of Eq. (2.2.4), it is important to note that the ratio of magnetic to electric susceptibility can attain the maximum value of 1/2 at nonrelativistic intensities. This may be demonstrated by direct numerical integration of the equations of motion [15]. Ultrafast growth (on a timescale $\Delta t < 100 fs$ [1]) of magnetic response takes place via energy transfer from electric field-induced linear motion along x, to the azimuthal motion initiated by the magnetic field along $\hat{\phi}'$, and is due to the phenomenon of parametric resonance [18].

The development to this stage can be summarized in a few points. The radiant magnetic emission intensity is predicted to be quadratic with respect to the input intensity. It may be enhanced by electronic resonance at $\Delta_1 = 0$ and is governed secondarily by a parametric detuning factor $(\Delta_2 + i\Gamma)^{-1}$. It can grow to a value of, at most, one fourth ($R_{max}^2 = 1/4$) that of the electric dipole emission intensity. These findings are in excellent agreement with experimental results [2] at intensities ten orders of magnitude below the relativistic threshold.

To calculate the magnetic susceptibility, and to compare it with the electric susceptibility, we now make use of Eq. (2.131).

$$\chi^{(m)} = \frac{\tilde{M}}{H_0} = \left(\frac{-Ne}{mH_0}\right)\left(\frac{<3|L_y|2>\hbar\Omega_0^{(e)}\hbar\Omega_0^{(m)}}{\hbar^2(\Delta_1 + i\Gamma_{12}^{(e)})(\Delta_2 + i\Gamma_{12}^{(m)})}\right)(\rho_{11} - \rho_{22})$$
$$= \left(\frac{-N\mu_0 e^3}{2m^2\hbar^2}\right)\left(\frac{|<3|L_y|2>|^2 <1|x|2>}{(\Delta_1 + i\Gamma_{12}^{(e)})(\Delta_2 + i\Gamma_{23}^{(m)})}\right)(\rho_{11} - \rho_{22})E_0 \tag{2.133}$$

The electric susceptibility $\chi^{(e)}$ may similarly be determined by comparing its defining

relationship, namely,

$$P(t) = \frac{1}{2}\tilde{P}e^{i\omega t} + h.c. = \frac{1}{2}\varepsilon_0\chi^{(e)}(-\omega)E_0e^{i\omega t} + h.c. \tag{2.134}$$

with Eqs. (2.110) and (2.125). This yields

$$\tilde{P} = 2N\mu_{21}\tilde{\rho}_{12}^{(e)} = \left(\frac{Ne^2}{\hbar}\right)\left(\frac{|<1|x|2>|^2E_0}{(\Delta_1 + i\Gamma_{12}^{(e)})}\right)(\rho_{11} - \rho_{22}) \tag{2.135}$$

$$\chi^{(e)} = \left(\frac{Ne^2}{\varepsilon_0\hbar}\right)\frac{|<2|x|1>|^2}{(\Delta_1 + i\Gamma_{12}^{(e)})} \tag{2.136}$$

In all expressions to this point, local field renormalization has been ignored. The ratio of magnetic and electric susceptibilities obtained from these results is

$$\begin{aligned}\frac{\chi^{(m)}(\omega)}{\chi^{(e)}(\omega)} &= \left(\frac{-\mu_0\varepsilon_0 e}{2m^2\hbar}\right)\frac{|<3|L_y|2>|^2E_0}{<2|x|1>(\Delta_2 + i\Gamma_{23}^{(m)})} \\ &= \frac{-2}{\hbar c^2}\frac{|<2|\mu^{(m)}|1>|^2E_0e^{-i\phi_p}}{<2|\mu^{(e)}|1>\sqrt{\Delta_2^2 + \Gamma_{23}^{2(m)}}}\end{aligned} \tag{2.137}$$

where $\phi_p \equiv \tan^{-1}(\Gamma_{23}^{(m)}/\Delta_2)$. Note that, in the vicinity of electronic resonance where magnetic dispersion is largest, the magnetic linewidth is expected to be much less than the parametric detuning factor ($\Gamma_{23}^{(m)} \ll \Delta_2$). Therefore $\phi_p \simeq 0$ and the signs of electric and magnetic dispersion are opposite, as depicted in Fig. 1. The matrix element in the numerator of Eq. (2.137) reflects transformation of the magnetic susceptibility as a rotation $R(y)$ about the y axis. According to Eq. (2.133), the magnetic susceptibility is also proportional to the electric dipole transition moment. Hence the matrix elements $<3|L_y|2>$ and $<1|x|2>$ must both be nonzero for optical magnetization to be allowed, and the electric field amplitude E_0 must be large for it to be intense. The issue of whether magnetic transitions are considered to take place in the excited state or ground state is deferred to Section 2.3.

Some further comments about selection rules are in order. Explicit evaluation of the magnetic matrix element between states of well-defined total initial and final angular momentum l_1 and l_2, respectively, using the Wigner-Eckart theorem [24], yields

$$< 3|V_{\pm}^{(m)}|2 >= (-)^{l_3-m_3}\frac{1}{2}(B_{\pm} < \alpha_3 l_3 m_3 \| \mu_{\mp}^{(m)} \| \alpha_2 l_2 m_2 > + c.c.) \times \begin{pmatrix} l_3 & 1 & l_2 \\ -m_3 & q & m_2 \end{pmatrix} \tag{2.138}$$

Here α_2 and α_3 refer collectively to any quantum numbers other than l and m needed to specify the initial and final states exactly. MD and ED interaction matrix elements are proportional to the same 3-j symbol, but their reduced matrix elements transform as rotations about $\hat{y}$ and translations along $\hat{x}$, respectively. Equation (2.138) indicates explicitly that magnetic interactions induced by circularly polarized components of the B field ($q = \pm 1$) exchange spin angular momentum of $\pm\hbar$ with the atom. By contrast, linearly polarized fields ($q = 0$) exchange no spin angular momentum with the atom. Nevertheless, at moderate intensities, the combined action of linearly polarized E and B fields can drive the formation of a parametrically enhanced, oscillating transverse orbital angular momentum as specified by Eq. (2.131). For this to happen, the reduced matrix elements of L_y and x must be simultaneously nonzero, and the selection rules $\Delta l_{12} = \pm 1$, $\Delta m_{12} = m_2 - m_1 = 0$,$\Delta l_{23} = 0$, and $\Delta m_{23} = \pm 1$ must be satisfied.

2.2.5 Second-harmonic and DC Electric Dipole Processes

Electric dipole moments can also be generated by the joint action of optical E and B fields. Two additional processes emerge from this analysis by considering expectation values of the electric dipole operator in combination with the magneto-electric coherences developed in Eq. (2.125). One process yields a radiant polarization at the second-harmonic frequency, and the other produces a static electric dipole in the direction of propagation of light.

We now consider electric dipole moments that develop perpendicular to $\hat{x}$ and $\hat{y}$. A z-directed, magnetically induced electric dipole moment is clearly distinct from either the linear electric dipole induced along $\hat{x}$ or the non-linear magnetic dipole induced along $\hat{y}$. Its macroscopic polarization is calculated using

$$\vec{P} = NTr(\vec{\mu}^{(e)}, \rho(t)) \tag{2.139}$$

where

$$\vec{\mu}^{(e)} = \mu_0^{(e)}\hat{z} \tag{2.140}$$

By substituting Eq. (2.125), and (2.140) into Eq. (2.139), and specializing again to the case of linear input polarization, one finds in the Cartesian lab frame where the charge oscillation along z is at a doubled frequency (i.e., $(\mu_{21}^{(e)})_z \propto e^{-2i\omega t}$) that

$$\begin{aligned}\vec{P}(t) &= N\hat{z}(\mu_{31}^{(e)}\rho_{23}^{(m)}(t)\rho_{12}^{(e)} + h.c.) \\ &= N\hat{z}\left[\left(\frac{1}{2}\frac{\mu_{31}^{(e)}(\Omega_0^{'(m)})_{23}(\Omega_0^{(e)})_{12}}{(\Delta_1 + i\Gamma_{12}^{(e)})(\omega_0 + i\Gamma_{23}^{(m)})}e^{-2i\omega t} + h.c.\right) + \left(\frac{1}{2}\frac{\mu_{31}^{(e)}(\Omega_0^{(m)})_{23}(\Omega_0^{(e)})_{12}}{(\Delta_1 + i\Gamma_{12}^{(e)})(\Delta_2 + i\Gamma_{23}^{(m)})} + h.c.\right)\right]\end{aligned} \tag{2.141}$$

This expression for the electric polarization driven jointly by E and B contains two terms of different frequency. The first is a field at 2ω that generates second-harmonic radiation. Unlike the magnetization at frequency ω in Eq. (2.131), the second-harmonic signal is longitudinally polarized and lacks the parametric resonance factor $(\Delta_2 + i\Gamma)^{-1}$, so it is expected to produce only weak emission perpendicular to the pump wave. The second term is a zero-frequency term that predicts a static charge separation induced by light in dielectric media illuminated by moderately intense coherent light. Since it originates from the oscillatory coherence in Eq. (2.125) and contains the same parametric denominator as the magnetization in Eq. (2.131), its magnitude is expected to be strongly enhanced. In ultrashort pulse interactions, this effect will therefore generate intense longitudinally polarized terahertz radiation, although conventional phase-matching of the output will not be possible.

These same optical effects were predicted previously using steady-state analysis of a classical model of electron motion subject to external electric and magnetic forcing fields and Hookes law restoring forces [15]. The present density matrix treatment has the merit of identifying the relative intensities, detuning dependences, emission frequencies, selection rules, directionality and multipole character of these effects in an independent, systematic way that requires no interpretation and is valid near resonances.

2.3 Heisenberg Theory of Transverse Optical Magnetism

In this section we consider a simple solution to the dynamics of a nominally 2-level system with an allowed transition between an $L = 0$ ground state and $L = 1$ excited state as a check on the density matrix approach. The macroscopic polarization P and magnetization M induced in such a system by a 2-photon process in which the optical E and B fields each act once they are calculated.

The equation of motion of an operator $\hat{O}_H$ in the Heisenberg picture is

$$\frac{d\hat{O}}{dt} = \frac{i}{\hbar}[H_0, \hat{O}] + \frac{i}{\hbar}[V, \hat{O}] - \Gamma\hat{O} \tag{2.142}$$

where $\Gamma\hat{O}$ has been added to account for phenomenological damping. The calculation is semi-classical and proceeds by finding the amplitude of the electric dipole moment that develops on the atom as the result of the action of the electric field followed by determination of the magnetic dipole induced by the magnetic field.

For linear input polarization, a superposition state is formed between the eigenstates $|100>$ and $|210>$ in the first step. In fully quantized, dressed state theory, this results in new quasistates with equal but opposite admixtures of the second state.

$$|D(n)>_+ = \sin\theta|1,n> + \cos\theta|2,n-1> \tag{2.143}$$

$$|D(n)>_- = \cos\theta|1,n> - \sin\theta|2,n-1> \tag{2.144}$$

where

$$\sin(2\theta) = \frac{2g\sqrt{n}}{\Omega_R} = \frac{\Omega}{\Omega_R} \tag{2.145}$$

$$\cos(2\omega) = \frac{\Delta}{\Omega_R} \tag{2.146}$$

$$\Omega_R \equiv \sqrt{\Delta^2 + 4g^2 n} \tag{2.147}$$

Thus, on the basis of this exact procedure, it is expected that the excited state acquires some ground state character and the ground state acquires some excited state character. The second step of a coherent, 2-photon magneto-electric transition can therefore proceed in two ways. The second interaction can be thought of as taking place in the ground or excited state. These two possibilities can be pictured as the following sequences.

$$|1>\equiv|100>\xrightarrow{E}|2>=\sin\theta|1>+\cos\theta|2>\xrightarrow[exc.st.]{B}|3>=a|211>+b|21-1>+c|210> \tag{2.148}$$

$$|1>\equiv|100>\xrightarrow{E}|2'>=\cos\theta|1>-\sin\theta|2>\xrightarrow[gr.st.]{B}|3'>=a'|211>+b'|21-1>+c'|210> \tag{2.149}$$

Three dipole moments can then form in state$|3'>$ for example.

$$P(0)=N<1|\mu^{(e)}(0)|3'>\hat{z}\neq 0 \tag{2.150}$$

$$P(2\omega)=N<1|\mu^{(e)}(2\omega)|3'>\hat{z}\neq 0 \tag{2.151}$$

$$M(\omega)=-N<2'|\mu^{(m)}(\omega)|3'>\hat{y}\neq 0 \tag{2.152}$$

The electric dipole moments $P(0)$ and $P(2\omega)$ appear to violate Laporte's rule requiring a change of parity for a non-zero dipole matrix element. That is, they form in the ground state which has a single parity if inversion symmetry is present. However $|2'>$ and $|3'>$ are not stationary states. Both these states are superpositions of mixed partiy. Hence, the matrix elements $<1|\mu^{(e)}(0)|3'>$, $<1|\mu^{(e)}(2\omega)|3'>$, and $<2'|\mu^{(m)}(\omega)|3'>$ can all simultaneously be non-zero, although they are computed between components of a nominally single energy level.

To incorporate the mutual state mixing of states $|100>$ and $|210>$ without appealing to dressed state theory, it is necessary to introduce a new concept in atomic physics. This concept is closely related to that of "'holes"' in semiconductor solid state theory. Here, however, we shall refer to it as "'conjugate particle excitation"'. It provides a consistent picture of the conjugate term in the ED rotating wave approximation as the excitation of a conjugate electron in a negative frequency space. Consider the ED operator expression

$$\hat{\mu}^{(e)}=\frac{1}{2}\mu_0^{(e)}\left(\sigma_+e^{i\omega t}+\sigma_+^{\dagger}e^{-i\omega t}\right) \tag{2.153}$$

Ordinarily the second term would yield zero when operating on the ground state. Here it is retained because it represents the creation of a conjugate excitation that mixes $|210>$ into the ground state wavefunction. In essence, it creates a "'hole"' in the ground state wavefunction that has $|210>$ character and must be included in the dynamics because it corresponds to a secular term in the interaction potential. This interpretation is in complete

agreement with dressed state theory.

To proceed, we adopt a Heisenberg picture of the dynamics and use Eq. (2.142) to follow the time evolution of the system during sequential ED and MD interactions. By solving for the ED and MD operators one can find the macroscopic polarization and magnetization between and two states using the expressions

$$P = \frac{1}{2}\tilde{P}e^{i\omega t} + h.c. \tag{2.154}$$

$$M = \frac{1}{2}\tilde{M}e^{i\omega t} + h.c. \tag{2.155}$$

where

$$\tilde{P} = N\mu^{(e)} \tag{2.156}$$

$$\tilde{M} = N\mu^{(m)} \tag{2.157}$$

The electric interaction is assumed to take place first and the magnetic interaction is a subsequent perturbation. Hence the electric dipole operates first between the states $|1>\equiv|100>$ and $|2>=|210>$. The static Hamiltonian has the form

$$H_0 = \hbar\omega_1|1><1| + \hbar\omega_2|2><2| \tag{2.158}$$

Taking the zero of energy to be at the level of state $|1>$ and defining the resonant frequency to be $\omega_0 \equiv \omega_2 - \omega_1$, this Hamiltonian can be written in the 2-state basis as the matrix operator

$$H_0 = \hbar\begin{pmatrix}\omega_0 & 0\\ 0 & 0\end{pmatrix} \tag{2.159}$$

or in terms of Pauli matrices

$$H_0 = \frac{\hbar\omega_0}{2}(\sigma_z + \sigma_I) \tag{2.160}$$

To solve the Heisenberg equation of motion the interaction Hamiltonian must also be

expressed in irreducible form. For an electric dipole process, the interaction may be found by substituting tensorial expressions for the moment and the field into the customary relation:

$$V^{(e)} = -\vec{\mu}^{(e)} \cdot \vec{E} \tag{2.161}$$

The vector fields have irreducible representations of

$$\vec{E}(t) = -\frac{1}{2}\left[E_+ \hat{\varepsilon}_- + E_- \hat{\varepsilon}_+\right] e^{i\omega t} + h.c. \tag{2.162}$$

$$\vec{B}(t) = -\frac{i}{2}\left[B_+ \hat{\varepsilon}_- - B_- \hat{\varepsilon}_+\right] e^{i\omega t} + h.c. \tag{2.163}$$

where $\hat{\varepsilon}_\pm \equiv \mp\left(\frac{\hat{x} \pm i\hat{y}}{\sqrt{2}}\right)$. Also, the electric dipole moment has the irreducible vector representation (most generally):

$$\vec{\mu}^{(e)} = \frac{1}{2}\left(-\mu_-^{(e)}(\omega)\hat{\varepsilon}_+ - \mu_+^{(e)}(\omega)\hat{\varepsilon}_- + \mu_0^{(e)}(\omega)\hat{\varepsilon}_0\right) e^{i\omega t} + h.c. \tag{2.164}$$

In operator form this is

$$\hat{\mu}^{(e)} = \frac{1}{2}\left(-\mu_-^{(e)}(\omega)\hat{\sigma}_+ - \mu_+^{(e)}(\omega)\hat{\sigma}_- + \mu_0^{(e)}(\omega)\hat{\sigma}_z\right) e^{i\omega t} + h.c. \tag{2.165}$$

for a one-photon moment. By substituting (2.162) and (2.164) into (2.161), the semi-classical interaction Hamiltonian is therefore found to be

$$\begin{aligned} V^{(e)} &= -\vec{\mu}^{(e)} \cdot \vec{E} \\ &= (-)^2 \left[\frac{1}{2}\left(\mu_-^{(e)}\hat{\varepsilon}_+ + \mu_+^{(e)}\hat{\varepsilon}_- - \mu_0\hat{\varepsilon}_0\right) e^{i\omega t} + c.c.\right] \cdot \left[\frac{1}{2}\left(E_+\hat{\varepsilon}_- + E_-\hat{\varepsilon}_+\right) e^{i\omega t} + c.c.\right] \end{aligned} \tag{2.166}$$

The scalar products of the circular basis vectors $\hat{\varepsilon}_q$ can be summarized as

$$\hat{\varepsilon}_q \cdot \hat{\varepsilon}_p = \begin{cases} 0 & q = p \neq 0 \\ -1 & q \neq p \neq 0 \\ 0 & q = 0, p \neq 0 \\ 1 & q = p = 0 \end{cases} \quad \hat{\varepsilon}_q^* = -\hat{\varepsilon}_{-q} \tag{2.167}$$

Hence, one finds that the expression for the interaction Hamiltonian reduces to

$$\begin{aligned} V^{(e)} =& \frac{1}{4}\Big[-\mu_-^{(e)}(\omega)E_+e^{2i\omega t} + \mu_-^{(e)}(\omega)E_-^* - \mu_+^{(e)}(\omega)E_-e^{2i\omega t} + \mu_+^{(e)}(\omega)E_+^* \\ & -\mu_-^{(e)*}(\omega)E_+^* + \mu_-^{(e)*}(\omega)E_-e^{-2i\omega t} - \mu_+^{(e)*}(\omega)E_-^* + \mu_+^{(e)*}(\omega)E_+e^{-2i\omega t}\Big] \end{aligned} \tag{2.168}$$

Making the secular approximation (by dropping the explicitly time-dependent terms) we find

$$\begin{aligned} V^{(e)} &= \frac{1}{4}\left[\mu_-^{(e)}(\omega)E_-^* + \mu_+^{(e)}(\omega)E_+^* - \mu_-^{(e)*}(\omega)E_+^* - \mu_+^{(e)*}(\omega)E_-^*\right] \\ &= \frac{1}{4}\left[-\mu_-^{(e)}(\omega)E_+ - \mu_+^{(e)}(\omega)E_- - \mu_-^{(e)*}(\omega)E_+^* - \mu_+^{(e)*}(\omega)E_-^*\right] \\ &= -\frac{1}{4}\left[\left(\mu_-^{(e)}(\omega)E_+ + \mu_+^{(e)}(\omega)E_-\right) + h.c.\right] \\ &= -\frac{1}{4}\left[\left(\hbar\Omega_-^{(e)} + \hbar\Omega_+^{(e)}\right) + h.c.\right] \end{aligned} \tag{2.169}$$

where $\Omega_\pm^{(e)} \equiv \frac{\mu_\pm^{(e)} E_\pm}{\hbar}$. For linear polarization, the additional substitutions may be made:

$$\mu_\pm^{(e)} = \frac{\mu_0^{(e)}}{\sqrt{2}} \tag{2.170}$$

$$E_\pm = \frac{E_0}{\sqrt{2}} \tag{2.171}$$

So finally the interaction Hamiltonian becomes

$$\begin{aligned} V^{(e)} &= -\frac{1}{4}\left[\left(\frac{\hbar\Omega_0^{(e)}}{2} + \frac{\hbar\Omega_0^{(e)}}{2}\right) + h.c.\right] \\ &= -\frac{1}{4}\left[\hbar\Omega_0^{(e)} + h.c.\right] \end{aligned} \tag{2.172}$$

Since this interaction can cause transitions up and down, its semi-classical operator form is

$$V^{(e)} = -\frac{1}{4}\hbar\Omega_0^{(e)}\left(\sigma_+ + \sigma_-\right) \tag{2.173}$$

To solve the Heisenberg equations of motion, commutators of the operators with the Hamiltonian are needed. To find the temporal evolution of $\mu^{(e)}$, we need $[H_0, \mu^{(e)}]$ and $[V^{(e)}, \mu^{(e)}]$ are therefore needed.

$$\begin{aligned}
[H_0, \mu^{(e)}] &= \frac{\hbar\omega_0}{4}(\sigma_z + \sigma_I)\left[\left(-\mu_-^{(e)}\sigma_+ - \mu_+^{(e)}\sigma_- + \mu_0^{(e)}\sigma_z\right)e^{i\omega t} + h.c.\right] \\
&\quad - \frac{\hbar\omega_0}{4}\left[\left(-\mu_-^{(e)}\sigma_+ - \mu_+^{(e)}\sigma_- + \mu_0^{(e)}\sigma_z\right)e^{i\omega t} + h.c.\right](\sigma_z + \sigma_I) \\
&= -\frac{\hbar\omega_0}{4}\left[\left(\mu_-^{(e)}[\sigma_+, \sigma_z]e^{i\omega t} + \mu_+^{(e)}[\sigma_-, \sigma_z]e^{i\omega t}\right) + h.c.\right] \\
&= -\frac{\hbar\omega_0}{2}\left[\left(\mu_-^{(e)}\sigma_+ - \mu_+(e)\sigma_-\right)e^{i\omega t} + h.c.\right] \qquad (2.174) \\
[V^{(e)}, \mu^{(e)}] &= -\frac{\hbar\Omega_0}{4}(\sigma_+ + \sigma_-)\left[\left(-\mu_-^{(e)}\sigma_+ - \mu_+^{(e)}\sigma_- + \mu_0^{(e)}\sigma_z\right)e^{i\omega t} + h.c.\right] \\
&\quad + \frac{\hbar\Omega_0}{4}\left[\left(-\mu_-^{(e)}\sigma_+ - \mu_+^{(e)}\sigma_- + \mu_0^{(e)}\sigma_z\right)e^{i\omega t} + h.c.\right](\sigma_+ + \sigma_-) \\
&= \frac{\hbar\Omega_0}{4}\left[\left(\mu_+^{(e)}[\sigma_+, \sigma_-] + \mu_0^{(e)}[\sigma_z, \sigma_+] + \mu_-^{(e)}[\sigma_-, \sigma_+] + \mu_0^{(e)}[\sigma_z, \sigma_-]\right)e^{i\omega t}\right. \\
&\quad \left.\left(\mu_-^{(e)*}[\sigma_+, \sigma_-] + \mu_0^{(e)*}[\sigma_z, \sigma_+] + \mu_+^{(e)*}[\sigma_-, \sigma_+] + \mu_0^{(e)*}[\sigma_z, \sigma_-]\right)e^{-i\omega t}\right] \qquad (2.175) \\
&= \frac{\hbar\Omega_0}{4}\left[\left(\mu_+^{(e)}\sigma_z + 2\mu_0^{(e)}\sigma_+ - \mu_-^{(e)}\sigma_z - 2\mu_0^{(e)}\sigma_-\right)e^{i\omega t}\right. \\
&\quad \left.\left(\mu_-^{(e)*}\sigma_z + 2\mu_0^{(e)*}\sigma_+ - \mu_+^{(e)*}\sigma_z - 2\mu_0^{(e)*}\sigma_-\right)e^{-i\omega t}\right] \qquad (2.176)
\end{aligned}$$

2.3.1 The Electric Interaction

With $\mu^{(e)}$, $[H_0, \mu^{(e)}]$, and $[V^{(e)}, \mu^{(e)}]$ evaluated we now proceed to solve the Heisenberg equation for the time depencence of the electric dipole operator $\mu^{(e)}$.

$$\frac{d\mu^{(e)}}{dt} = \frac{i}{\hbar}[H_0, \mu^{(e)}] + \frac{i}{\hbar}[V^{(e)}, \mu^{(e)}] - \Gamma\mu^{(e)} \tag{2.177}$$

The positive frequency terms yield

$$\frac{i\omega}{2}\left(-\mu_-^{(e)}\sigma_+ - \mu_+^{(e)}\sigma_- + \mu_0^{(e)}\sigma_z\right)e^{i\omega t} = -\frac{i\omega_0}{2}\left(\mu_-^{(e)}\sigma_+ - \mu_+(e)\sigma_-\right)e^{i\omega t} + \frac{i\Omega_0}{4}\left(\mu_+^{(e)}\sigma_z + 2\mu_0^{(e)}\sigma_+ - \mu_-^{(e)}\sigma_z - 2\mu_0^{(e)}\sigma_-\right)e^{i\omega t} - \frac{\Gamma}{2}\left(-\mu_-^{(e)}\sigma_+ - \mu_+^{(e)}\sigma_- + \mu_0^{(e)}\sigma_z\right)e^{i\omega t} \tag{2.178}$$

We solve for each of the amplitudes separately, beginning with $\mu_-^{(e)}$

$$-\frac{i\omega}{2}\mu_-^{(e)}(\omega) = -\frac{i\omega_0}{2}\mu_-^{(e)}(\omega) + \frac{i\Omega_0}{2}\mu_0^{(e)}(\omega) + \Gamma\mu_-^{(e)}(\omega) \tag{2.179}$$

$$\left(-\frac{i\omega}{2} + \frac{i\omega_0}{2} - \frac{\Gamma}{2}\right)\mu_-^{(e)}(\omega) = \frac{i\Omega_0}{2}\mu_0^{(e)}(\omega) \tag{2.180}$$

$$(\Delta_1 + i\Gamma)\,\mu_-^{(e)}(\omega) = \Omega_0\mu_0^{(e)}(\omega) \tag{2.181}$$

$$\mu_-^{(e)}(\omega) = \frac{\Omega_0\mu_0^{(e)}(\omega)}{(\omega_0 - \omega) + i\Gamma} \tag{2.182}$$

Similarly we find

$$\mu_+^{(e)}(\omega) = \frac{\Omega_0\mu_0^{(e)}(\omega)}{(\omega_0 + \omega) + i\Gamma} \tag{2.183}$$

since $\omega \approx \omega_0$, $\mu_-^{(e)}(\omega) \gg \mu_+^{(e)}(\omega)$. The results for the negative frequency terms are complex conjugates of the positive frequencies, so the results are very similar. We can neglect the terms that cause denominators that depend on $\omega_0 + \omega$. This is known as the rotating wave approximation (RWA) and can be incorporated into the electric dipole representation by writing it as

$$\mu^{(e)}(\omega) = \frac{1}{2}\left(-\mu_-^{(e)}(\omega)\sigma_+ e^{i\omega t} - \mu_-^{(e)*}(\omega)\sigma_- e^{-i\omega t}\right) + \frac{1}{2}\mu_0^{(e)}(\omega)\sigma_z\left(e^{i\omega t} + e^{-i\omega t}\right) \tag{2.184}$$

2.3.2 The Magnetic Interaction

Once the magnetic component of the optical field acts on a system placed in a superposition state by the electric field interaction, three frequencies of response emerge. This is due to the fact that the magnetic dipole operator contains two new frequencies. Thus, temporal evolution that describes the sequential action of ED and MD operators reflects three frequencies associated with the combined effects of $\mu^{(e)}$, $\mu^{(m)}$, namely 0, ω, and 2ω. The magnetic dipole operator has the irreducible tensor representation (see Appendix C for details):

$$\begin{aligned}\vec{\mu}^{(m)} = &-\frac{1}{2}\left(i\mu_{+}^{(m)}(2\omega)\hat{\varepsilon}_{-} - i\mu_{-}^{(m)}(2\omega)\hat{\varepsilon}_{+} - i\mu_{0}^{(m)}(2\omega)\hat{\varepsilon}_{0}\right)e^{2i\omega t} + h.c. \\ &+\left(-i\mu_{+}^{(m)}(0)\hat{\varepsilon}_{-} + i\mu_{-}^{(m)}(0)\hat{\varepsilon}_{+} + i\mu_{0}^{(m)}(0)\hat{\varepsilon}_{0}\right)\end{aligned} \tag{2.185}$$

The two-photon induced magnetic dipole therefore oscillates at frequencies 0 and 2ω, because it is assumed here to be driven by the field combination $E(\omega)B(\omega)$.

The magnetic interaction is calculated in a similar procedure to the electric interaction. First we find the magnetic dipole interaction Hamiltonian. It is given by

$$\begin{aligned}V^{(m)} &= -\vec{\mu}^{(m)}\cdot\vec{B} \\ &= -\frac{1}{2}\left[\left(i\mu_{+}^{(m)}\hat{\varepsilon}_{-} - i\mu_{-}^{(m)}\hat{\varepsilon}_{+} - i\mu_{0}^{(m)}\hat{\varepsilon}\right)e^{\omega t} + h.c.\right] \\ &\quad\cdot\left[\frac{i}{2}\left(B_{+}\hat{\varepsilon}_{-} - B_{-}\hat{\varepsilon}_{+}\right)e^{i\omega t} + h.c.\right] \\ &= -\frac{1}{4}\left[\mu_{+}^{(m)}(\omega)B_{-}e^{2i\omega t} + \mu_{+}^{(m)}(\omega)B_{+}^{*} + \mu_{-}^{(m)}(\omega)B_{+}e^{2i\omega t} + \mu_{-}^{(m)}(\omega)B_{-}^{*}\right. \\ &\quad\left.\mu_{+}^{(m)*}(\omega)B_{+} + \mu_{+}^{(m)*}(\omega)B_{-}^{*}e^{-2i\omega t} + \mu_{-}^{(m)*}(\omega)B_{-} + \mu_{-}^{(m)*}(\omega)B_{+}^{*}e^{-2i\omega t}\right]\end{aligned} \tag{2.186}$$

Making the secular approximation, this reduces to

$$V^{(m)} = \frac{1}{4}\left[\left(\mu_{+}^{(m)}(\omega)B_{-} + \mu_{-}^{(m)}(\omega)B_{+}\right) + h.c.\right] \tag{2.187}$$

For linear polarization, the transverse and longitudinal components of the magnetic dipole moment and field are related the same way as described for the electric components in the previous section, namely

$$\mu_{\pm}^{(m)} = \frac{\mu_0^{(m)}}{\sqrt{2}} \tag{2.188}$$

$$B_{\pm} = \frac{B_0}{\sqrt{2}} \tag{2.189}$$

So the interaction Hamiltonian becomes

$$\begin{aligned} V^{(m)} &= \frac{1}{4}\left[\left(\frac{\mu_0^{(m)}B_0}{2} + \frac{\mu_0^{(m)}B_0}{2}\right) + h.c.\right] \\ &= \frac{1}{2}\hbar\Omega_0^{(m)} \end{aligned} \tag{2.190}$$

In operator form this is

$$V^{(m)} = \frac{1}{2}\hbar\Omega_0^{(m)}\left(\frac{L_+}{\hbar} + \frac{L_-}{\hbar}\right) \tag{2.191}$$

Again, we need the commutators of the operators with the Hamiltonian for the Heisenberg equation of motion. To find the temporal evolution of $\mu^{(m)}$ we need $[H_0, \mu^{(m)}]$ and $[V^{(m)}, \mu^{(m)}]$. In view of Eq. (2.149), there are two relevant static Hamiltonians. The magnetic interaction can take place in either the excited state or the ground state. Hence, expanding the basis set to include all the states but focusing on the $L = 1$ excited state sub-space, we write

$$H_0 = \hbar\begin{pmatrix} \omega_0 + \omega_\phi & 0 & 0 \\ 0 & 0 & 0 \\ 0 & 0 & \omega_0 - \omega_\phi \end{pmatrix} = \hbar\omega_0\hat{I} + \hbar\omega_\phi\frac{\hat{L}_z}{\hbar} \tag{2.192}$$

This assumes that magnetic transitions take place with resonant frequency ω_ϕ between $L = 1$ sub-levels in the excited state. If we consider the magnetic transitions to be between $L = 1$ sub-levels of the admixture to the ground state the effective Hamiltonian is altered to

$$H_\phi = \hbar \begin{pmatrix} \omega_\phi & 0 & 0 \\ 0 & 0 & 0 \\ 0 & 0 & -\omega_\phi \end{pmatrix} = \hbar\omega_\phi \frac{\hat{L}_z}{\hbar} \tag{2.193}$$

since the zero of energy is chosen to be the ground eigenstate.

Focusing first on ground state dynamics at frequency 2ω, we calculate the commutators

$$\begin{aligned}
\left[H_\phi, \mu^{(m)}(2\omega)\right] &= \hbar\omega_\phi \frac{L_z}{\hbar}\left[\left(-\frac{i}{2}\mu_+^{(m)}(2\omega)\frac{L_-}{\hbar} + \frac{i}{2}\mu_-^{(m)}(2\omega)\frac{L_+}{\hbar} + \frac{i}{2}\mu_0^{(m)}(2\omega)\frac{L_z}{\hbar}\right)e^{2i\omega t} + h.c.\right] \\
&\quad - \left[\left(-\frac{i}{2}\mu_+^{(m)}(2\omega)\frac{L_-}{\hbar} + \frac{i}{2}\mu_-^{(m)}(2\omega)\frac{L_+}{\hbar} + \frac{i}{2}\mu_0^{(m)}(2\omega)\frac{L_z}{\hbar}\right)e^{2i\omega t} + h.c.\right]\hbar\omega_\phi\frac{L_z}{\hbar} \\
&= \frac{i}{2\hbar}\omega_\phi\left[\left(-\mu_+^{(m)}(2\omega)[L_z, L_-] + \mu_-^{(m)}(2\omega)[L_z, L_+]\right)e^{2i\omega t} + h.c.\right] \\
&= \frac{i}{2}\omega_\phi\left[\left(\mu_+^{(m)}(2\omega)L_- + \mu_-^{(m)}(2\omega)L_+\right)e^{2i\omega t} + h.c.\right] \qquad (2.194) \\
\left[V^{(m)}, \mu^{(m)}(2\omega)\right] &= \frac{1}{2}\hbar\Omega_0^{(m)}\left(\frac{L_+}{\hbar} + \frac{L_-}{\hbar}\right)\times \\
&\quad \left[\left(-\frac{i}{2}\mu_+^{(m)}(2\omega)\frac{L_-}{\hbar} + \frac{i}{2}\mu_-^{(m)}(2\omega)\frac{L_+}{\hbar} + \frac{i}{2}\mu_0^{(m)}(2\omega)\frac{L_z}{\hbar}\right)e^{2i\omega t} + h.c.\right] \\
&\quad - \left[\left(-\frac{i}{2}\mu_+^{(m)}(2\omega)\frac{L_-}{\hbar} + \frac{i}{2}\mu_-^{(m)}(2\omega)\frac{L_+}{\hbar} + \frac{i}{2}\mu_0^{(m)}(2\omega)\frac{L_z}{\hbar}\right)e^{2i\omega t} + h.c.\right]\times \\
&\quad \frac{1}{2}\hbar\Omega_0^{(m)}\left(\frac{L_+}{\hbar} + \frac{L_-}{\hbar}\right) \\
&= -\frac{i}{4}\hbar\Omega_0^{(m)}\left[\left(\mu_+^{(m)}(2\omega)\frac{[L_+, L_-]}{\hbar^2} + \mu_0^{(m)}(2\omega)\frac{[L_z, L_+]}{\hbar^2}\right.\right. \\
&\quad \left.\left. + \mu_-^{(m)}(2\omega)\frac{[L_+, L_-]}{\hbar^2} + \mu_0^{((m)}(2\omega)\frac{[L_z, L_-]}{\hbar^2}\right)e^{2i\omega t} + h.c.\right] \\
&= -\frac{i}{4}\hbar\Omega_0^{(m)}\left[\left(\mu_+^{(m)}(2\omega)\frac{L_z}{\hbar} + \mu_0^{(m)}(2\omega)\frac{L_+}{\hbar}\right.\right. \\
&\quad \left.\left. + \mu_-^{(m)}(2\omega)\frac{L_z}{\hbar} - \mu_0^{((m)}(2\omega)\frac{L_-}{\hbar}\right)e^{2i\omega t} + h.c.\right] \qquad (2.195)
\end{aligned}$$

With the results for $\mu^{(m)}$, $\left[H_\phi, \mu^{(m)}(2\omega)\right]$, and $\left[V^{(m)}, \mu^{(m)}(2\omega)\right]$ in hand, it is straightforward to solve the Heisenberg equation of motion for the time dependence of the magnetic dipole operator at frequency 2ω. This equation is

$$\frac{d\mu^{(m)}(2\omega)}{dt} = \frac{i}{\hbar}[H_\phi, \mu^{(m)}(2\omega)] + \frac{i}{\hbar}[V^{(m)}, \mu^{(m)}(2\omega)] - \Gamma\mu^{(m)}(2\omega) \tag{2.196}$$

and the solutions for amplitudes retained in the rotating wave approximation are

$$\mu_-^{(m)}(2\omega) = \frac{\Omega_0^{(m)}\mu_0^{(m)}(2\omega)}{2(\omega_\phi - 2\omega + i\Gamma)} \tag{2.197}$$

$$\mu_-^{(m)*}(2\omega) = \frac{\Omega_0^{(m)}\mu_0^{(m)}(2\omega)}{2(\omega_\phi - 2\omega - i\Gamma)} \tag{2.198}$$

Repeating this calculation for $\mu^{(m)}(0)$, one finds

$$\left[H_\phi, \mu_0^{(m)}\right] = i\hbar\omega_\phi \left[\mu_+^{(m)}(0)\frac{L_-}{\hbar} + \mu_-^{(m)}(0)\frac{L_+}{\hbar}\right] \tag{2.199}$$

$$\left[V^{(m)}, \mu^{(m)}(0)\right] = -i\hbar\Omega_0^{(m)} \left[2\mu_-^{(m)}(0)\frac{L_z}{\hbar} + \mu_0^{(m)}(0)\frac{L_+}{\hbar} - \mu_0^{(m)}(0)\frac{L_-}{\hbar}\right] \tag{2.200}$$

$$\mu_-^{(m)}(0) = \frac{\Omega_0^{(m)}\mu_0^{(m)}(0)}{2(\omega_\phi + i\Gamma)} \tag{2.201}$$

$$\mu_-^{(m)*}(0) = \frac{\Omega_0^{(m)}\mu_0^{(m)}(0)}{2(\omega_\phi - i\Gamma)} \tag{2.202}$$

The terms presented in Eqs. (2.201), (2.202), (2.197), and (2.198) are all consistent with the RWA and come from the *ground* state dynamics. The excited state dynamics only contribute terms that do not satisfy the rotating wave approximation and are reduced in magnitude by the optical frequency.

2.3.3 Heisenberg Polarization and Magnetization

To preserve normalization of the states when the electric and magnetic dipole operators act on the system, it is necessary to solve for the relative moments. Hence, the results for the commutators must be divided by the full amplitude of the relevant dipole with respect to the quantization axis.

The action of the normalized operators on the system is calculated next by writing down the product $\frac{\mu^{(m)}\mu^{(e)}}{\mu_0^{(m)}\mu_0^{(e)}}$ of amplitudes created by the ED and MD interactions and then calculating the matrix elements developed in the system by the second order interaction with

light, namely $<1|\mu^{(e)}(0)|3'>$, $<1|\mu^{(e)}(2\omega)|3'>$, and $<2'|\mu^{(m)}(\omega)|3'>$.

The action of the normalized electric dipole operator on the ground state $|nlm>=|100>$ is

$$\frac{\hat{\mu}^{(e)}(\omega)}{\mu_0^{(e)}(\omega)}|1> = \left[-\frac{1}{2}\frac{\mu_-^{(e)}}{\mu_0^{(e)}}\hat{\sigma}_+ e^{i\omega t} + h.c.\right]|100> \tag{2.203}$$

$$= -\left[\frac{1}{2}\frac{\Omega_0^{(e)}}{\omega_0-\omega+i\Gamma}e^{i\omega t} + \frac{1}{2}\frac{\Omega_0^{(e)*}}{\omega_0-\omega-i\Gamma}e^{-i\omega t}\right]|210> \tag{2.204}$$

where $\hat{\sigma}_+|1>=|210>$ for the excited state component and $\hat{\sigma}_+^\dagger|1>=|210>$ for the conjugate particle excitation.

The quantization axis of state $|2>$ is implicitly along the E field ($\hat{x}$ direction). The induced moment is therefore parallel to $\hat{x}$, not $\hat{z}$. Hence, the state $|210>$ needs to be transformed into the reference frame in which $\hat{z}$ is the axis of quantization. This is accomplished by a coordinate rotation in the $L=1$ sub-space. Consider a coordinate rotation by an angle $-\pi/2$ about the y axis. The new primed coordinates are related to the original ones by the mapping

$$\begin{pmatrix} x' \\ y' \\ z' \end{pmatrix} = \begin{pmatrix} 0 & 0 & 1 \\ 0 & 1 & 0 \\ -1 & 0 & 0 \end{pmatrix} \begin{pmatrix} x \\ y \\ z \end{pmatrix} \tag{2.205}$$

The components of a fixed vector experience the inverse rotation

$$\begin{pmatrix} V_x' \\ V_y' \\ V_z' \end{pmatrix} = \begin{pmatrix} 0 & 0 & -1 \\ 0 & 1 & 0 \\ 1 & 0 & 0 \end{pmatrix} \begin{pmatrix} V_x \\ V_y \\ V_z \end{pmatrix} \tag{2.206}$$

Recalling the expressions that relate the Cartesian and spherical components of an irreducible tensor of rank 1, namely

$$V_x = -\left(\frac{V_+ - V_-}{\sqrt{2}}\right) \tag{2.207}$$

$$V_y = i\left(\frac{V_+ + V_-}{\sqrt{2}}\right) \tag{2.208}$$

$$V_z = V_0 \tag{2.209}$$

one finds that

$$V_z' = -\left(\frac{V_+ - V_-}{\sqrt{2}}\right) \tag{2.210}$$

Hence, the state $|2>=|210>$ can be written in the spherical tensor basis as

$$|210>=Y_0 \rightarrow \frac{Y_1 - Y_{-1}}{\sqrt{2}} = \frac{|211> - |21-1>}{\sqrt{2}} \tag{2.211}$$

By the same token, the reference value of the electric dipole moment $\mu_0^{(e)}(\omega)$ is altered by the rotation. The full dipole moment becomes a transverse amplitude in the primed coordinates. Hence, the corresponding z component is

$$\mu_0^{(e)}(\omega) \rightarrow \sqrt{2}\mu_0^{(e)}(\omega) \equiv \mu_0^{(e)'} \tag{2.212}$$

This shows that the electric dipole interaction creates the superposition state $|2'>$:

$$\frac{\hat{\mu}^{(e)}(\omega)}{\mu_0^{(e)'}(\omega)}|1>= -\left[\frac{1}{2}\frac{\Omega_0^{(e)}}{\omega_0 - \omega + i\Gamma}e^{i\omega t} + \frac{1}{2}\frac{\Omega_0^{(e)*}}{\omega_0 - \omega - i\Gamma}e^{-i\omega t}\right](|211> - |21-1>) \equiv |2'> \tag{2.213}$$

The magnetic field is now able to act on the state $|2'>$ to generate the final superposition state $|3'>$ in the following way:

$$\frac{\mu^{(m)}}{\mu_0^{(m)}}(|211>-|21-1>) = \left[\frac{i}{2}\frac{\mu_-^{(m)}(2\omega)}{\mu_0^{(m)}(2\omega)}\frac{L_+}{\hbar}e^{2i\omega t} - \frac{i}{2}\frac{\mu_+^{(m)}(2\omega)}{\mu_0^{(m)}(2\omega)}\frac{L_-}{\hbar}e^{2i\omega t}\right.$$
$$-\frac{i}{2}\frac{\mu_-^{(m)*}(2\omega)}{\mu_0^{(m)}(2\omega)}\frac{L_-}{\hbar}e^{-2i\omega t} + \frac{i}{2}\frac{\mu_+^{(m)*}(2\omega)}{\mu_0^{(m)}(2\omega)}\frac{L_+}{\hbar}e^{-2i\omega t}$$
$$\left.+i\frac{\mu_-^{(m)}(0)}{\mu_0^{(m)}(0)}\frac{L_+}{\hbar} - i\frac{\mu_+^{(m)}(0)}{\mu_0^{(m)}(0)}\frac{L_-}{\hbar}\right](|211>-|21-1>)$$
$$= -i\left[\frac{1}{2}\frac{\mu_-^{(m)}(2\omega)}{\mu_0^{(m)}(2\omega)}e^{2i\omega t} + c.c. + \frac{1}{2}\frac{\mu_+^{(m)}(2\omega)}{\mu_0^{(m)}(2\omega)}e^{2i\omega t} + c.c.\right.$$
$$\left.+\frac{\mu_-^{(m)}(0)}{\mu_0^{(m)}(0)} + \frac{\mu_+^{(m)}(0)}{\mu_0^{(m)}(0)}\right]|210> \qquad (2.214)$$

The result of the two sequential electric and magnetic dipole interactions is the evolution of the system from state $|1>$ to state $|3'>$, where

$$|3'> = \frac{\mu^{(m)}}{\mu_0^{(m)}}\frac{\mu^{(e)}}{\mu_0^{(e)}}|1>$$
$$= i\left[\frac{1}{4}\frac{\mu_-^{(m)}(2\omega)}{\mu_0^{(m)}(2\omega)}\frac{\mu_-^{(e)}(\omega)}{\mu_0^{(e)}(\omega)}e^{3i\omega t} + \frac{1}{4}\frac{\mu_+^{(m)}(2\omega)}{\mu_0^{(m)}(2\omega)}\frac{\mu_-^{(e)}(\omega)}{\mu_0^{(e)}(\omega)}e^{-i\omega t}\right.$$
$$+\frac{1}{4}\frac{\mu_-^{(m)}(2\omega)}{\mu_0^{(m)}(2\omega)}\frac{\mu_-^{(e)*}(\omega)}{\mu_0^{(e)}(\omega)}e^{i\omega t} + \frac{1}{4}\frac{\mu_+^{(m)}(2\omega)}{\mu_0^{(m)}(2\omega)}\frac{\mu_-^{(e)*}(\omega)}{\mu_0^{(e)}(\omega)}e^{-3i\omega t}$$
$$+\frac{1}{4}\frac{\mu_-^{(m)*}(2\omega)}{\mu_0^{(m)}(2\omega)}\frac{\mu_-^{(e)}(\omega)}{\mu_0^{(e)}(\omega)}e^{-i\omega t} + \frac{1}{4}\frac{\mu_+^{(m)*}(2\omega)}{\mu_0^{(m)}(2\omega)}\frac{\mu_-^{(e)}(\omega)}{\mu_0^{(e)}(\omega)}e^{3i\omega t}$$
$$+\frac{1}{4}\frac{\mu_-^{(m)*}(2\omega)}{\mu_0^{(m)}(2\omega)}\frac{\mu_-^{(e)*}(\omega)}{\mu_0^{(e)}(\omega)}e^{-3i\omega t} + \frac{1}{4}\frac{\mu_+^{(m)*}(2\omega)}{\mu_0^{(m)}(2\omega)}\frac{\mu_-^{(e)*}(\omega)}{\mu_0^{(e)}(\omega)}e^{i\omega t}$$
$$+\frac{1}{2}\frac{\mu_-^{(m)}(0)}{\mu_0^{(m)}(0)}\frac{\mu_-^{(e)}(\omega)}{\mu_0^{(e)}(\omega)}e^{i\omega t} + \frac{1}{4}\frac{\mu_+^{(m)}(0)}{\mu_0^{(m)}(0)}\frac{\mu_-^{(e)}(\omega)}{\mu_0^{(e)}(\omega)}e^{i\omega t}$$
$$\left.+\frac{1}{2}\frac{\mu_+^{(m)}(0)}{\mu_0^{(m)}(0)}\frac{\mu_-^{(e)*}(\omega)}{\mu_0^{(e)}(\omega)}e^{-i\omega t} + \frac{1}{2}\frac{\mu_-^{(m)}(0)}{\mu_0^{(m)}(0)}\frac{\mu_-^{(e)*}(\omega)}{\mu_0^{(e)}(\omega)}e^{-i\omega t}\right]|210> \qquad (2.215)$$

Now we proceed to calculate $<1|\mu_0^{(e)}(0)|3'>$, $<1|\mu^{(e)}(2\omega)|3'>$, and $<2'|\mu^{(m)}(\omega)|3'>$. The RWA is assumed for both the electric and magnetic interactions. To ensure no net

angular momentum is excited (linearly polarized light) in the system, the $L_\pm$ operators are combined only with $L_\mp$ terms. Hence, the radiative MD moment has matrix element

$$
\begin{aligned}
< 2'|\mu^{(m)}(\omega)|3' > = -\mu_{32}^{(m)} \Bigg[& \frac{1}{8}\frac{\Omega_0^{(m)}/2}{\omega_\phi - 2\omega + i\Gamma}\frac{\Omega_0^{(e)}/2}{\omega_0 - \omega + i\Gamma}e^{i\omega t} + \frac{1}{8}\frac{\Omega_0^{(m)}/2}{\omega_\phi - 2\omega + i\Gamma}\frac{\Omega_0^{(e)*}/2}{\omega_0 - \omega - i\Gamma}e^{-i\omega t} \\
& + \frac{1}{8}\frac{\Omega_0^{(m)*}/2}{\omega_\phi - 2\omega - i\Gamma}\frac{\Omega_0^{(e)}/2}{\omega_0 - \omega + i\Gamma}e^{i\omega t} + \frac{1}{8}\frac{\Omega_0^{(m)*}/2}{\omega_\phi - 2\omega - i\Gamma}\frac{\Omega_0^{(e)*}/2}{\omega_0 - \omega - i\Gamma}e^{i\omega t} \\
& + \frac{1}{4}\frac{\Omega_0^{(m)}/2}{\omega_\phi + i\Gamma}\frac{\Omega_0^{(e)}/2}{\omega_0 - \omega + i\Gamma}e^{-i\omega t} + \frac{1}{4}\frac{\Omega_0^{(m)*}/2}{\omega_\phi - i\Gamma}\frac{\Omega_0^{(e)*}/2}{\omega_0 - \omega - i\Gamma}e^{i\omega t} \Bigg]
\end{aligned}
\tag{2.216}
$$

where $\mu_{32}^{(m)} \equiv < 21 \pm 1|eL_\pm/2m|210 >$. Simplifying and assuming $\Omega_0^{(m)} = \Omega_0^{(m)*}$ we find

$$
\begin{aligned}
< 2'|\mu^{(m)}(\omega)|3' > = \frac{1}{16}\mu_{32}^{(m)} \Bigg[& \frac{\Omega_0^{(e)}}{\omega_0 - \omega + i\Gamma^{(e)}}e^{i\omega t}\frac{\Omega_0^{(m)}(\omega_\phi - 2\omega)}{(\omega_\phi - 2\omega)^2 + \Gamma^{(m)2}}e^{i\omega t} + c.c. \\
& + \frac{\Omega_0^{(e)}}{\omega_0 - \omega + i\Gamma^{(e)}}\frac{\Omega_0^{(m)}}{\omega_\phi + i\Gamma^{(m)}}e^{-i\omega t} + c.c. \Bigg]
\end{aligned}
\tag{2.217}
$$

Similarly, the two electric moments are

$$
\begin{aligned}
< 1|\mu^{(e)}|3' > = -\frac{i}{16}\mu_{12}^{(e)} \Bigg[& \frac{\Omega_0^{(m)}}{\omega_\phi - 2\omega + i\Gamma^{(m)}}\frac{\Omega_0^{(e)}(\omega_0 - \omega)}{(\omega_0 - \omega)^2 + \Gamma^{(e)2}}e^{2i\omega t} + c.c. \\
& + \frac{\Omega_0^{(e)}}{\omega_0 - \omega + i\Gamma^{(e)}}\frac{\Omega_0^{(m)}}{\omega_\phi + i\Gamma} + c.c. \Bigg]
\end{aligned}
\tag{2.218}
$$

where $\mu_{12}^{(e)} \equiv < 100|er|210 >$. The final expressions for polarization and magnetization, which are the main results of this section, are therefore:

$$
\begin{aligned}
P(0) &= N < 1|\mu^{(e)}(0)|3' > \hat{z} \\
&= -N\frac{i}{16}\mu_{12}^{(e)}\left[\frac{\Omega_0^{(e)}}{\omega_0-\omega+i\Gamma^{(e)}}\frac{\Omega_0^{(m)}}{\omega_\phi+i\Gamma}+c.c.\right]\hat{z} \qquad (2.219)\\
P(2\omega) &= N < 1|\mu^{(e)}(2\omega)|3' > \hat{z} \\
&= -N\frac{i}{16}\mu_{12}^{(e)}\left[\frac{\Omega_0^{(m)}}{\omega_\phi-2\omega+i\Gamma^{(m)}}\frac{\Omega_0^{(e)}(\omega_0-\omega)}{(\omega_0-\omega)^2+\Gamma^{(e)2}}e^{2i\omega t}+c.c.\right]\hat{z} \qquad (2.220)\\
M(\omega) &= -N < 2'|\mu^{(m)}(\omega)|3' > \hat{y} \\
&= -N\frac{1}{16}\mu_{32}^{(m)}\left[\frac{\Omega_0^{(e)}}{\omega_0-\omega+i\Gamma^{(e)}}e^{i\omega t}\frac{\Omega_0^{(m)}(\omega_\phi-2\omega)}{(\omega_\phi-2\omega)^2+\Gamma^{(m)2}}e^{i\omega t}+c.c.\right. \\
&\quad \left.+\frac{\Omega_0^{(e)}}{\omega_0-\omega+i\Gamma^{(e)}}\frac{\Omega_0^{(m)}}{\omega_\phi+i\Gamma^{(m)}}e^{-i\omega t}+c.c.\right]\hat{y} \qquad (2.221)
\end{aligned}
$$

When the difference in representations is taken into account for dipole moments in this calculation, the result agrees quantitatively with the results of the last section and Ref. [22] (as amended), obtained using the density matrix.

Chapter 3

Methods

In this chapter the experimental methods and apparatus for the observation of magnetic dipole scattering are discussed. This includes the calibration and statistics of the photomultiplier detector, design of the collection optics system, sample preparation, and data collection algorithms.

3.1 Magnetic Dipole Scattering

The experimental approach used in this work was based on elastic light scattering, for which the radiation patterns are well known [11]. In the case of dipole radiation, the maximum amount of energy is emitted in a direction perpendicular to the axis of the dipole and none is emitted parallel to the dipole axis, regardless of whether the dipole is electric or magnetic.

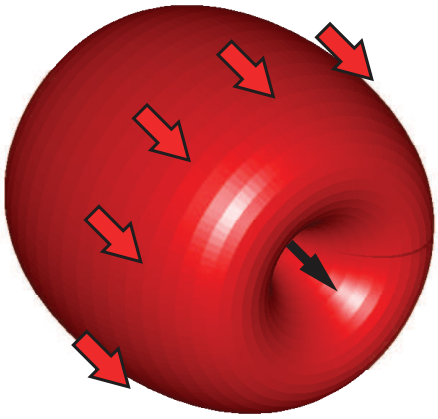

Figure 3.1 Electric dipole radiation pattern given a linear charge motion directed through the center of the dipole pattern. The polarization of the radiation is parallel to both the charge motion and the electric dipole moment.

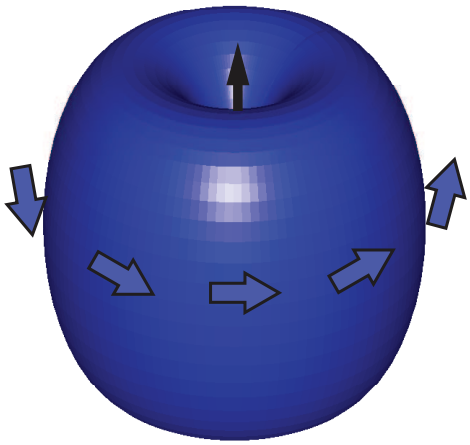

Figure 3.2 Magnetic dipole radiation pattern given a solenoidal charge motion orbiting the center of the dipole pattern. The (electric field) polarization of the radiation is perpendicular to the magnetic dipole moment.

The result of a full calculation (see Sec. 1.4) yields the classic $\sin^2\theta$ radiation pattern displayed in Fig. 3.1. The polarization of the light emitted depends on the type of dipole as discussed in Chapter 1. The goal of the experimental portions of this dissertation research was to separate the electric and magnetic dipole contributions in scattered light in order to study the radiation pattern, polarization, and intensity dependence of the magnetic dipole in several different samples. Since the radiation patterns of electric and magnetic dipoles are orthogonal for elastic scattering at the unique angle of $\theta_{sc} = 90°$, all experiments described here were performed at this angle.

When linearly polarized light is passed through a dielectric sample, the first motion of the electrons is an oscillation parallel to the direction of polarization. This oscillating, linear dipole radiates in a $\sin^2\theta$ pattern where θ is measured from the direction of the electric field. The polarization of this radiation is parallel to the electric field of the light (Figure 3.1). Second, the magnetic field, which is perpendicular to the direction of polarization, causes the electron motion to oscillate in a curve around the magnetic field. This circular motion is an induced magnetic dipole that also radiates in a $\sin^2\theta$ pattern where θ is now measured from the direction of the magnetic field. The polarization of this radiation is perpendicular

to the magnetic field of the light (Figure 3.2). However the incident electric and magnetic fields are also perpendicular. Hence, the radiation patterns are indistinguishable in the forward direction where both dipoles are transverse to the propagation axis of scattered light. When $\theta_{sc} = 90^{\circ}$, the polarization of incident light maybe rotated to control whether a given induced dipole is transverse or longitudinal and the radiation patterns may be observed separately (Fig. 3.3).

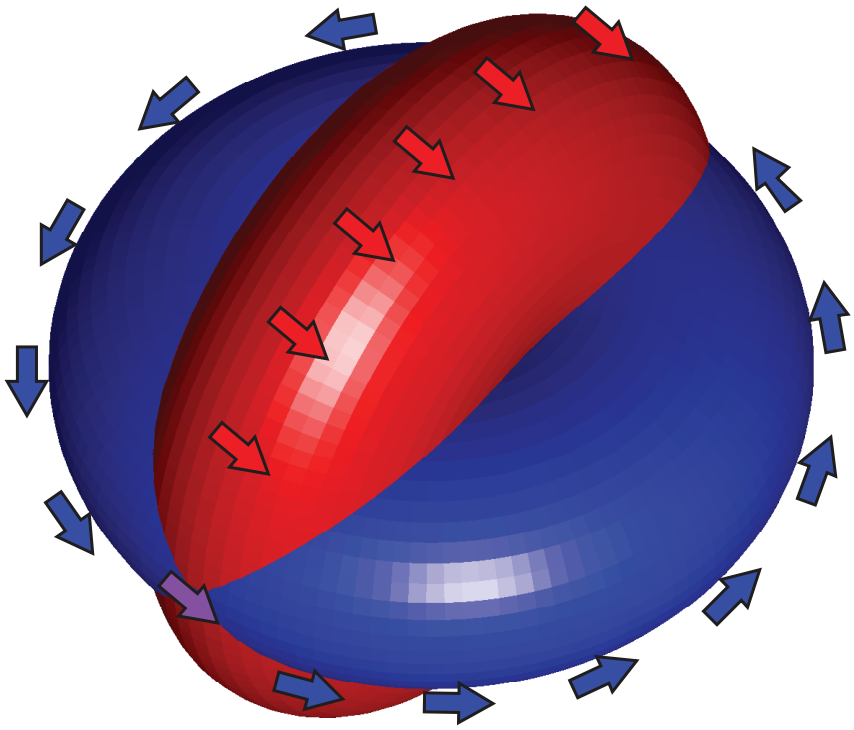

Figure 3.3 Radiation and polarization from electric (Red) and magnetic (Blue) dipoles generated by a plane wave of light. The purple arrow indicates that the polarizations of the two polarizations are parallel, and therefore indistinguishable, along the forward direction

Experimentally, the finite volume of emission and the finite area of detection introduce a small solid angle in collection. In spherical coordinates defined in Fig. 3.4, we can calculate the error in our signal due to collecting a small solid angle of light rather than $\theta_{sc} = 90^{\circ}$ scattered light alone.

From Chapter 1 it may be recalled that the polarization of an electric dipole is along the $\hat{\theta}$ direction and the polarization of a magnetic dipole is along the $\hat{\phi}$. Assuming that the detector is along the $\hat{x}$ of Fig. 3.4 and collects a small angle in both $\hat{\theta}$ and $\hat{\phi}$ we can find the projection of the polarization direction onto the detector.

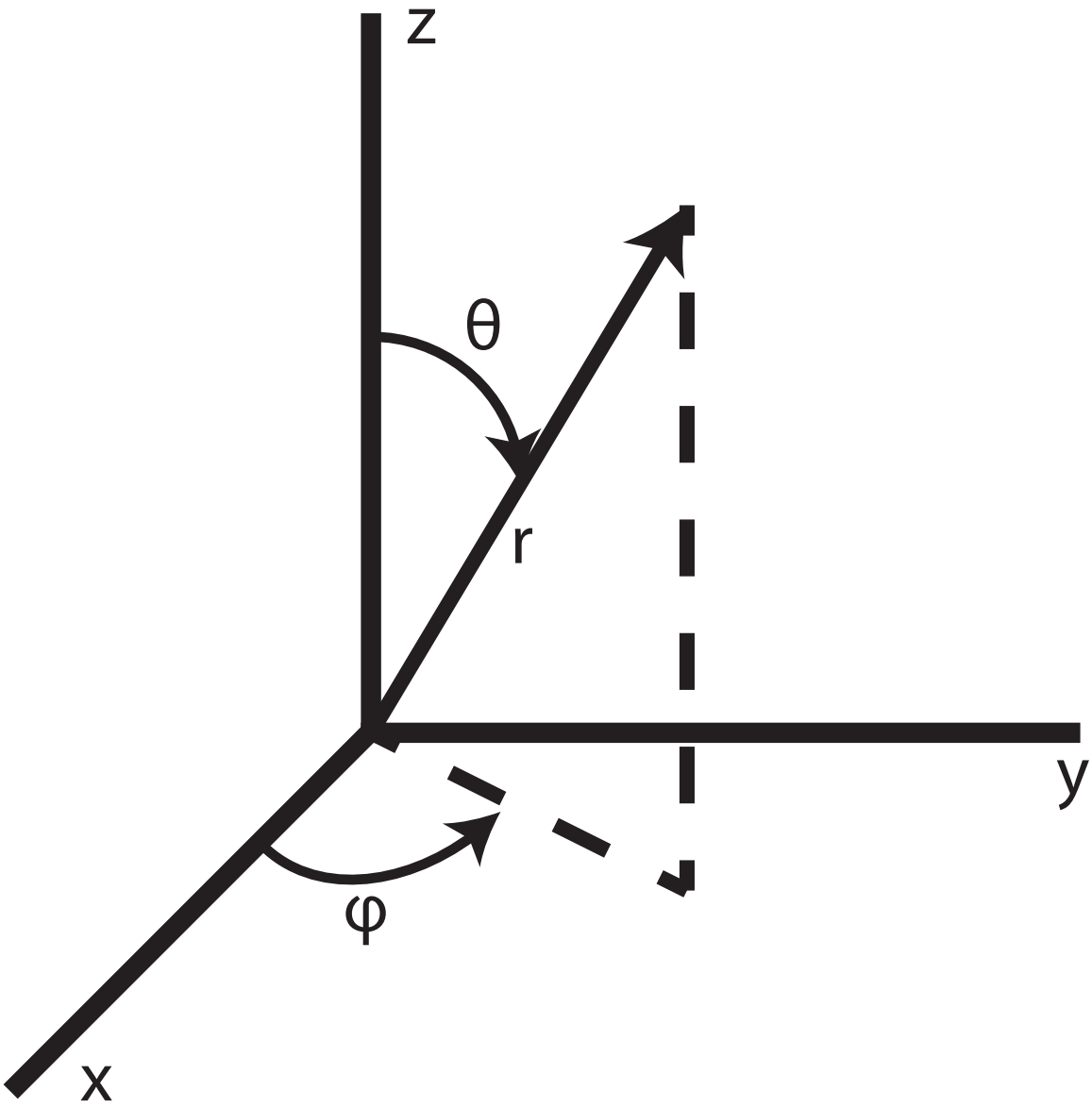

Figure 3.4 Spherical coordinate system following standard physics/mathematics conventions

A transverse electric dipole scatterer located at the origin is oriented parallel to the $\hat{\theta}$ vector which decomposes as

$$\hat{\theta} = \cos(\theta)\cos(\phi)\hat{x} + \cos(\theta)\sin(\phi)\hat{y} - \sin(\theta)\hat{z} \tag{3.1}$$

For a small angle around the $\hat{x}$ axis, $\theta \simeq \pi/2$ and $\phi \simeq 0$. This allows the simplification of the projection to

$$\hat{\theta} \simeq \theta\hat{x} + \theta\phi\hat{y} - \hat{z} \tag{3.2}$$

When projecting onto the yz plane, the $\hat{x}$ direction is normal to the detector and therefore can be ignored, resulting in

$$\hat{\theta} \simeq \theta\phi\hat{y} - \hat{z} \tag{3.3}$$

$$\Delta\hat{\theta} \simeq \Delta\theta\Delta\phi\hat{y} \tag{3.4}$$

This shows that for small angles in θ (about $\pi/2$) and ϕ, setting an analyzing polarizer to the vertical direction, $\hat{z}$, ontroduces errors in second order, proportional to $\Delta\theta\Delta\phi$. Only a very small amount of signal from an electric dipole is lost by passing through a polarizer.

A transverse magnetic dipole scatterer located at the origin is parallel to the $\hat{\phi}$ vector which decomposes as

$$\hat{\phi} = -\sin(\phi)\hat{x} + \cos(\phi)\hat{y} \tag{3.5}$$

For a small angle this simplifies to

$$\hat{\phi} \simeq -\phi\hat{x} + \hat{y} \tag{3.6}$$

$$\Delta\hat{\phi} \simeq -\Delta\phi\hat{x} \tag{3.7}$$

As before, the $\hat{x}$ direction is normal to the detector and therefore can be ignored, resulting in

$$\hat{\phi} \simeq \hat{y} \tag{3.8}$$

$$\Delta\hat{\phi} \simeq 0 \tag{3.9}$$

Interestingly, there is no error in measuring the magnetic dipole signal through a horizontally, $\hat{y}$, oriented polarizer. This means that to second order there is no signal leaking from electric dipole scattering into the magnetic dipole measurement.

3.1.1 Construction and Alignment

In order to measure the two scattered signals we implement a perpendicular scattering geometry. A linearly polarized beam is first passed through a precision 90° prism in order to define the sample location as well as a precisely perpendicular direction along which we will place the detection optics. The two beam paths are defined by pairs of irises.

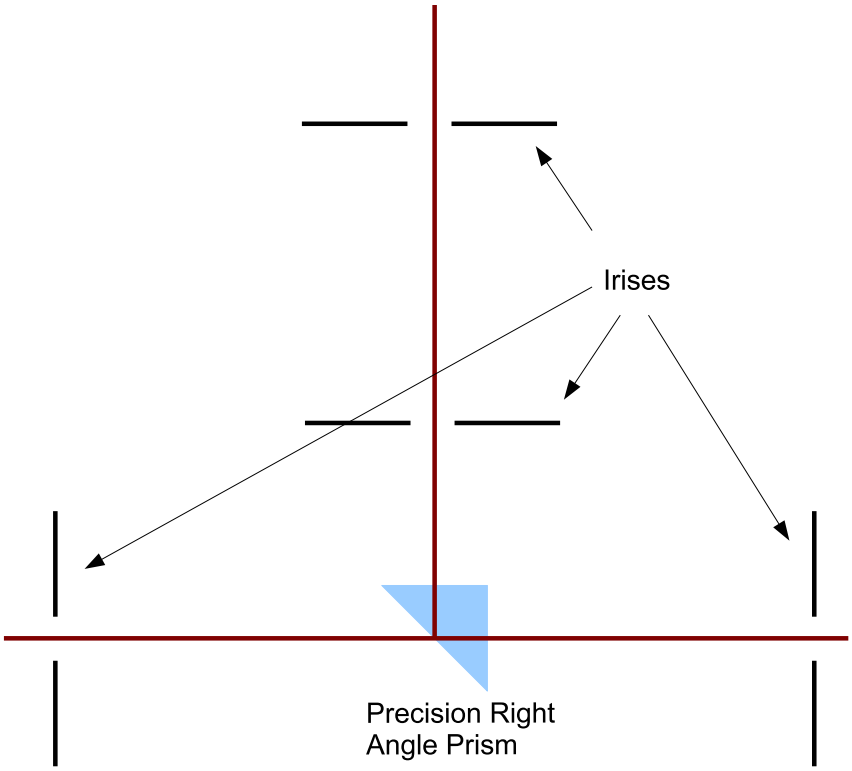

Figure 3.5

A second, low-power, alignment laser is then passed through the pair of irises defining the detection arm so that in the future the system can be aligned without using the more intense pump laser. The precision right angle prism is then removed but its mount is left to serve as a sample holder. the intersection of the pump beam and alignment beam is centered on any sample placed on the holder.

The intensity of the pump beam is controlled by a variable neutral density filter. The polarization, while initially 100:1 out of the laser, is improved to 10000:1 by passing the beam through a Glan-Laser polarizer. The direction of polarization is then controlled by a half-wave plate mounted in a motorized rotary stage. In the detection arm, a 10000:1 Glan-Laser polarizer is mounted in a motorized rotary stage just behind the final iris in order

to allow only the selected polarization to pass into a detector. The face of this polarizer is set normal to the detection arm axis by retroreflection of the alingment laser. After passing over the sample holder the pump beam enters a beam dump with the option of being replaced by a photodetector to enable real-time power measurement and compensation.

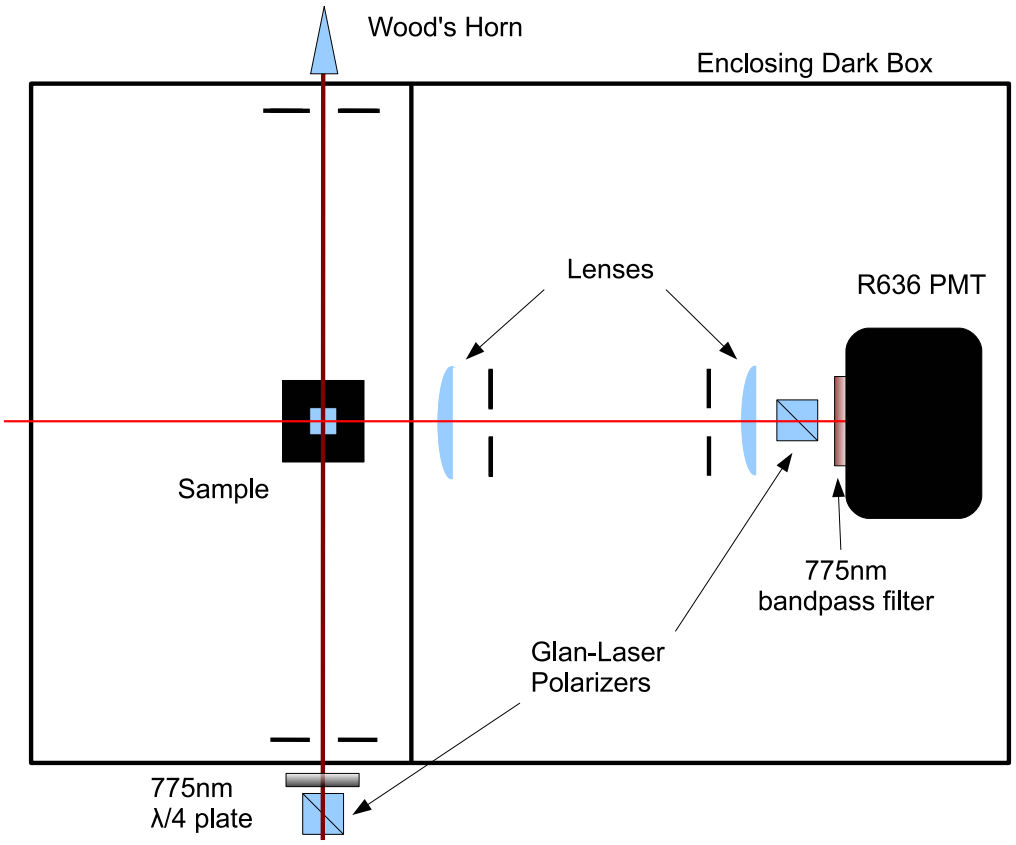

Figure 3.6 Experimental setup for photon counting in a perpendicular scattering geometry

With the location, intensity, and polarization of the pump beam controlled, we now focus on collecting the signal. As the pump beam passes through a dielectric material, the electrons are induced to move in phase with the light and each other. Only in the forward direction are the motions seen to be in phase and therefore form a beam of light that continues through the medium. In the perpendicular direction, since the oscillations are seen to be out of phase, only a tiny signal propagates. This signal is still at the fundamental frequency of the pump beam. In order to detect this small signal we place behind the analyzing polarizer a 10nm FWHM bandpass intereference filter centered on the pump laser wavelength. This reduces the possibility of detecting photons other than those from the sample by at least four orders

of magnitude compared to the signal. To reduce the possibility even further, a dark box is constructed around the entire apparatus with only three holes punched in the exterior walls. Two holes allow for the entrance and exit of the pump beam. A third hole (on the left of Fig. 3.6) allows the alignment laser to pass into the box toward the detector. This hole can be blocked by a shutter during data collection. A dividing wall is constructed inside the dark box separating the apparatus into two halves, one containing the sample, sample holder, and the three entrance and exit holes, the other containing the detection arm. A small hole through the dividing wall allows the alignment laser, and also the signal, to pass from one half of the box into the other. This setup eliminates the possibility of any stray light entering the detection arm. To collect the signal light a two lens imaging telescope is constructed in the detection arm. The first lens is placed between the sample/dividing wall and the first iris of the detection arm. The second is placed between the second iris and analyzing polarizer. The imaging conditions of the telescope can be adjusted to change the magnification of the image on the detector. The total signal onto the detector can be adjusted by changing the size of the irises within the collimated beam portion of the imaging telescope.

3.1.2 Detection and Data Collection

For photon counting experiments the detector is a Hamamatsu R636 side-on photomultiplier tube. It is housed in a Products for Research sealed, air cooled photomultiplier housing with a shutter. It is wired for low noise with the anode held at ground and the high bias voltage applied over the cathodes by a Stanford Research PS325 High Voltage Power Supply. To reduce the noise, before any data collection, the photomultiplier was left under high voltage in the dark for an extended period of time. To improve the efficiency and average out any inhomogeneity of the photocathode, the image of the sample formed by the imaging telescope was magnified to fill a significant fraction of the photocathode without extending beyond the boundaries. Once the photomultiplier is powered, the signal is viewed on an oscilloscope to see if clean, well-separated, and repeatable pulses are generated. If the pulses reach a peak height below $10mV$ (the minimum recommended discriminator height of the SR400 discussed below) a Stanford Research SR445 Preamplifier is available to provide amplification of up to 625 times before data collection.

The pulse height and noise of the photomultiplier are primarily determined by the voltage applied across the cathodes. The pulse height and gain of the R636 photomultiplier is nearly linear over the range 500-1500V. However, with increased voltage also comes increased dark current. The total current drawn through the photomultiplier as a function of applied voltage was explored. It was found that for higher intensity experiments 1250V provided

sufficient gain and low noise. For experiments at low intensity requiring more gain, 1400V was found to provide sufficient gain while not increasing the dark counts to unreasonable levels.

Data collection was performed using a Stanford Research SR400 photoncounter. The main function of the SR400 is to use an electronic discriminator to count the number of pulses, during a window of time, that reach a peak voltage greater than the set voltage of the discriminator. There are three discriminators, each of which can count pulses separated by a minimum of $5ns$ or a pulse rate of approximately 200 million counts per second. The intensity of scattered light is never expected to approach this count rate, so it is assumed that every pulse is counted. No two-photon peaks are observed in Fig. 3.8 confirming that the pulses are well separated. The simplest form of data collection, used for long integration times, is CW or having the disscriminators constantly counting. By counting the number of pulses in a fixed time while the pump beam is on but the sample cuvette is empty we find the background count rate of the setup. Then the cuvette is replaced with an identical cuvette filled with the sample liquid and pulses are counted for the same duration. Subracting the first result from the second provides background correction to the measurement.

The SR400 also has two independent gates that can trigger the discriminators. These gates can be triggered to open for a fixed amount of time after a delay. The gate width is accurate to less than $1ms$ and the delay can be as short as $25ns$. Between each measurement the SR400 must dwell for a fixed amount of time, as short as $.2ms$. Combining the discriminators with the gates, there are many possible count modes. We made use of the A-B mode to provide real-time background subtraction during data collection. In this mode the SR400 counts the number of pulses that reach the discriminator height of both the A discriminator and the B discriminator and then records the difference. Using the timing diagram of Fig. 3.7 the number of pulses of height H measured while the pump beam was off was subracted from the number of pulses measured while the pump beam was on.

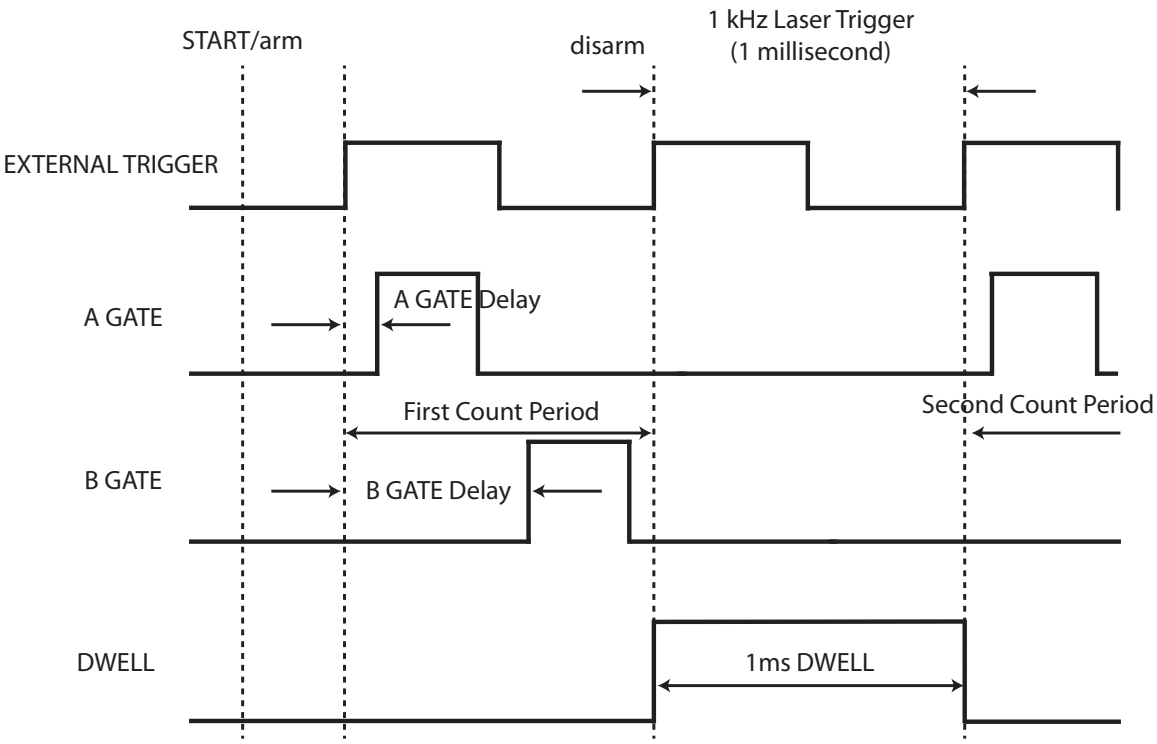

Figure 3.7 Timing diagram of real-time background subtraction using multiple gates on SR400 photoncounter

This provides a background subtraction for any light reaching the detector due to sources other than scattering from the sample. Given the 1kHz repetition rate of the pump beam this means that background subtraction was performed every millisecond, a very short time compared to most fluctuations in light levels in the room. Thus, any light leakage through the enclosing box, telescope apertures, and interference filter is still subtracted from the the measured signal.

A differential pulse height analysis was performed to find the ideal pulse discriminator voltage to collect all counts due to single photon events but a minimum of dark count events or noise. In this procedure, the discriminator threshold is scanned from nearly $0mV$ to well beyond the highest expected peak height. At each discriminator step, the SR400 is allowed to count pulses for a fixed amount of time. Then the number of counts at discriminator height N is subtracted from the number of counts at discriminator height N-1. This results in a binned data set where the number of pulses between pulse heights N and N-1 is plotted versus pulse height as seen in Fig. 3.8.

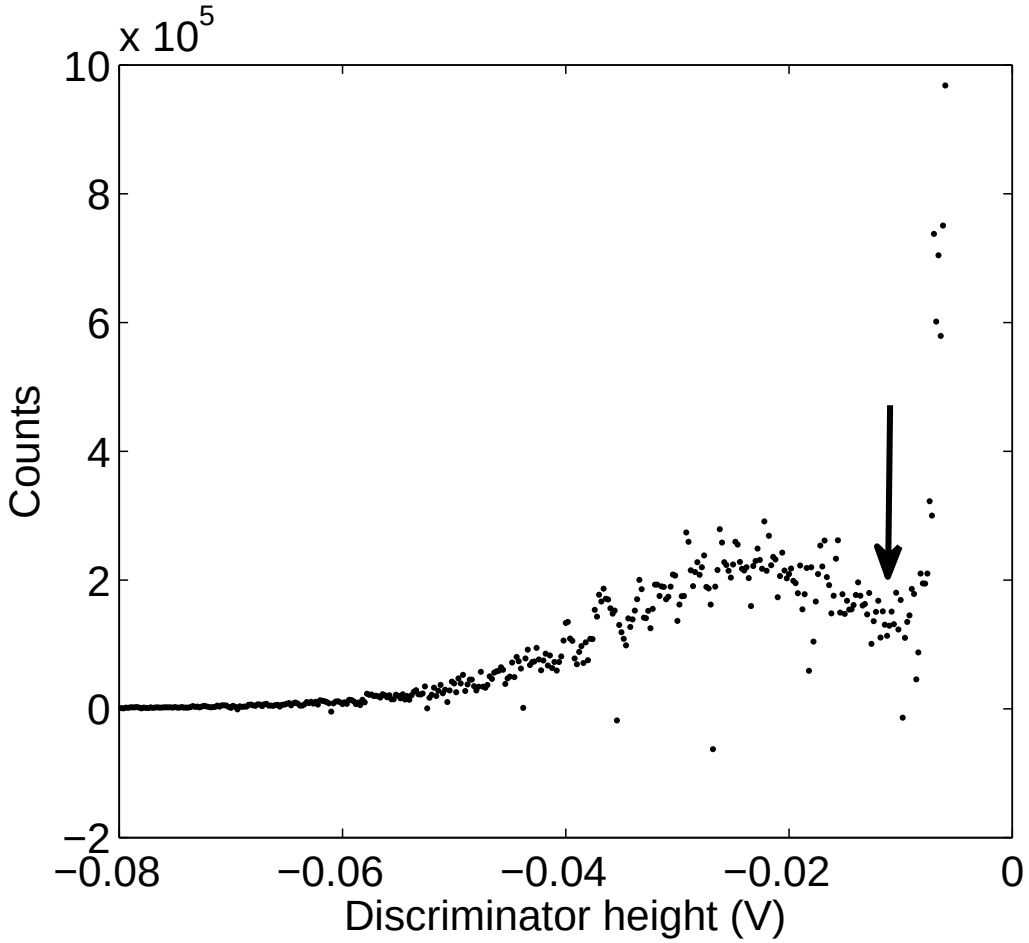

Figure 3.8 Differential pulse height spectrum of output from Hamamatsu R636 photomultiplier tube. The arrow indicates the discriminator voltage setting that should be chosen to count all photon events but as few dark counts as possible.

This data is used to choose the best discriminator voltage setting for data collection. By setting the discriminator voltage at the local minimum indicated in the diagram only pulses of height greater than (to the left of) this set point will be counted. This excludes a significant number of dark counts as seen in Fig. 3.8 as the discriminator voltage approaches $0mV$.

With the photomultiplier and discriminator voltages chosen we can now collect data. First, the input intensity is set using a variable neutral density filter outside the data collection box. In order to measure the intensity dependence of the magnetic dipole scattering, the intensity is first set quite low, approximately $10^7 W/cm^2$. With the intensity fixed we set the analyzing polarizer in front of the photomultiplier to the vertical direction. The polarizer is mounted in a Newport PR50PP rotation stage that is powered by a Newport SMC100PP and controlled by LabView drivers. This will allow vertically polarized light from an electric dipole to be detected. The quarter-wave plate in the pump beam is also mounted in a

Newport PR50PP powered by a Newport SMC100PP and controlled by the same LabView program. In the course of data collection the angle of the quarter-wave plate is varied in steps while vertically polarized signal is measured at each step by the photomultiplier. The minimum step size is .02 degrees but larger step sizes are typically chosen for speed of collection and clarity of plots. After a complete 360 degree sweep of the quarter-wave plate is recorded the analyzing polarizer is rotated 90 degrees into the horizontal position and the sweep of the quarter-wave plate is repeated. This will generate both an electric dipole and magnetic dipole measurement for analysis. By automating the experiment the laboratory can be placed in full darkness and no experimenter is required to be in the room to add possible signal from reflection of ambient light or additional infrared generated by body heat. It also allows extremely long integration times for low signal collection and very precise and repeatable angular postioning of the quarter-wave plate and analyzing polarizer.

3.1.3 Sample Selection

Samples that were available in extremely pure form and that had well known optical properties were selected for the experiments. Three spectoscopic grade liquids that lacked resonances anywhere near the excitation wavelengths of 775nm and 810nm were deemed the most appropriate in this regard, while being dense enough to cause a measureable number of scattering events into the perpendicular direction. The use of gases was excluded because of the low scattering rate. Liquids were also chosen because they lack impurities or flaws that could give rise to multiple scattering. Nor do they have long range structure to cause any changes to the polarization or intensity of the light due to interaction with a non-isotropic medium. Ideal samples should have a third order susceptibility, $\chi^{(3)}$, that is low enough to allow experiments to be performed at significant pump intensites ($10^{10} W/cm^2$) without the possibility of third order nonlinear processes changing the measured signal. Finally, and most importantly, the control sample must be centrosymmetric to exclude all second order nonlinear optical processes other than the optical magnetic process of interest.

Our control sample was chosen to be spectroscopic grade carbon tetrachloride. Carbon tetrachloride is a very well studied chemical reagent that is optically clear and can be purchased in a highly purified liquid form. The density of liquid provides the necessary scattering but the amorphous structure provides no long range order. It also has a low third order susceptibility [25], as seen in Table 3.1, and is effectively centrosymmetric, so its second order (electric) susceptibility is zero.

To test the dependence of magnetic scattering on electronic structure it is necessary to select other liquids that are optically clear and highly pure but with dramatically different

Material	$\chi^{(3)}(esu)$	$n_2(cm^2W^{-1})$
Benzene	6.8×10^{-14}	1.2×10^{-15}
Carbon tetrachloride	8.0×10^{-14}	1.5×10^{-15}
Water	1.8×10^{-14}	4.1×10^{-16}

Table 3.1 Third order nonlinear optical coefficients for sample reagents

structure. Benzene, another organic solvent, is readily available in spectroscopic grade purity and has a ring structure that allows some of the electron cloud to be nearly free. Water provides a polar liquid that is also readily available as highly purified, deionized water. Consequently CCl_4, H_2O, and C_6H_6 were picked as samples for the investigation. Their nonlinear properties are summarized in Table 3.1.

3.1.4 Sample Preparation

Samples for the magnetic dipole scattering experiment were highly purified, spectroscopic grade reagents. The liquids were passed through two $0.2\mu m$ Millipore filters to remove any possible particle contaminants and deposted in Hellma QS 1cm x 1cm quartz spectrophotonic cells. Cells were washed on the inside using high concentration detergent using the procedurer recommended by the manufacturer. A drop of detergent was placed in the cell and mixed with distilled water to approximately 75% full. The cell was capped and shaken vigorously for approximately 30 seconds. The cells were emptied and filled with distilled water and shaken. This rinsing step was reapeated about six times to guarantee that all detergent was removed. The outer faces of the cell were cleaned with methanol and a dragged lens tissue, a standard optics procedure. The sample was allowed to sit undisturbed for several hours to let any bubbles formed during filtering or during the filling process to escape.

Sample cells were individually placed at the intersection of the pump laser and the alignment laser on the sample stand. The position of each one was optimized so that both lasers passed through the center of each face of the cell on both entrance and exit. The angle of the sample was adjusted by retroreflecting the alignment beam. In this way the alignment laser was arranged to pass through the cell and intersect the path of the pump beam at 90° in the center of the cell. Beyond the cell it impinged on the photomultiplier housing. The position of the photomultiplier housing, and therefore photomultiplier, was adjusted by three dimensional micrometers to place the alignment laser on the center of the photocathode. The alignment laser was turned off and its hole into the dark box was sealed. The lid was placed on the dark box and the photomultiplier shutter was opened to begin data collection.

Chapter 4

Results

In this chapter experimental data that compare magnetic dipole scattering intensities in carbon tetrachloride, water, and benzene are presented. The intensity dependence of the nonlinear magnetic dipole response is reported along with confirmation of the linear intensity dependence of the electric dipole response. These results confirm that the intensity has not reached the typical electric nonlinear intensity regime. The ratio of the magnetic to electric dipole responses versus intensity is shown to be linear and to saturate at a value of $1/4$. The intensity dependences of each dipole response, the ratio of the responses, and the saturation of the ratio at a value of $1/4$ are all shown to support the theory of Optical Magnetism developed in Chapter II.

4.1 Magnetic Dipole Scattering

4.1.1 Sample Properties

Strong magnetic dipole scattering was unexpectedly observed in 2007 [1] in several dielectric liquids. Since the liquids in question, water, carbon tetrachloride and benzene, have no resonances near the pump wavelengths of 775nm and 810nm the original results clearly are not due to electronic resonances of any kind. The absence of resonances was confirmed by UV-Vis absorption in the spectral range of 200nm-1100nm using low intensity excitation at room temperature (Figs. 4.1 - 4.3).

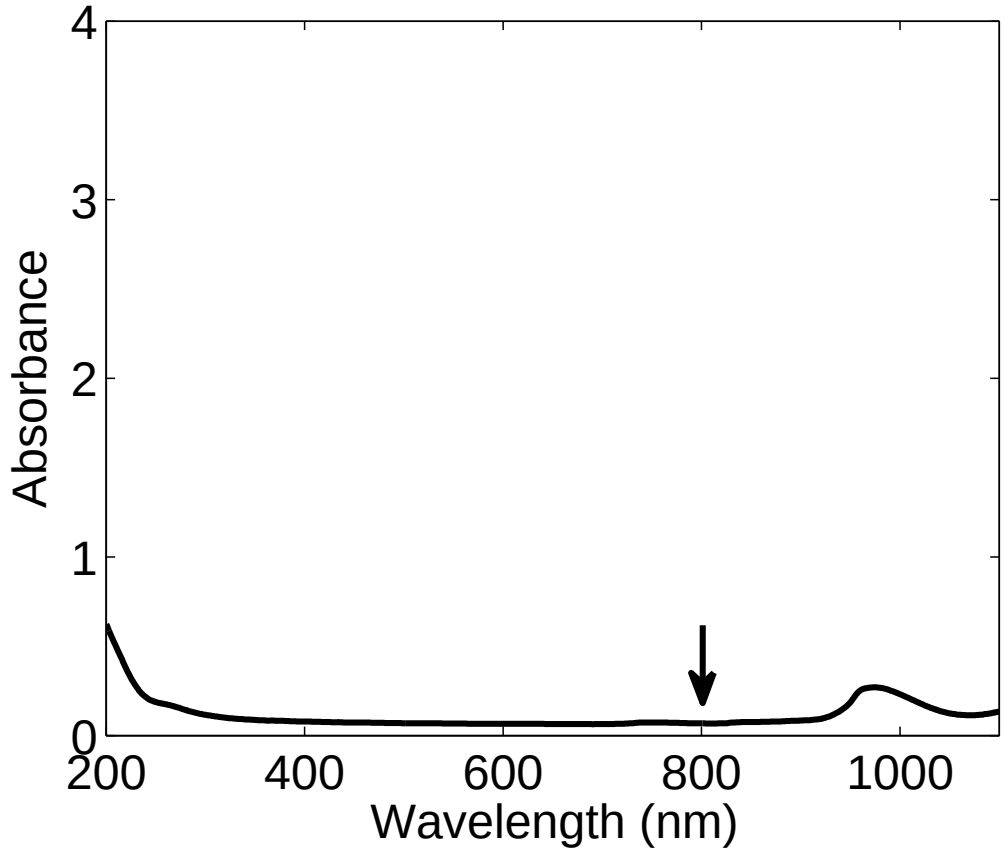

Figure 4.1 Absorbance spectrum of distilled water in Hellma QS quartz cell. No significant resonances are seen near the pump wavelengths of 775nm and 810nm. The arrow indicates the regime of exciation in the experiments. The small feature at 970nm is attributed to a combination of symmetric and antisymmetric stretching modes in the water molecule.

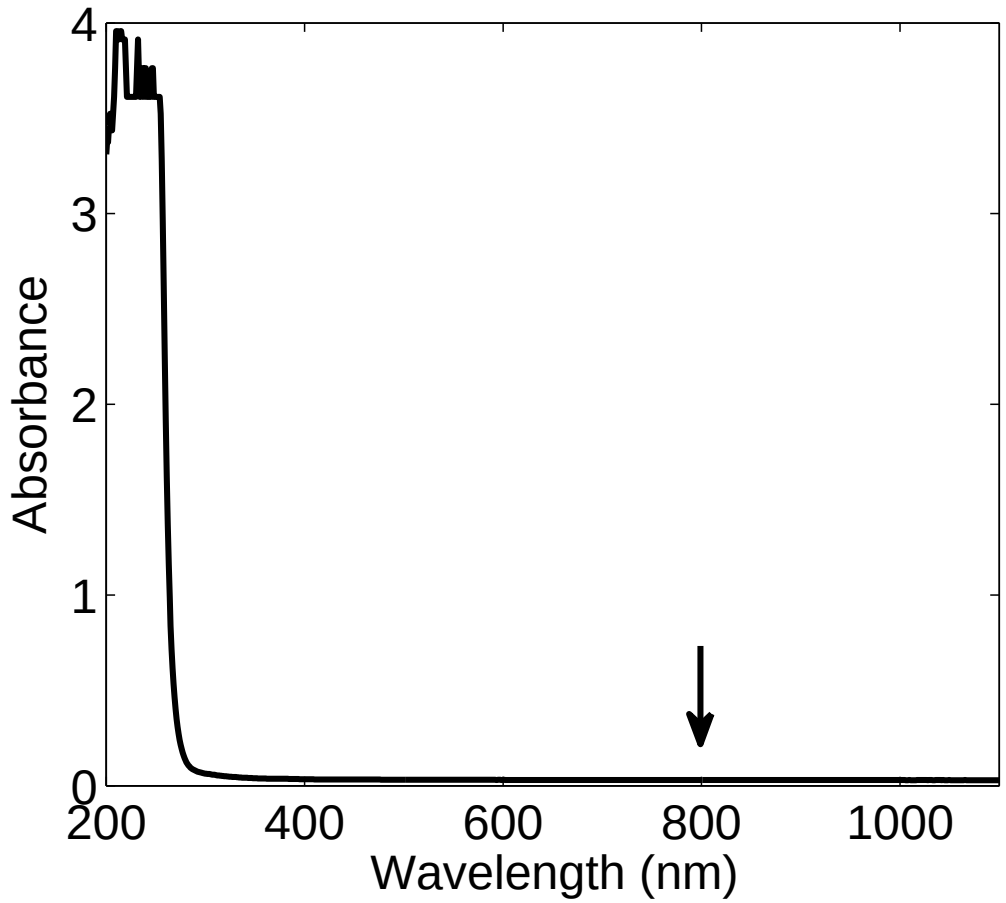

Figure 4.2 Absorbance spectrum of carbon tetrachloride in Hellma QS quartz cell. No significant resonances are seen near the pump wavelengths of 775nm and 810nm. The arrow indicates the regime of exciation in the experiments. The large feature on the left is strong UV absorption that saturated the spectrophotometer resulting in the jagged appearance for large absorbance.

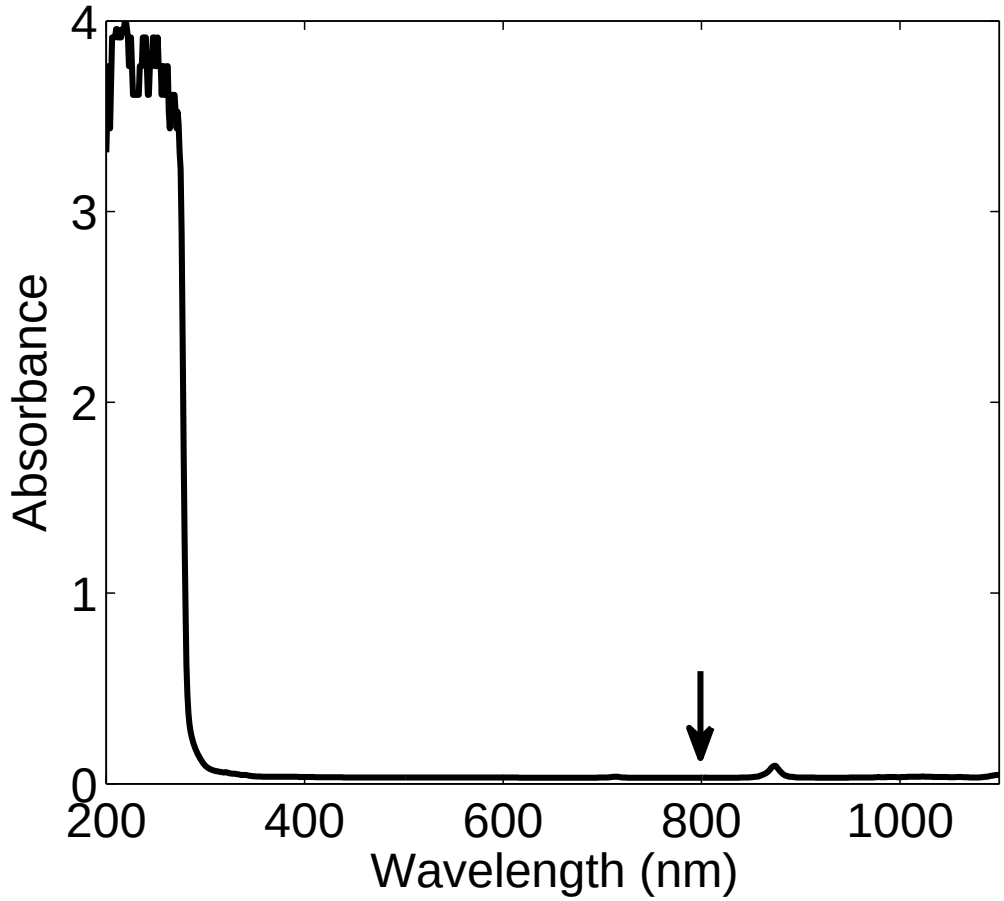

Figure 4.3 Absorbance spectrum of benzene in Hellma QS quartz cell. No significant resonances are seen near the pump wavelengths of 775nm and 810nm. The arrow indicates the regime of exciation in the experiments.

This also confirms that there are no significant impurities in the liquids to effect the results of scattering experiments. In such a pure dielectric sample, far off resonance, a beam of light will pass through the sample uneffected. However, even in a highly purified liquid with no suspended impurities, thermal fluctuations of density cause local changes in index of refraction. These index fluctuations act as scattering centers. A small fraction of light will be Rayleigh scattered perpendicular to the original direction of propagation.

4.1.2 Magnetic Dipole Scattering Over the Visible and NIR Spectrum

The earliest experiment in Transverse Optical Magnetism was a magnetic dipole scattering experiment performed by Oliveira [1] in a slightly different geometry than that described in Chapter 3. Rather than using a square quartz cuvette illuminated from the side by a low

intensity beam, a rather high intensity beam ($I < 10^{13} W/cm^2$) was focused weakly through the meniscus of carbon tetrachloride held in a cylindrical glass holder. Scattered light passed through the cylindrical wall of the holder into the collection optics and detector. This procedure is described in more detail in reference [1]. The use of relatively high intensity caused white light generation due to the onset of nonlinear phase modulation. Scattered electric and magnetic dipole signals were recorded at several different wavelengths to determine if there was any dependence on the excitation wavelength. By pumping the sample at 775nm and placing a 10nm FWHM bandpass filter in front of the detector, radiation patterns for scattered light were determined at many wavelengths in the visible and NIR spectrum.

One result, shown in Fig. 4.4, was obtained in carbon tetrachloride pumped at 775nm. Scattered light was recorded at 640nm and used to prepare polar plots of the radiation pattern. Similar electric and magnetic dipole patterns were recovered from 390nm to 775nm but gave similar results and are not shown.

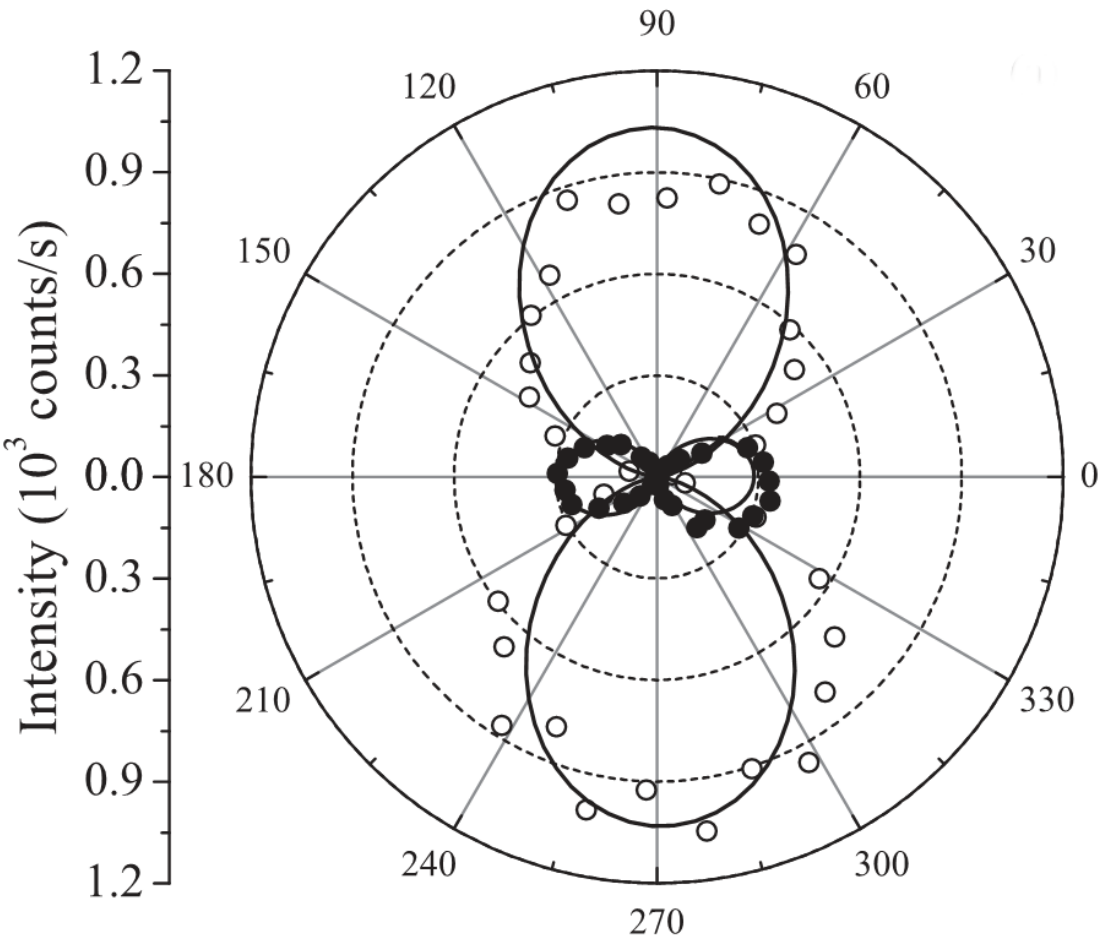

Figure 4.4 Experimental intensity patterns for electric (open circles) and magnetic (solid circles) scattering measured using amplified pulses, (775nm) measured at 640nm, in CCl_4. The solid lines are fits to the data by $\sin(\theta)^2$ and $\cos(\theta)^2$ respectively.

The reader may note that the data in Fig. 4.4 is quite noisy. The nonlinear processes that contribute to white light generation are dependent on local fluctuations of density and index of refraction within the focal volume caused by incipient self-focusing. To improve the experimental signal to noise ratio we made use of three improvements. First, the quartz cuvette geometry described in Chapter 3 was used to eliminate the air/meniscus interface at the input of the cylindrical glass holder. Second, the intensity was reduced by almost three orders of magnitude to $2.2 \times 10^{10} W/cm^2$ to eliminate white light generation and other electric nonlinearities. This reduction in intensity was the result of using an 80MHz unamplified modelocked Ti:Sapphire laser source. Third, the pulse to pulse noise was reduced to well below 0.5%, much lower than the amplified system, again as the result of using the mode-locked oscillator. The pump wavelength changed to 810nm for the oscillator experiments but no change in the electric and magnetic dipole pattern was observed.

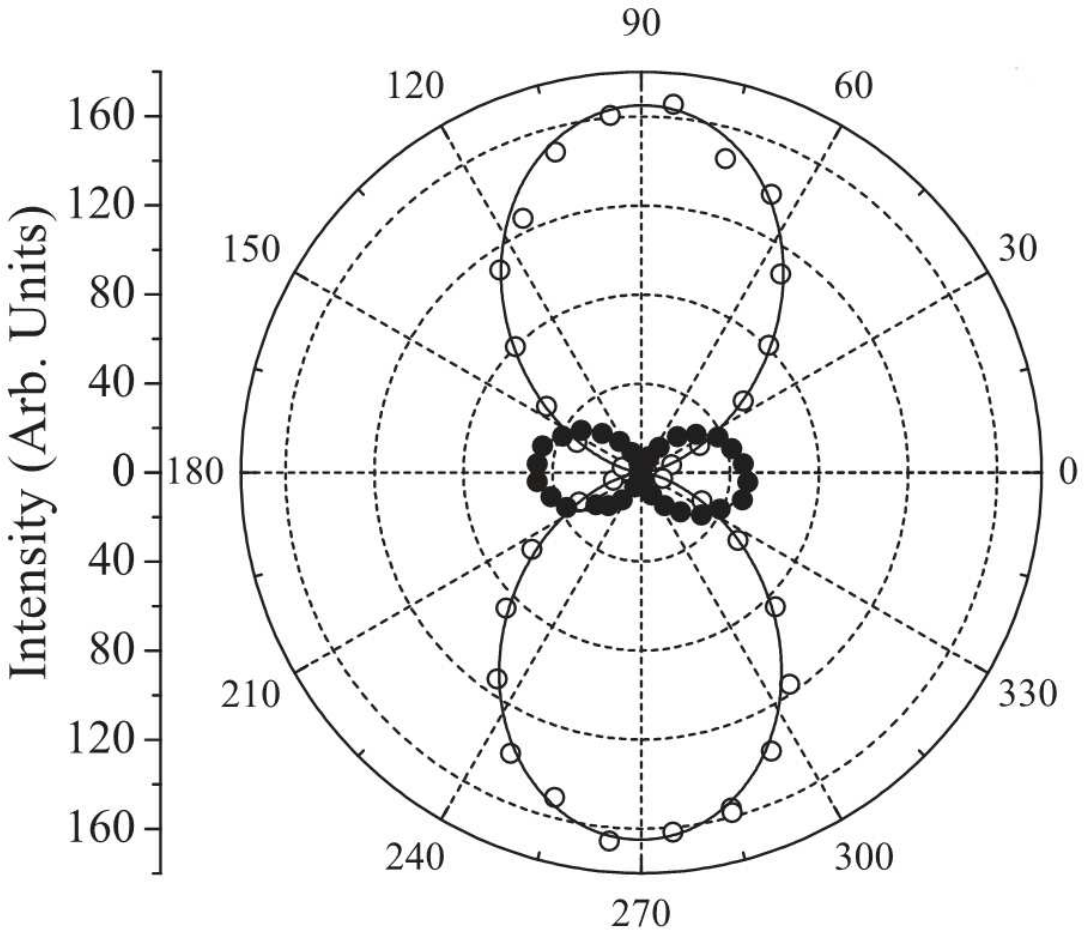

Figure 4.5 Experimental intensity patterns for electric (open circles) and magnetic (solid circles) polarization directions measured using unamplified pulses (810nm), measured at 810nm, in CCl_4. The solid lines are fits to the data by $\sin(\theta)^2$ and $\cos(\theta)^2$ respectively, indicating that the data is dipolar to an excellent degree.

It can be seen in Fig. 4.5 that the noise in the signal is dramatically reduced while the magnetic scattering signal remains at the same intensity relative to the electric dipole signal seen in Fig. 4.4. Scattering with the electric field polarization is now well-fitted by a dipole pattern $\sin^2(\theta)$. Expanding the view of the magnetic dipole signal alone in Fig. 4.6 we see that the magnetic dipole pattern also fits $\cos^2(\theta)$ very well. There is no evidence of quadupolar contributions in the data. The null in the dipolar distribution of Fig. 4.6 is very well defined.

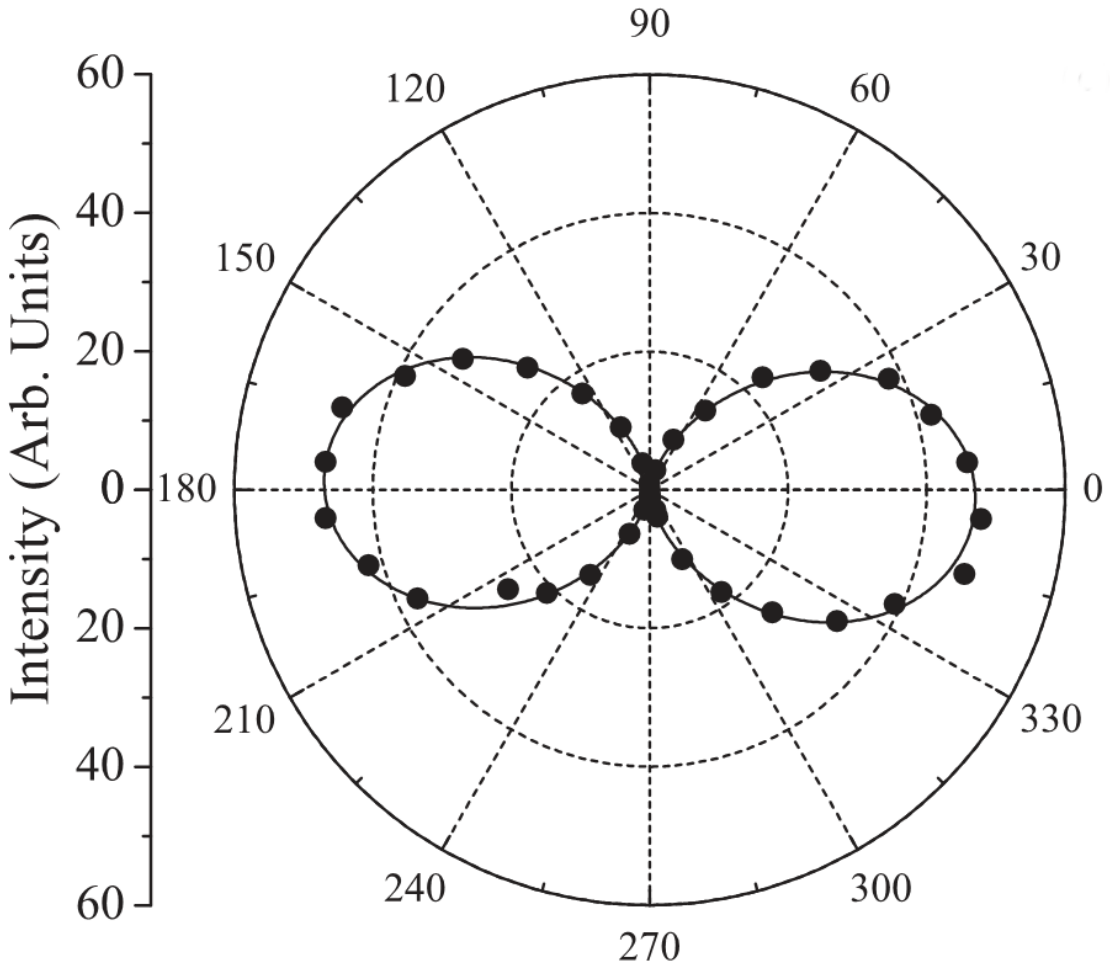

Figure 4.6 Magnified view of the magnetic dipole response using unamplified pulses (810nm), measured at 810nm, in CCl_4. The solid line is a fit to the data by $\cos(\theta)^2$ indicating that the data is dipolar to an excellent degree.

4.1.3 Magnetic Dipole Scattering Dependence on Molecular Structure

After observing magnetic dipole scattering in CCl_4, additional observations were sought in other samples over a range of intensities. First, in the high intensity ($I < 10^{13} W/cm^2$) regime a regeneratively amplified Ti:Sapphire laser with a repetition rate of 1kHz (Clark MXR CPA-2001) was used. This source produced pulse trains of 150fs pulses at 775nm. Up to 3.5mW of power was focused into the quartz cell containing deionized water. The geometry and photon counting method described in Chapter 3 were used to detect the scattered light. Because this experiment was performed in the white light generation regime data was collected at several wavelengths, but again, as was the case for carbon tetrachloride,

no wavelength dependence of the MD/ED scattering ratio was observed. Figure 4.7 shows the result of this experiment when pumped at 775nm and measured at 775nm as well. The electric and magnetic signals remain dipolar but with the increased noise expected from the amplified pump and higher intensity.

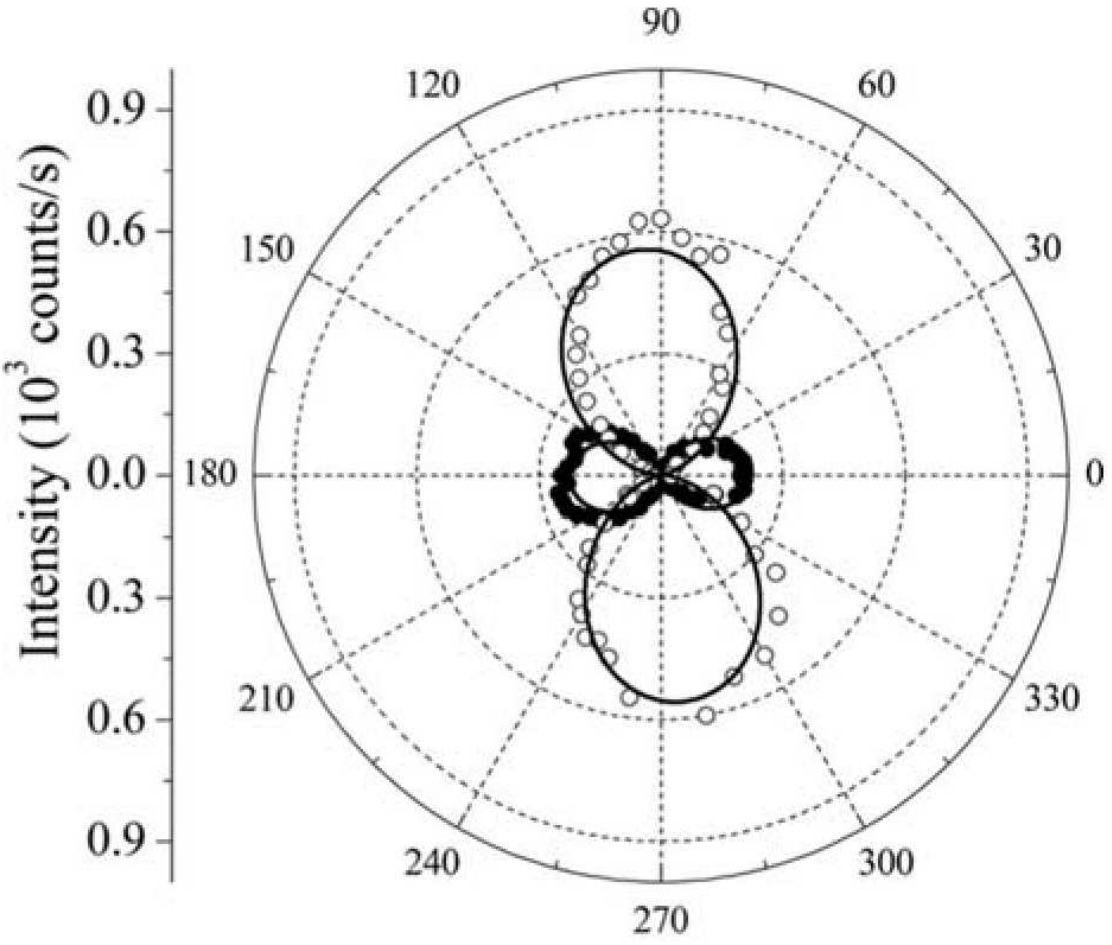

Figure 4.7 Experimental intensity patterns for electric (open circles) and magnetic (solid circles) polarization directions measured using amplified pulses (775nm), measured at 775nm, in deionized water. The solid lines are fits to the data by $\sin(\theta)^2$ and $\cos(\theta)^2$ respectively.

Pulsed experiments confirmed that the magnetic dipole scattering process and continuum generation could be induced in H_2O and C_6H_6 as well as carbon tetrachloride with no quantitative differences. This suggests a broad universality of this phenomenon.

Subsequent experiments were performed with the lower noise, unamplified pulses of approximately 100fs duration from the mode-locked oscillator. In this series of measurements approximately 400mW of average power at 810nm was focused through a 2cm focal length lens into the liquid. The peak intensity was limited to $I \ll 2 \times 10^{10} W/cm^2$, 1000 times

below the white light generation threshold of water [26]. Synchronous detection was used to increase the signal to noise ratio of the data further. This was achieved through mechanical chopping of the pump beam and measuring the signal with a polarization-insensitive EG&G FND-100 photodiode connected to a Stanford Research SR530 Lock-in Amplifier. The data was measured at the fundamental frequency, 810nm, and is shown in water and benzene in Figs. 4.8 and 4.9 respectively.

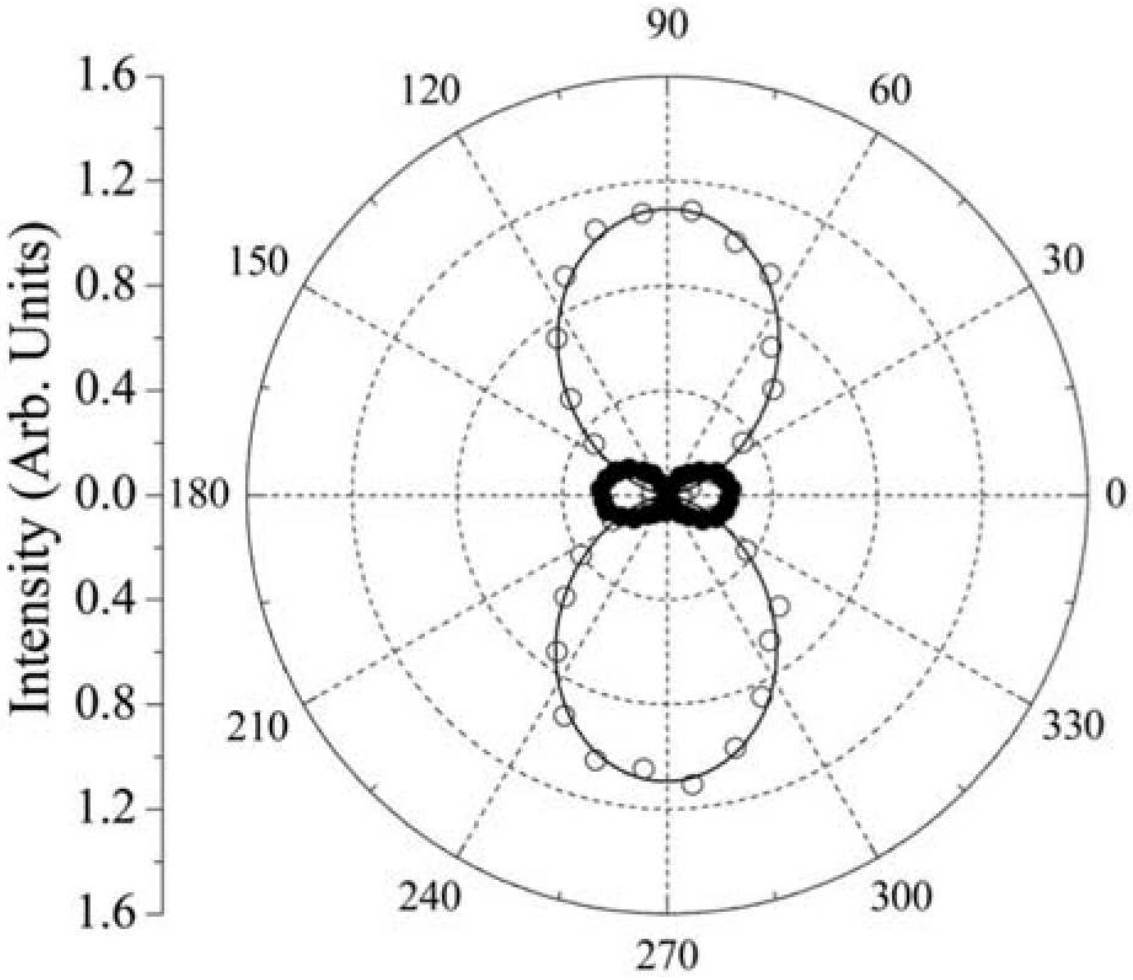

Figure 4.8 Experimental intensity patterns for electric (open circles) and magnetic (solid circles) polarization directions measured using unamplified pulses (810nm), measured at 810nm, in deionized water. The solid lines are fits to the data by $\sin(\theta)^2$ and $\cos(\theta)^2$ respectively, indicating that the data is dipolar to an excellent degree.

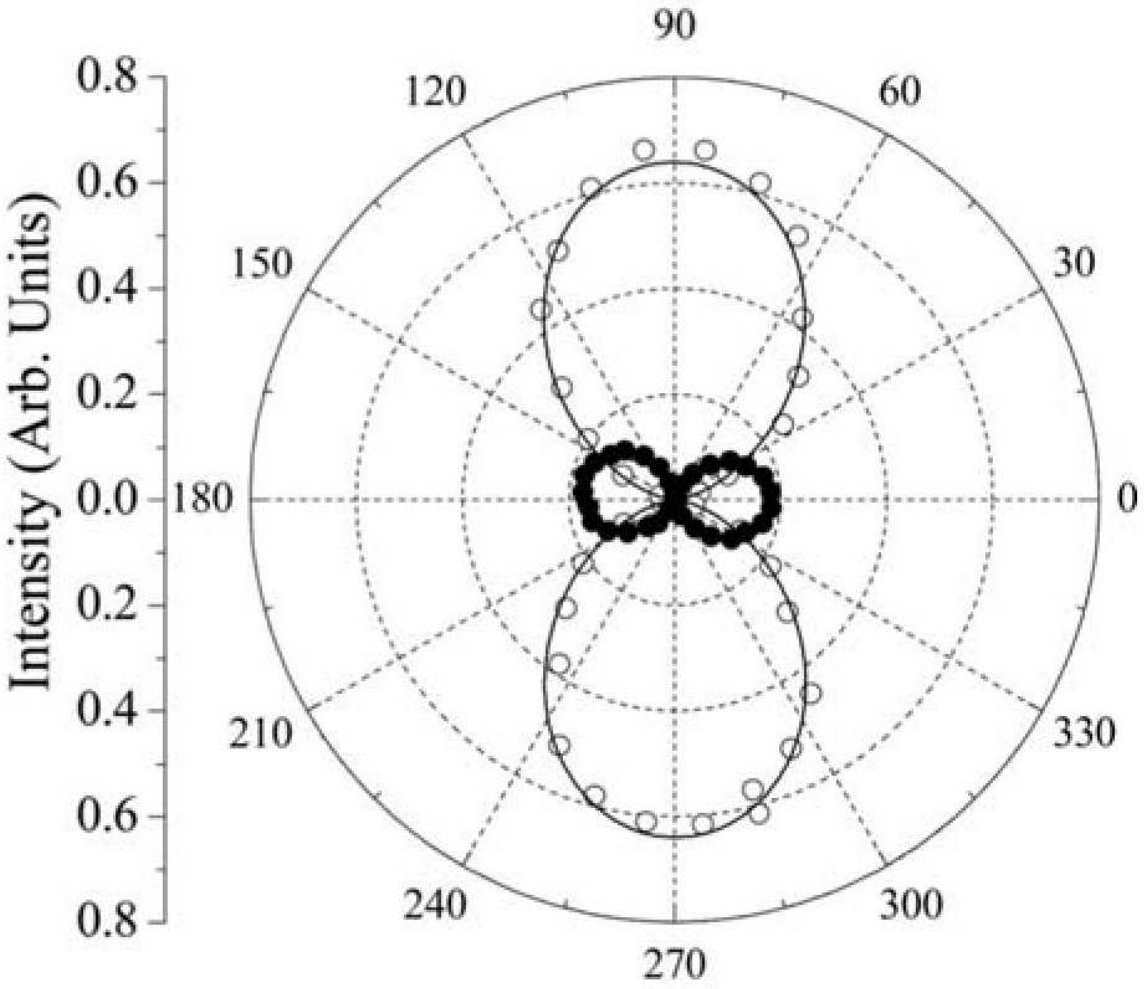

Figure 4.9 Experimental intensity patterns for electric (open circles) and magnetic (solid circles) polarization directions measured using unamplified pulses (810nm), measured at 810nm, in benzene. The solid lines are fits to the data by $\sin(\theta)^2$ and $\cos(\theta)^2$ respectively, indicating that the data is dipolar to an excellent degree.

4.1.4 Intensity Dependence of Magnetic Dipole Scattering and the Electric to Magnetic Dipole Scattering Ratio

The next experiment focused on the intensity dependence of the magnetic scattering signal. For this experiment we returned to the carbon tetrachloride sample because of its centrosymmetric structure. To determine the low intensity magnetic response, the pump laser was replaced with a linearly polarized, CW, Argon laser at 514nm capable of producing 1-10W of power. Focused, this laser provided $10^5 W/cm^2$ at maximum intensity. At this intensity no measureable magnetic dipole scattering was found. This placed a lower bound on the

intensity regime to be explored to find the intensity dependence of the magnetic dipole response.

A broad range of intensities was then investigated, beginning at $10^5 W/cm^2$ and extending to the white light generation regime in order to observe the onset of the magnetic scattering. While the unamplified laser system provided lower noise, it did require focusing of the beam to achieve sufficient intensity. Unfortunately for an intensity scan, the focal position changes as a function of intensity due to nonlinear self-focusing. Using this pump laser required realigning the system for each step in intensity. Making such a procedure reproducible was both challenging and time consuming, so all subsequent experiments using the amplified laser system were performed with a collimated beam. This allowed measurement of a wide range of intensities from $10^5 W/cm^2$ to $10^{10} W/cm^2$.

Using the R636 photomultiplier and the procedure of Chapter 3 a scan of intensity from approximately $10^6 W/cm^2$ to $10^8 W/cm^2$ was performed for carbon tetrachloride. To find the intensity dependence of both the electric and magnetic dipole signals it was only necessary in practice to find the dependence of the ED and MD scattering maxima on intensity. Thus, at each step in intensity data pairs were taken with the input polarization and analyzer in the electric signal maximum and the magnetic signal maximum orientations.

In this regime of intensities there should be no nonlinear electric scattering effects, so a linear dependence of scattered light intensity with vertical polarization is expected versus intensity. The growth of the magnetic scattering signal relative to the electric one is shown as squares referring the right axis of Fig. 4.10 taken from Ref. [2]. The dashed line is a quadratic line of best fit for the data displayed indicating that the dependence is quadratic with intensity. The ratio of the magnetic dipole signal to the electric dipole is plotted as circles refering to the left axis. The solid line is a line of best fit indicating that the ratio follows a linear dependence as a function of intensity.

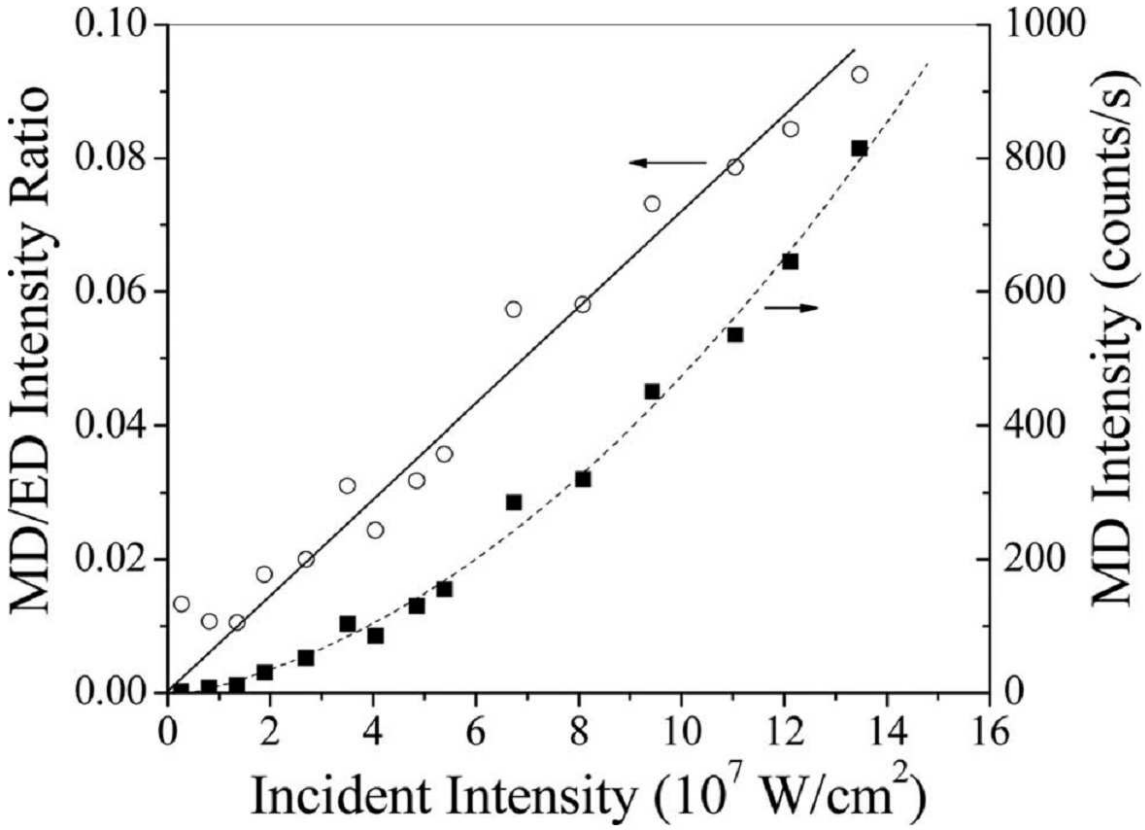

Figure 4.10 Experimental intensity dependence of magnetic dipole scattering (solid squares) and magnetic to electric dipole ratio (open circles) versus input intensity in CCl_4. The dashed line is a quadratic regression through the magnetic dipole scattering data. The solid line is a linear regression through the ratio data.

The intensity dependence of the onset of magnetic response was determined with good accuracy in this way. However, higher intensities were clearly needed to see the development of magnetic saturation. In the next experiments a wider intensity range was used in order to push the sample toward and see magnetic saturation. Given the results of the previous experiments in the unamplified laser system where the magnetic dipole signal reached the full $1/4$ of the electric dipole signal, it was believed that the full intensity dependence up to saturation and beyond could be seen with this setup. The ratio of magnetic to electric dipole signal is plotted in Fig. 4.11 taken from Ref.[27].

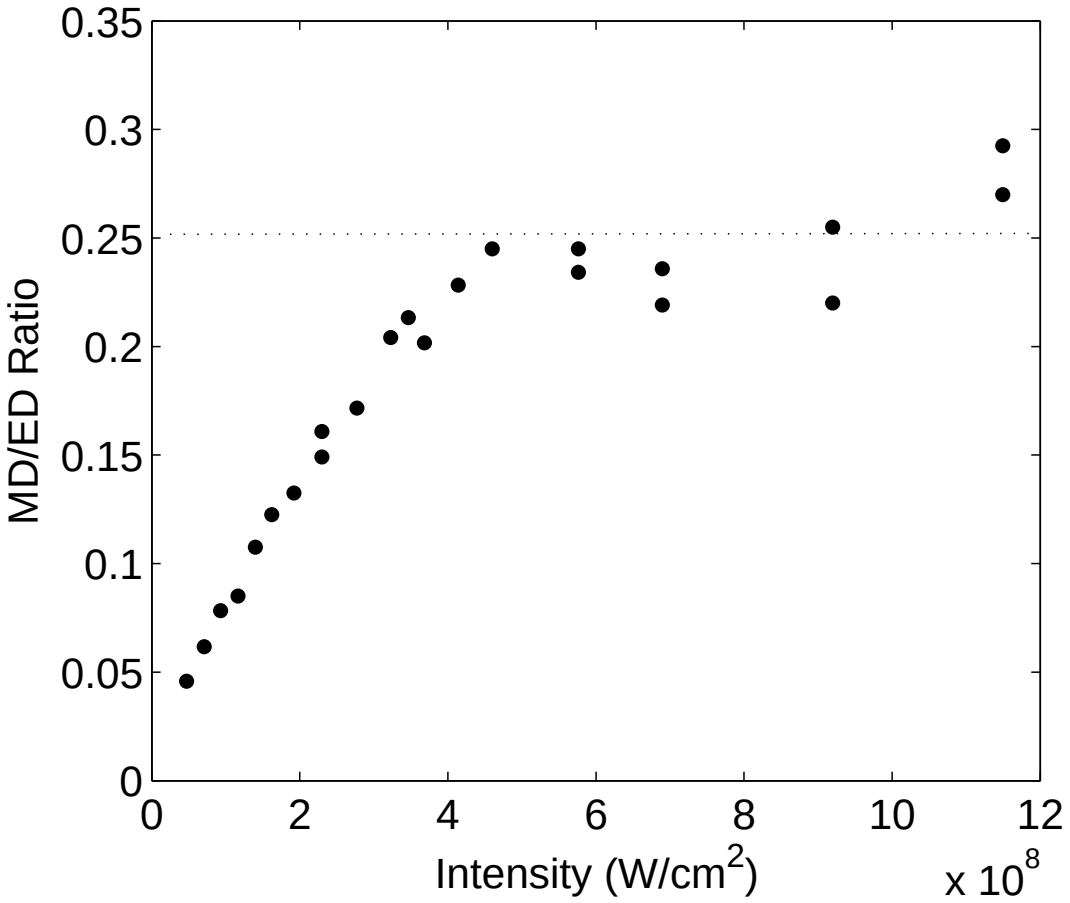

Figure 4.11 Experimental intensity dependence of magnetic dipole scattering versus input intensity in CCl_4 over a wide range of intensities including the saturation point at approximately $4.5 \times 10^8 W/cm^2$.

The linear dependence of the ratio on intensity is seen to continue up to a saturation value of $1/4$ in agreement with the discussion of Sec. 2.1.3.

The data of Fig.4.12 provide evidence of the magnetic response limitation described in Sec. 2.1.3. Hence, it is desirable to confirm how general this behavior might be experimentally. The measurements were therefore made for each of the three liquids over a wide intensity range. The magnetic to electric scattering ratios for all three liquids has been plotted as a function of intensity in Fig. 4.12.

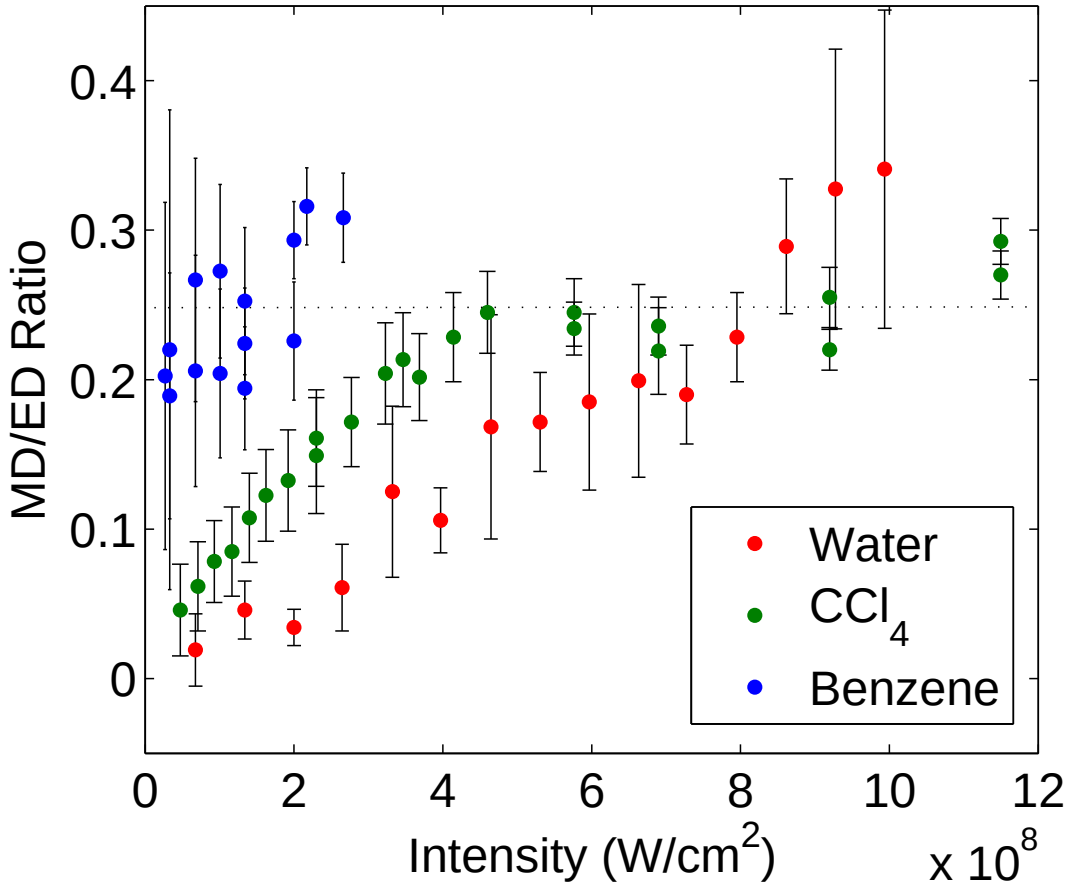

Figure 4.12 Experimental intensity dependence of magnetic dipole scattering versus input intensity in Water (red), CCl_4 (green), and Benzene (blue).

In Fig. 4.12 the ratio of magnetic to electric response of each liquid can be seen to approach the "'saturation"' value of $1/4$ linearly as a function of intensity. Since the magnetic response was shown to be quadratic in Fig. 4.10, this also confirms that the electric dipole response is still in the linear regime. We also see that the slope of the intensity dependence in the "'linear"' regime below an MD/ED ratio of 0.25 is different for each liquid. Benzene appears to have a very steep initial onset slope. In fact, it was found that all data points taken were not statistically different from $1/4$. It was found not to be possible to reliably measure the intensity at the low powers making it impractical with the amplified laser source to search for the linear ratio dependence in the case of benzene. Future experiments with lower intensity sources may make this possible. This seemingly strong magnetic response for benzene will provide important perspective for discussions of applications in Chapter 5.

Thermal nonlinearities cannot contribute to the measured quadratic signal. While random density fluctuations in the liquid due to thermal energy are possible, the efficiency of

second harmonic generation would vary wildly as the fluctuations change with each laser pulse. The laser does not deposit enough heat to cause a significant temperature change. The lack of resonances near the pump wavelength means the absorption is extremely low, as seen in Figs. 4.1-4.3. The laser pulses are of order $1\mu J$ in energy. When combined with an absorption of order one percent the total energy deposited approaches the nJ level. The heat capacity of the sample is approximately $5J/K$, so the laser must fire of the order one billion times to raise the temperature of the sample by $1K$. In the time required to fire this many times, any heat gained would be exchanged with the air keeping the sample at room temperature. Even on the microscopic scale, heating cannot play a role. The pulses are of order 100fs in duration and separated by microseconds to milliseconds. The time scale for phonon interactions is picoseconds. Thus, the laser pulse has entered the sample, excited electron motion, and re-emitted a photon in the perpendicular direction before any phonon processes can take place. The next pulse arrives after microseconds or longer, well after any phonon processes decay back to the ground state.

A similar experiment was performed at high power in which the analyzing polarizer was rotated rather than the input polarization. The result was a beam width dependent de-polarization of the measured scattered light. The results have not yet been successfully interpreted, so the data and discussion are presented in Appendix D.

Chapter 5
Conclusions

In this chapter we discuss the experimental results, in relation to the theory derived in Chapter 2, and make predictions based on that theory about future possibilities. It is shown that the Complete Lorentz Oscillator Model correctly predicts that Transverse Optical Magnetism is a second order process that can take place in materials with centrosymmetry. Interactions dependent on both an electric field and a magnetic field have symmetry restrictions that differ from those of the more typical, second order, nonlinear interaction involving two electric fields. Here we summarize experimental results showing that the quadratic nonlinearity of interest here takes place in centrosymmetric media and that the maximum current density that can be directed from linear motion into solenoidal motion to generate magnetic effects is $J_M = -1/2J_E$, in agreement with theory. The implications of intense optical magnetic effects are explored as a new direction for nonlinear optics with implications for the generation of large magnetic fields, terahertz radiation, and solar power without the use of semiconductor solar cells.

5.1 Maximum Magnetic Scattering

In this work, unexpectedly large magnetic dipole scattering was observed in dielectric liquids as described in Section 4.1.2. These results contradicted previous arguments by Landau and Lifshitz predicting that magnetic effects at optical frequencies are unimportant [5]. Atoms were deemed to be too small to support magnetic effects at optical frequencies. In this section we identify the flaw in this earlier argument and discuss the evidence supporting the opposite conclusion based on theory developed in Section 2.1.

Since the polarization states of radiation due to electric and magnetic dipoles are separable in the perpendicular direction, as described in Section 3.1, we conclude that the signals of Figures 4.4 and 4.5 are independent measurements of the electric and magnetic responses generated in the samples. The fits to dipolar patterns for each data set, particularly those

using the low noise oscillator in Fig. 4.5, are excellent. Hence, we must conclude that they arise from orthogonal transverse dipole sources. Hence, they must correspond to electric and magnetic dipoles. Moreover, these signals cannot be due to linear rotary effects or quadratic electric nonlinearities, especially in the case of CCl_4. Carbon tetrachloride is not chiral, it has no permanent dipole, and is centrosymmetric. Alternative optical processes cannot explain our results. Additionally, the results appear to be universal in dielectrics. The results of Figures 4.7, 4.8, and 4.9 in different liquids with different electronic and molecular structures are similar. Thus, we conclude that intense magnetic dipole radiation has been generated at optical frequencies and that a new chapter in nonlinear optics has begun.

Extracting the ratio of the signals in Figures 4.4 through 4.9 we find that in each case the maximum magnetic dipole signal attainable is approximately $1/4$ the size of the electric dipole signal. The ratio data is compared in Table 5.1.

Material (pump light condition)	Maximum MD/ED Ratio
Benzene (unamplified)	0.28 ± 0.04
Carbon tetrachloride (amplified)	0.22 ± 0.05
Carbon tetrachloride (unamplified)	0.28 ± 0.03
Carbon tetrachloride (unamplified)	0.27 ± 0.04
Water (amplified)	0.38 ± 0.10
Water (unamplified)	0.23 ± 0.04

Table 5.1 Ratio of the maximum of the magnetic dipole signal to the maximum of the electric dipole signal for benzene, carbon tetrachloride, and water under both amplified and unamplified pump light conditions.

The measurements of Table 5.1 were repeated 10 times each to estimate standard deviation. We see that there is no doubt that magnetic response can exceed predictions of the traditional multipole expansion by five orders of magnitude and the theory of Landau and Lifshitz must be incorrect. There is no long range order or structure in these dielectric liquids, so the bodies generating the magnetic signal are individual molecules.

In view of the conclusion we compare the results with the model developed in Section 2.1.3. It was predicted, theoretically, that the maxiumum amount of current that can be deflected from linear motion, caused by the electric field, into solenoidal motion due to a magnetic field is $1/2$. It is well known that the sources of radiation are currents and that the intensity of light collected in our experiment depends on the source current squared. The maximum solenoidal current is $1/2$ so the maximum magnetic dipole signal due to that current is $(1/2)^2 = 1/4$. This is in excellent agreement with our results in Table 5.1. Further, the derivation of the maximum current made no assumption about the electronic structure of the matter supporting the solenoidal current. Thus, we expect to find the same maximum value of $1/4$ universally in all dielectric materials, in agreement with the experimental

results of Section 4.1.2.

5.2 Symmetry and Frequency Considerations

As described in Section 4.1.4, the intensity dependence of the magnetic dipole was observed to be accurately quadratic in carbon tetrachloride . This result stands in stark contrast to previous nonlinear optics as outlined in Section 1.3 in which centrosymmetry prohibits quadratic nonlinearities. The results of this research nevertheless clearly establish that centrosymmetric materials can support second order magnetization at the frequency of the incident light.

Liquids have no long range order to develop nonlinear effects. The random positions of molecules act as an amorphous material and thus have no structure. An amorphous material can be treated as centrosymmetric over distances containing several molecules since no preferred direction is defined. Thus, we expect no second order effects in any liquid. To eliminate the possiblity of stray second order nonlinearities we can also choose a liquid that is centrosymmetric on the molecular scale as well. Carbon tetrachloride has a tetragonal structure, group T_d, which is of the cubic, centrosymmetric type. Thus, in liquid carbon tetrachloride the symmetry can only be broken by a surface. In the setup described in Chapter 3 care was taken to exclude the quartz/liquid interface from the observed region. The collection optics were designed to collect light only from the center of the cuvette and the peak intensity of the beam was always centered in the liquid volume.

All these precautions aside, if any second order process took place involving only the electric fields of the light, the radiation developed would have been at an even harmonic of the pump wavelength. All previously known second order processes induce signals at either 0ω (a DC effect) or 2ω (a second harmonic generation effect). However, in the results reported here we measured scattered light at the fundamental frequency. No electric dipole can be created via a second order purely electric effect at the fundamental frequency. A magnetic field can, however, deflect electrons into a curved motion to form a magnetic dipole at the fundamental frequency. Moreover such a dipole would be oriented parallel to the magnetic field and perpendicular to the electric field. Thus, the expected polarization and frequency of the elastic scattering signals reported here can only be due to magnetic dipole response.

The Complete Lorentz Oscillator Model of Section 2.1.5 predicted that in second order a curved motion can be driven by light that forms a magnetic dipole oriented parallel to the driving magnetic field. In agreement with this, the numerical results in Figs. 5.2 and 5.3

showed that just such a curved motion is expected classically. While the projection of the motion along the $\hat{z}$ direction is at 2ω, the rotational motion about a point in the center of the arc is at ω. This circular motion is indeed a magnetic dipole that can only exist in second order. The mechanism requires an electric field to add energy to the system by initiating linear motion and the magnetic field causes a deflection which is solenoidal in character. We reiterate that all these theoretical expectations are consistent with the experimental results.

5.3 Predictions of Additional Magneto-electric Effects

We now turn to predictions of the CLOM to analyze additional effects that may be studied in the future. The following sub-sections examine further implications of the classical expressions derived earlier to describe light-induced motion in bound electron systems. The results were:

$$x(t) = A_{x0,\omega}\cos(\omega t + \phi_0) \tag{5.1}$$

$$z(t) = A_{z1,0}\sin(\phi_0) + A_{z1,2\omega}\sin(2\omega t + \phi_0 - \phi_1) \tag{5.2}$$

and predict two magnetically-induced electric dipole effects that have not yet been thoroughly discussed.

5.3.1 Magneto-electric Second Harmonic Generation

In Eq. (5.2) the second term that oscillates at 2ω. That is, it predicts electric dipole radiation at 2ω in centrosymmetric media, a result that can only be magnetic in origin. Consequently, this predicts megneto-electric second harmonic generation. Unfortunately, the orientation of the dipoles does not allow for easy observation of this radiation. Because the radiation is z polarized, the oscillations occur along the direction of propagation of the light. This means that the dipoles do not radiate at all along the direction of propagation. Instead they radiate perpendicular to the direction of propagation. However, since the excitation pulse is moving, each induced dipole is slightly out of phase with its neighbors due to the finite propagation speed of the light. Hence, contributions to the radiated field off-axis are not perfectly in phase and do not form a beam of coherent light at the second harmonic wavelength.

Constructive interference of the second harmonic waves can be synchronized in a special direction. The analysis incorporates dispersion at the ω and 2ω wavelengths and is similar

to the approach used to describe generation of Cherenkov radiation by high energy particles passing through dielectrics.

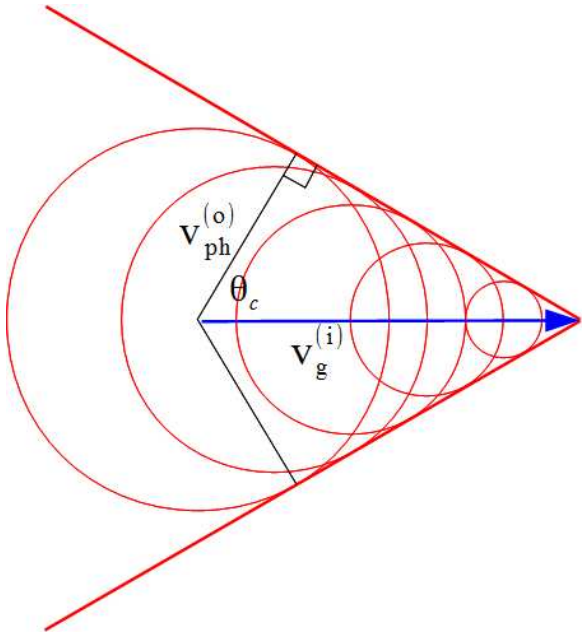

Figure 5.1 An incident excitation moves through a dielectric medium at group velocity $v_g^{(i)}$. The electromagnetic disturbance of its passage causes radiation to be emitted spherically from each point along its path. At angle θ_c the oscillations of the radiation are in phase and form a wavefront propagating with phase velocity $v_{ph}^{(o)}$.

As the incident passes through the medium at its group velocity $v_g^{(i)}$, a second wavelength of light is generated. The harmonic light propagates through the medium in all directions, but in only one direction do its expanding spherical waves form a form a wavefront with uniform phase. This direction is found by determining the angle at which the excitation velocity, $v_g^{(i)}$, and the emission velocity, $v_{ph}^{(o)}$, form a right triangle. This angle, θ_c, dictates the cone formed by the emitted phase front. A detector placed off-axis at angle θ_c will detect light at the harmonic wavelength.

If the velocities of the excitation and emission are similar, the angle θ_c can be quite small. For a sufficiently small angle, and propagation confined to a waveguide like an optical fiber, the emitted light will then be totally internally reflected by the air-dielectric interface. Second harmonic light generated by the excitation pulse will be guided down the fiber to exit at the far end. In such a geometry it is easy to imagine that the entire cone of emitted light could be collected for detection.

Calculation of the efficiency of conversion from the excitation wavelength into the second harmonic requires a coupled mode solution such as the one presented in Appendix E.

5.3.2 Magneto-electric Terahertz Generation

The zero frequency term in Eq. (5.2) is potentially useful for the generation of terahertz radiation. One of the methods of terahertz generation in common use today is optical rectification [28]. In this method a non-centrosymmetric crystal is excited by a high intensity light pulse of duration shorter than 1ps. The high intensity light pulse generates an electromagnetic field in the crystal at zero frequency by the process

$$P^{(2)}(0) = \chi^{(2)}(0;\omega,-\omega)E(\omega)E(-\omega) \tag{5.3}$$

The rectified field grows and subsides with the pulse as the intensity rises and falls. This transient field causes electron acceleration that generates the radiation. The bandwidth of the radiation is determined by the duration of the acceleration period. By choosing the pulse duration to be on the order of a picosecond, the frequency bandwidth of the radiation generated is approximately $\Delta\nu \propto 1/10^{-12}s = 10^{12}Hz = 1THz$.

A nearly identical method is possible using Transverse Optical Magnetism. In this case however the polarization is magneto-electric in origin. Therefore it obeys a relation like

$$P^{(2)}(0) = \chi^{(2)}(0;\omega,-\omega)E(\omega)B(-\omega) \tag{5.4}$$

and takes place in centrosymmetric media. This realization opens the door to THz generation in a host of new materials including silica glass.

5.3.3 Solar Power Generation

The zero frequency term in Eq. (5.2) can also be used to generate a constant voltage if the input light is sufficiently intense and continuous. Provided that the incident field does not change the occupation of energy levels of atoms in the medium, the classical theory is valid and can be used to estimate the efficiency of energy conversion by this means. In this section the possibilities of this interaction are explored through numeric integration of the equations of motion, 2.70 and 2.69. In order to meet the requirement that the incident field does not induce population changes the incident frequency is assumed to be detuned by more than the relevant transition linewidths, specified by γ_x and γ_z. The chosen field strengths are also assumed to correspond to two regimes: a low intensity regime where magnetic interactions are negligible and a high intensity regime where magnetically-driven polarizations attain

their maximum amplitude with respect to the linear electric polarization of the medium. On the other hand, when the electric field is increased by eight orders of magnitude, motion driven solely by E is no longer dominant.

Figures 5.2 and 5.3 present two trajectories calculated by direct integration of the Complete Lorentz Oscillator Model *including* the magnetic Lorentz force from Chapter 2. In each plot, the optical field is applied as a step function at time zero and frequency is detuned from electronic resonance by $\Delta_1/\gamma_x = \Delta_1/\Gamma_{12}^{(e)} = 1.67$. Normalized frequency parameters were assigned fixed values of $\omega = 1$, $\omega_x = \omega_y = 1.5$, $\omega_z = 0.2$, $\gamma_x = \gamma_y = \gamma_z = 0.3$. Figure 5.2 is calculated for an incident plane wave field of $E_0 = 1V/m$ and Fig. 5.3 is for $E_0 = 10^8 V/m$. In the first case, at low field strength, the trajectory lies almost entirely along the x-axis of the electric field, as expected for low intensity optical interactions. Motion driven by the electric field dominates the dynamics overwhelmingly. Magnification of the horizontal scale by 10^9 is necessary to make the component of the motion in the direction of propagation of light large enough to see. It is this small component that originates from the Lorentz force. In Fig. 5.3, the horizontal scale is only one hundredth that of the vertical axis and yet the motion along z has developed an amplitude much more comparable to that of motion along x.

It can be seen from both of these figures that motion driven by the optical fields reaches a steady state after only a few periods. The deviations from linear response along the electric field direction therefore appear on an ultrafast time scale in this simulation. The electron follows a strongly curved path and the centroid of the motion is displaced forward along the direction of propagation, away from the nucleus located at $x = y = z = 0$. Although E and B are similar in that they oscillate harmonically at the optical frequency and therefore have an average value of zero, E is a polar vector that reverses sign upon inversion, whereas B is an axial vector which does not. In combination, it is evident from Figs. 5.2 and 5.3 that these field components can drive a sizeable static displacement of bound electrons with respect to the nucleus.

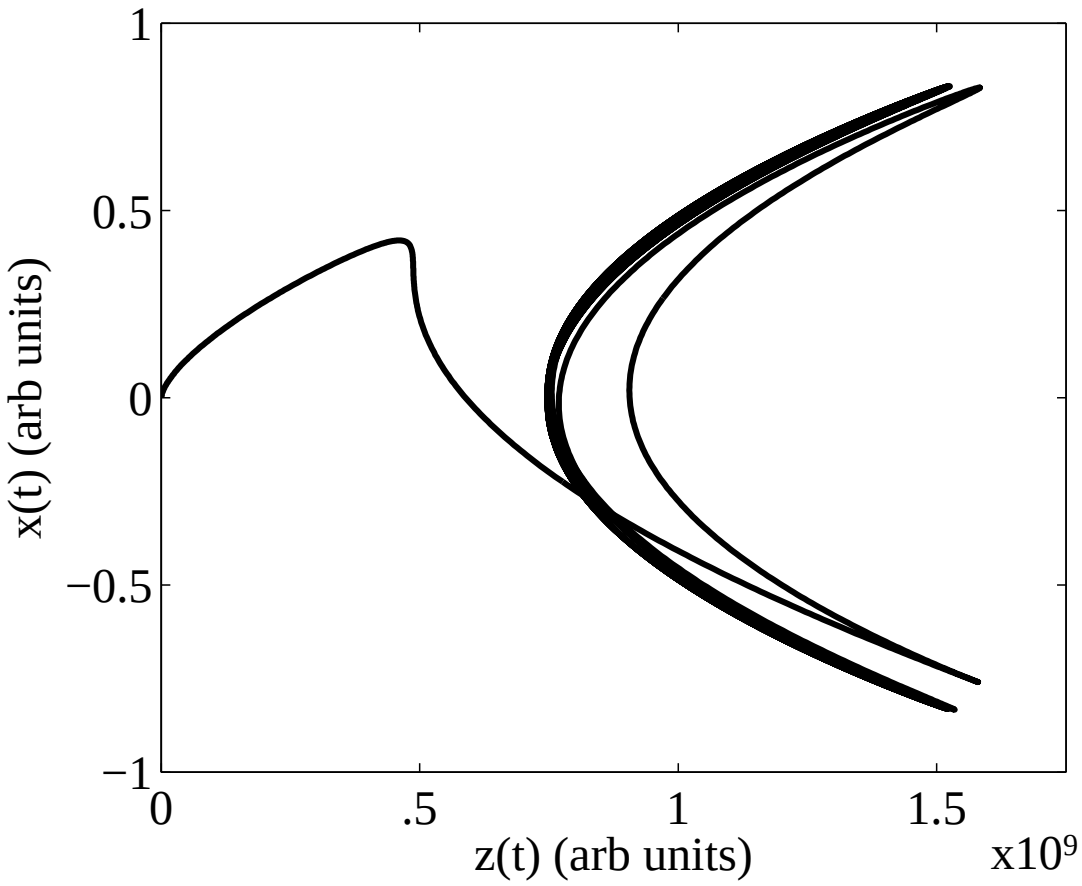

Figure 5.2 Trajectory of electron motion calculated by integration of the equations of motion for an incident electric field of strength $E_0 = 1V/m$. Note the axes differ by nine orders of magnitude. Frequency and linewidth parameters were chosen to be $\omega = 1$, $\omega_x = \omega_y = 1.3$, $\omega_z = 1$, and $\gamma_x = \gamma_y = \gamma_z = 1$.

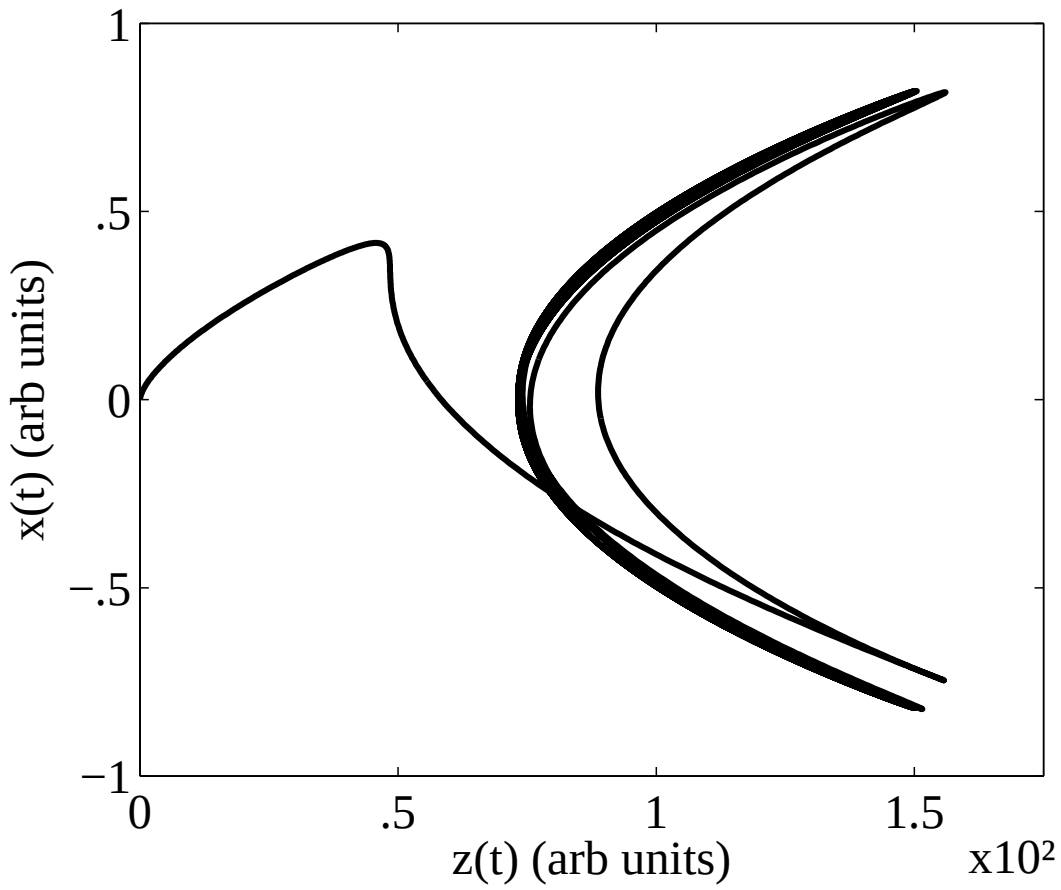

Figure 5.3 Trajectory of electron motion calculated by integration of the equations of motion for an incident electric field of strength $E_0 = 10^8 V/m$. Note the axes differ by only two orders of magnitude. Frequency and linewidth parameters were chosen to be $\omega = 1$, $\omega_x = \omega_y = 1.3$, $\omega_z = 1$, and $\gamma_x = \gamma_y = \gamma_z = 1$.

Remarkably, the exchange of energy that takes place between the electric and magnetic degrees of freedom in the system does not reverse as time progresses, as it does in other coupled oscillator systems. Here, the overall optical interaction at intermediate (sub-relativistic) intensities yields an electric dipole (ED) moment on an ultrafast time scale which is quasistatic and intensity-dependent. The large amplitude of this effect may be ascribed to the doubled frequency of electron motion projected along z [Figs. 5.5,5.10 and 5.13], and to the orthogonality of the electric and magnetic driving fields, which introduces intense parametric enhancement of the magnetic response. Since the dynamics have been shown to obey a complex Mathieu equation in 2.1.7, this result is not too surprising.

The shape of the steady state trajectory is remarkably similar to a hyperbola. It may be the case that for certain choices of parameters, the solution to the equations of motion may

be found exactly in future work if the problem is treated in elliptic coordinates.

Visualization of the temporal dynamics is somewhat easier if the true development of motion along each coordinate is plotted separately. In Figs. 5.4 and 5.5 for example, we can see the rapid onset of steady state motion along x and z. The combined motions in the z direction at frequencies 0 and 2ω are readily apparent in Fig. 5.5.

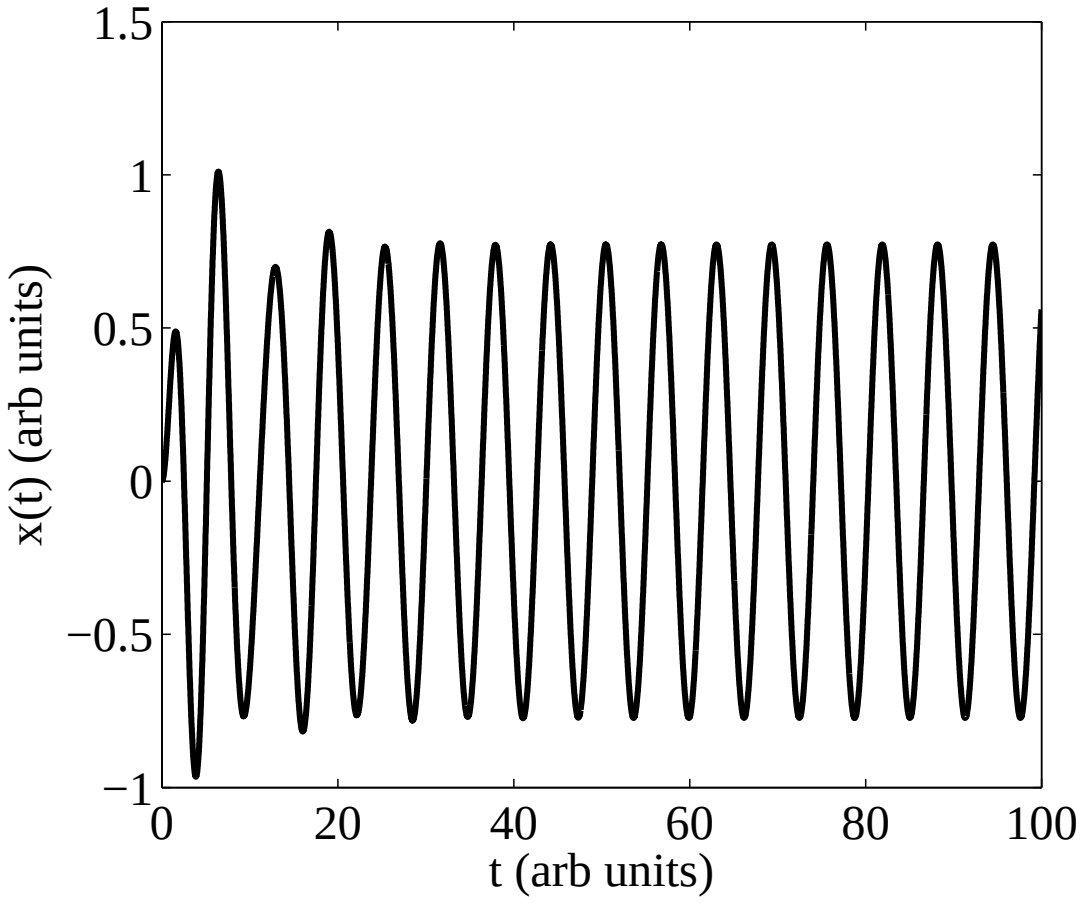

Figure 5.4 x component of electron motion for an incident electric field of strength $E_0 = 10^8 V/m$ and $\tau_{coh} = \text{inf}$. Frequency and linewidth parameters were chosen to be $\omega = 1$, $\omega_x = \omega_y = 1.5$, $\omega_z = 0.2$, and $\gamma_x = \gamma_y = \gamma_z = 0.3$.

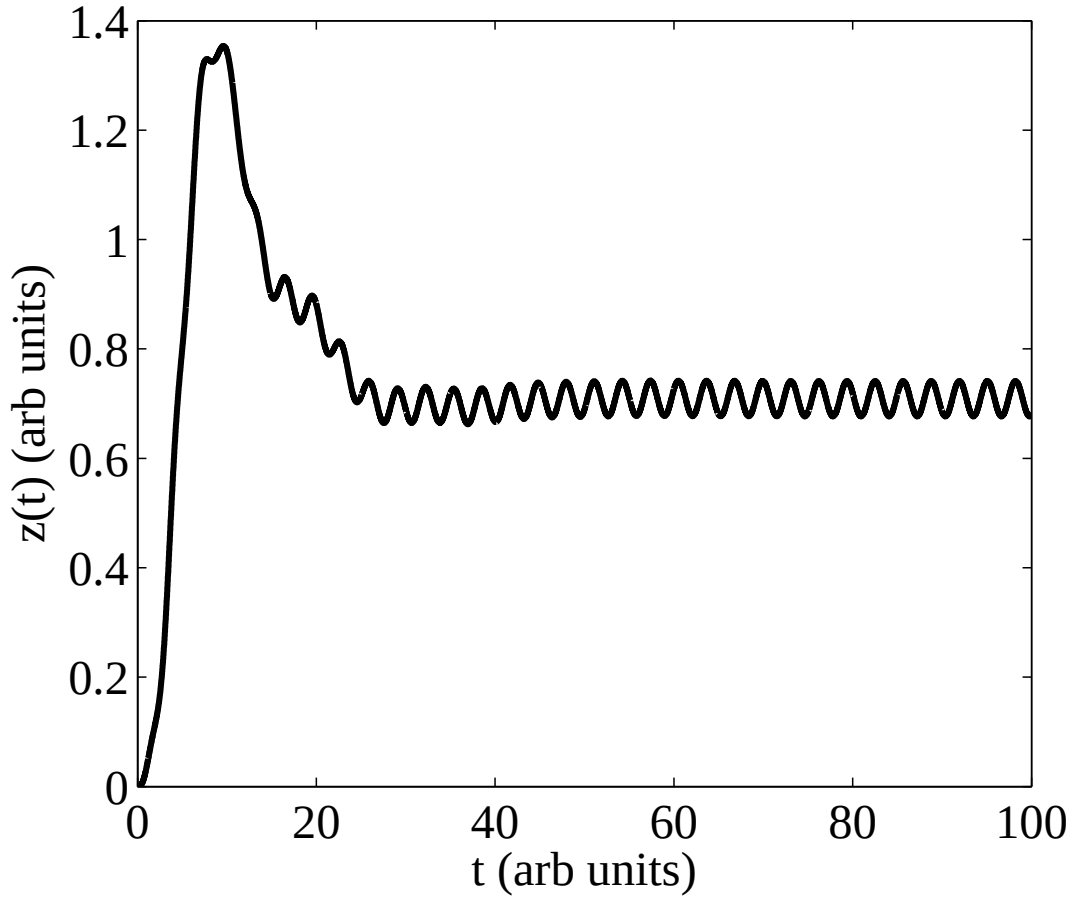

Figure 5.5 z component of electron motion for an incident electric field of strength $E_0 = 10^8 V/m$ and $\tau_{coh} =$ inf. Frequency and linewidth parameters were chosen to be $\omega = 1$, $\omega_x = \omega_y = 1.5$, $\omega_z = 0.2$, and $\gamma_x = \gamma_y = \gamma_z = 0.3$.

The results in Figs. 5.3-5.5 indicate that after a transient of approximately one half dozen cycles of the driving field, the motion reaches steady state. The oscillatory component of motion that persists at long times in Fig. 5.5 is frequency doubled (compare Fig. 5.4). This is therefore the second harmonic generation discussed earlier. The remainder of this section will focus on the DC offset evident in Fig. 5.5 which is the zero frequency term. We can see that the oscillatory motion is no longer about $z = 0$ but instead oscillates about .7 units away from the origin in the positive z direction. This indicates that the electron has pulled away from its nucleus creating a DC polarization in the material. Considering the effect of light on all atoms in the sample volume, as seen in Fig. 5.6, it is clear that a volume polarization density that is steady in time. This looks just like a charged capacitor. With a continuous light source of sufficient intensity, an optically-charged capacitor can be created.

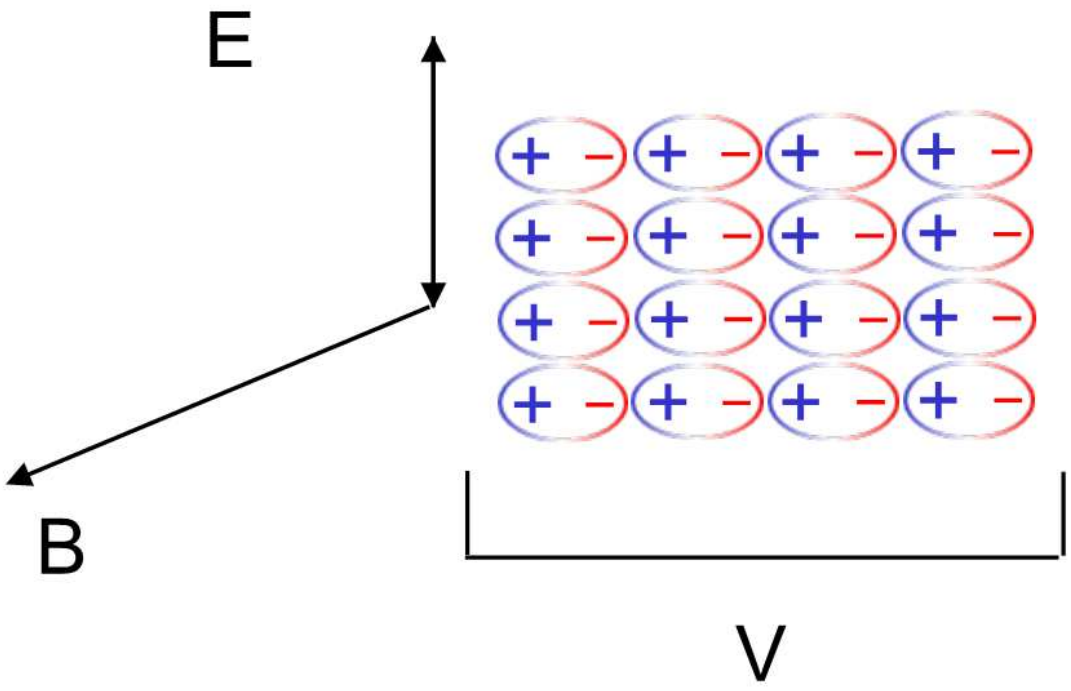

Figure 5.6 As light passes through the sample from left to right, each electron cloud is pulled to the right creating a volume polarization. From end to end this generates a voltage.

The creation of a volume polarization oriented parallel to the direction of propagation of the light can convert light energy directly into charge separation but will be of limited use if it only works for coherent light sources. While it may be possible to beam power across long distances through the use of CW lasers and convert it to electricity with high efficiency, the field of most interest in power conversion is solar power. The conversion of sunlight into a voltage would be of great benefit but would require that nonlinear charge separation to be possible with incoherent light like sunlight. This requirement is examined next by solving the equations of motion with random phase and polarization changes at a fixed time scale.

To follow charge motion driven by a random light field, an Euler integration technique was used [29] employing a constant temporal step size. The stochastic character of sunlight was simulated by changing the phase of the driving fields by an amount in the range $0-2\pi$ at an average rate of τ_{coh}^{-1}. One hundred integration steps were performed per optical cycle. This permitted precise variation and specification of the coherence time. For example, at a wavelength of 800 nm the optical period is 2.6 fs, so a coherence time of 30 fs can be modeled accurately by randomly changing phase at an average rate of once per 1150 steps. The effect of a stochastic driving field with $\tau_{coh} = 30fs$ is presented in Figs. 5.7 and 5.8. When the dephasing time was reduced to 3fs to correspond specifically to radiation from

the sun, the results in Figs. 5.9 and 5.10 were obtained. Note that both Figs. 5.8 and 5.10 exhibit a large, positive offset of the average motion in the direction of propagation, despite dephasing at rates approaching the optical frequency. (Note that the arbitrary unit scales for all plots of the x position and z position of Figs. 5.4 through 5.13 are the same for easy comparison.)

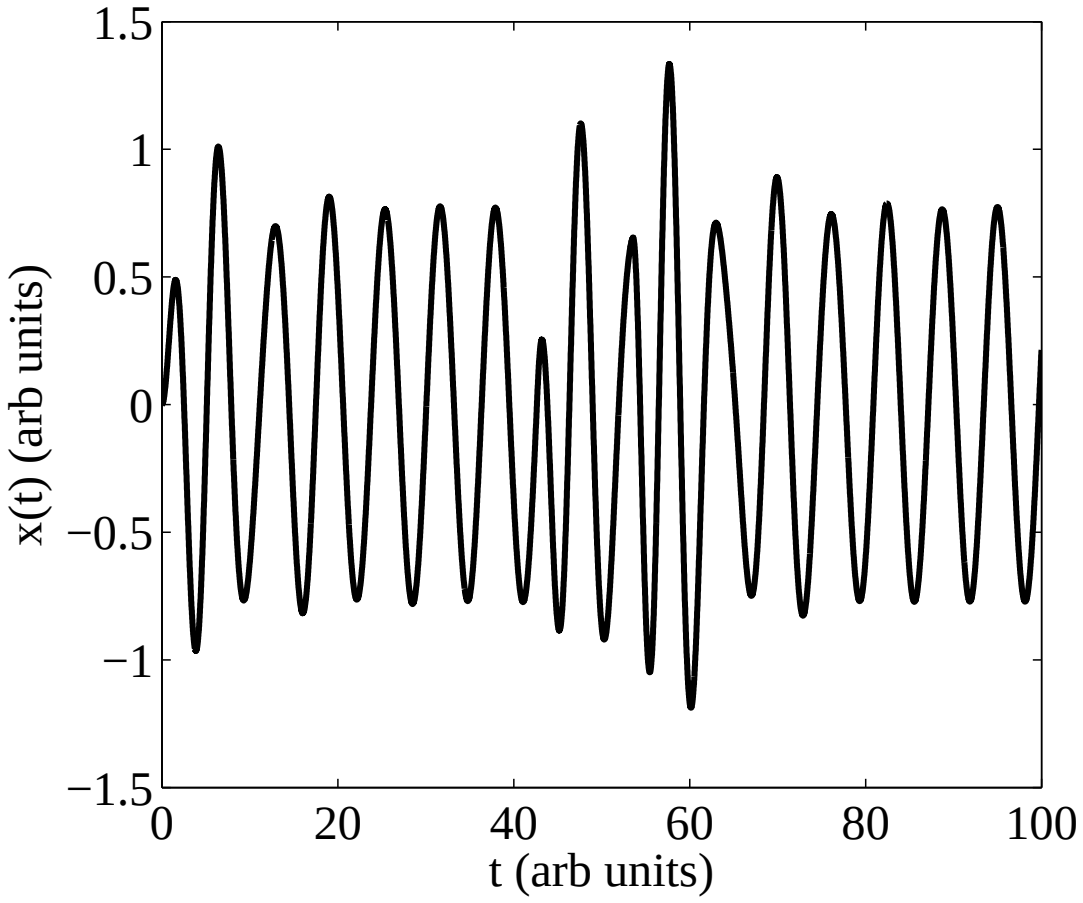

Figure 5.7 x component of electron motion for an incident electric field of strength $E_0 = 10^8 V/m$ and average phase disruption time of $\tau_{coh} = 30fs$. Frequency and linewidth parameters were chosen to be $\omega = 1$, $\omega_x = \omega_y = 1.5$, $\omega_z = 0.2$, and $\gamma_x = \gamma_y = \gamma_z = 0.3$.

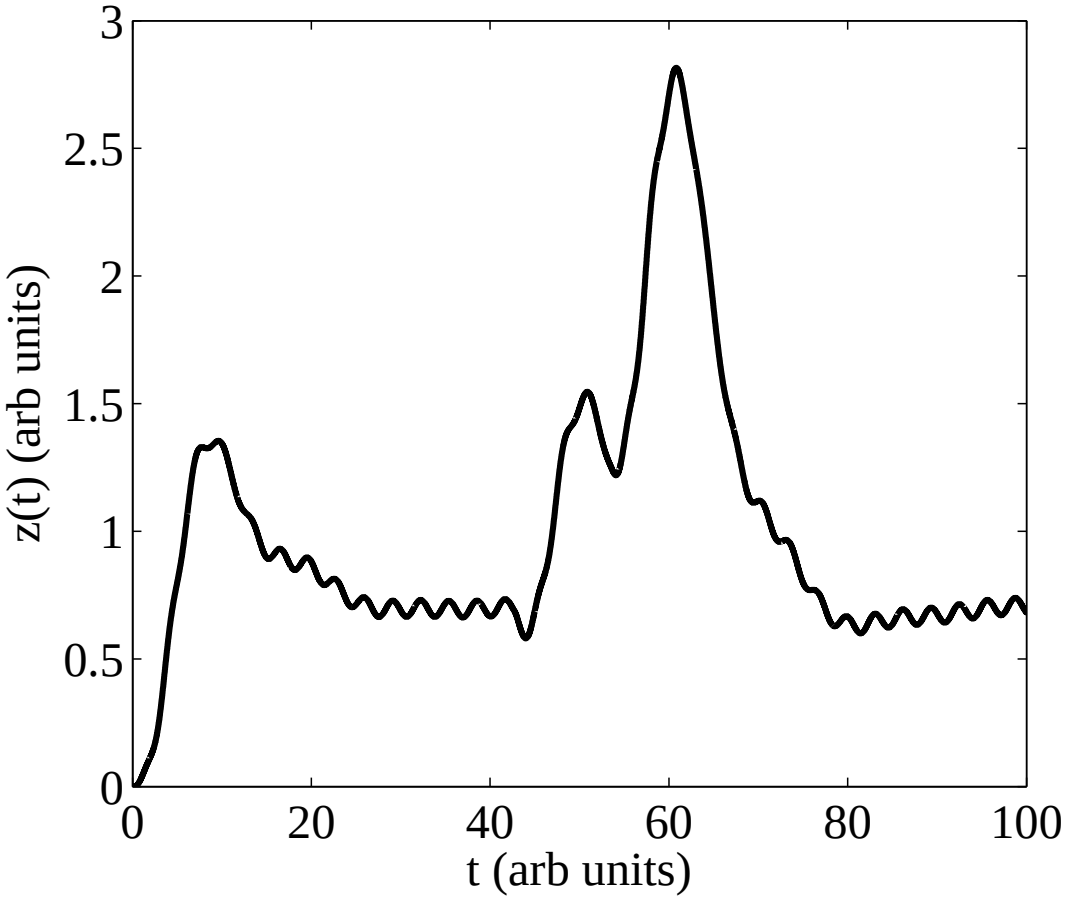

Figure 5.8 z component of electron motion for an incident electric field of strength $E_0 = 10^8 V/m$ and average phase disruption time of $\tau_{coh} = 30fs$. Frequency and linewidth parameters were chosen to be $\omega = 1$, $\omega_x = \omega_y = 1.5$, $\omega_z = 0.2$, and $\gamma_x = \gamma_y = \gamma_z = 0.3$.

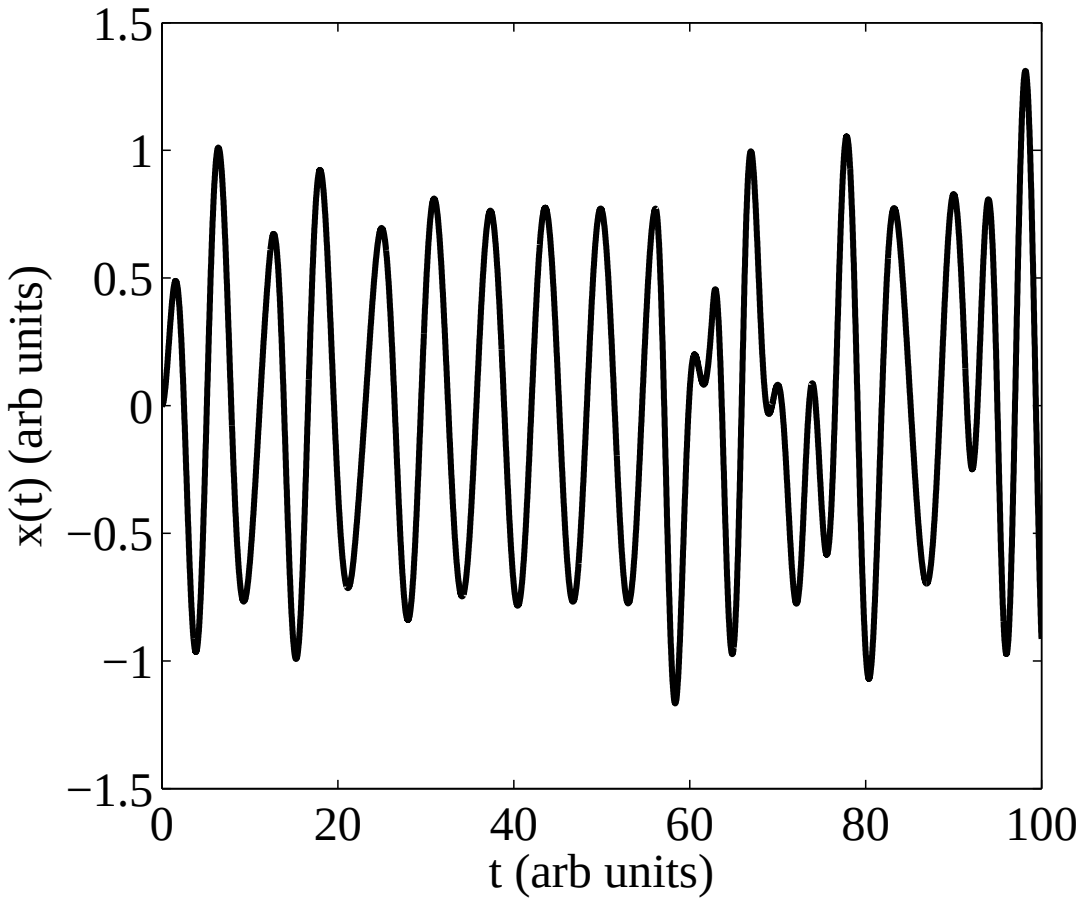

Figure 5.9 x component of electron motion for an incident electric field of strength $E_0 = 10^8 V/m$ and average phase disruption time of $\tau_{coh} = 3fs$. Frequency and linewidth parameters were chosen to be $\omega = 1$, $\omega_x = \omega_y = 1.5$, $\omega_z = 0.2$, and $\gamma_x = \gamma_y = \gamma_z = 0.3$.

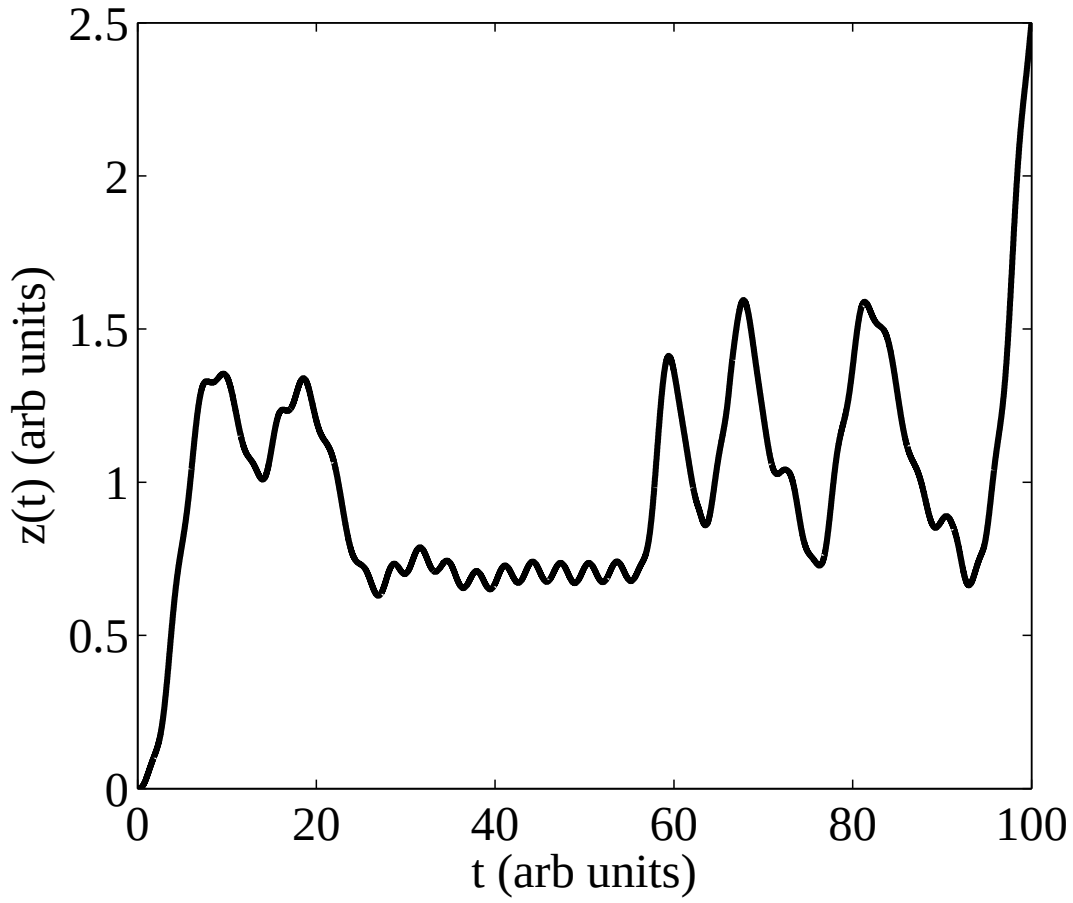

Figure 5.10 z component of electron motion for an incident electric field of strength $E_0 = 10^8 V/m$ and average phase disruption time of $\tau_{coh} = 3fs$. Frequency and linewidth parameters were chosen to be $\omega = 1$, $\omega_x = \omega_y = 1.5$, $\omega_z = 0.2$, and $\gamma_x = \gamma_y = \gamma_z = 0.3$.

Sunlight exhibits rapid, random fluctuations both in phase and polarization. To simulate radiation from this source fully, the procedure described above must therefore be generalized to include stochastic polarization fluctuations. Allowance for random polarizations in the x-y plane necessitates an extension of the calculations above to three dimensions. Consequently in Fig. 5.12 the projection of the electron trajectory along y is presented in addition to the components along x and z.

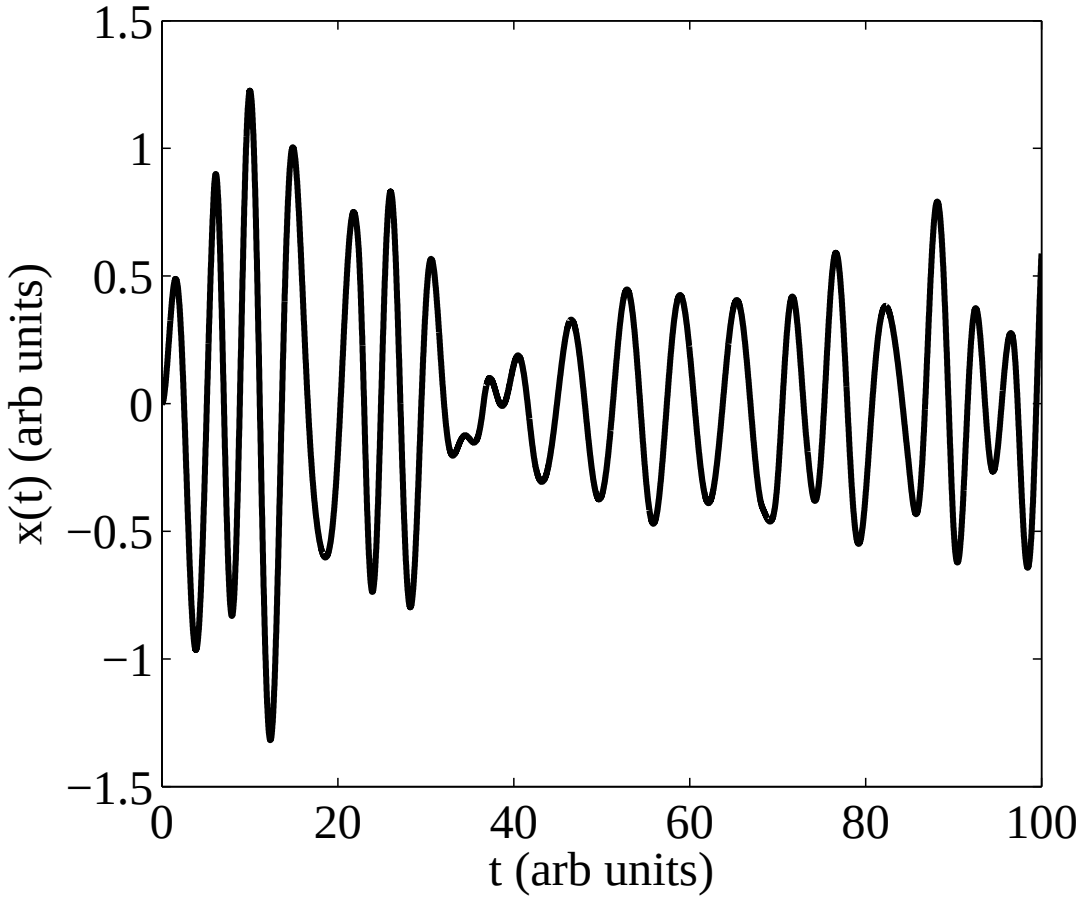

Figure 5.11 x component of electron motion for an incident electric field of strength $E_0 = 10^8 V/m$ and average phase and polarization disruption time of $\tau_{coh} = 3fs$. Frequency and linewidth parameters were chosen to be $\omega = 1$, $\omega_x = \omega_y = 1.5$, $\omega_z = 0.2$, and $\gamma_x = \gamma_y = \gamma_z = 0.3$.

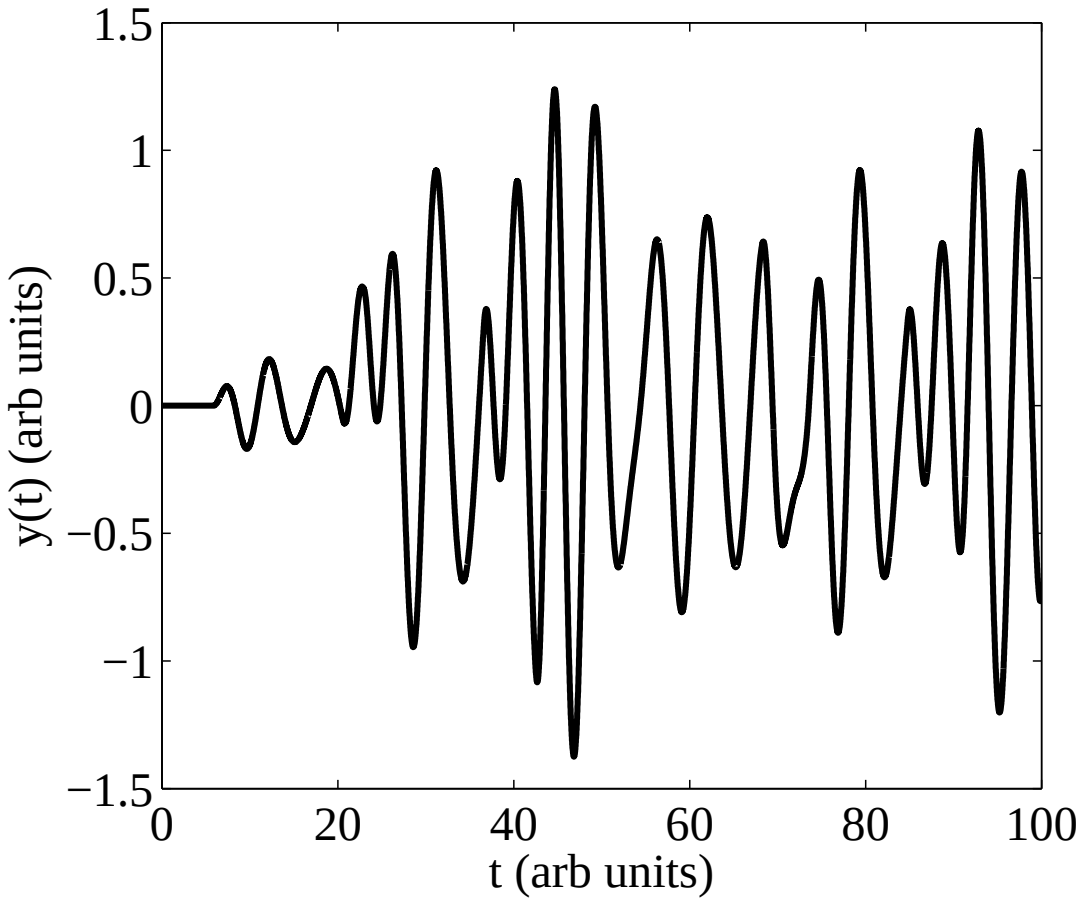

Figure 5.12 y component of electron motion for an incident electric field of strength $E_0 = 10^8 V/m$ and average phase and polarization disruption time of $\tau_{coh} = 3fs$. Frequency and linewidth parameters were chosen to be $\omega = 1$, $\omega_x = \omega_y = 1.5$, $\omega_z = 0.2$, and $\gamma_x = \gamma_y = \gamma_z = 0.3$.

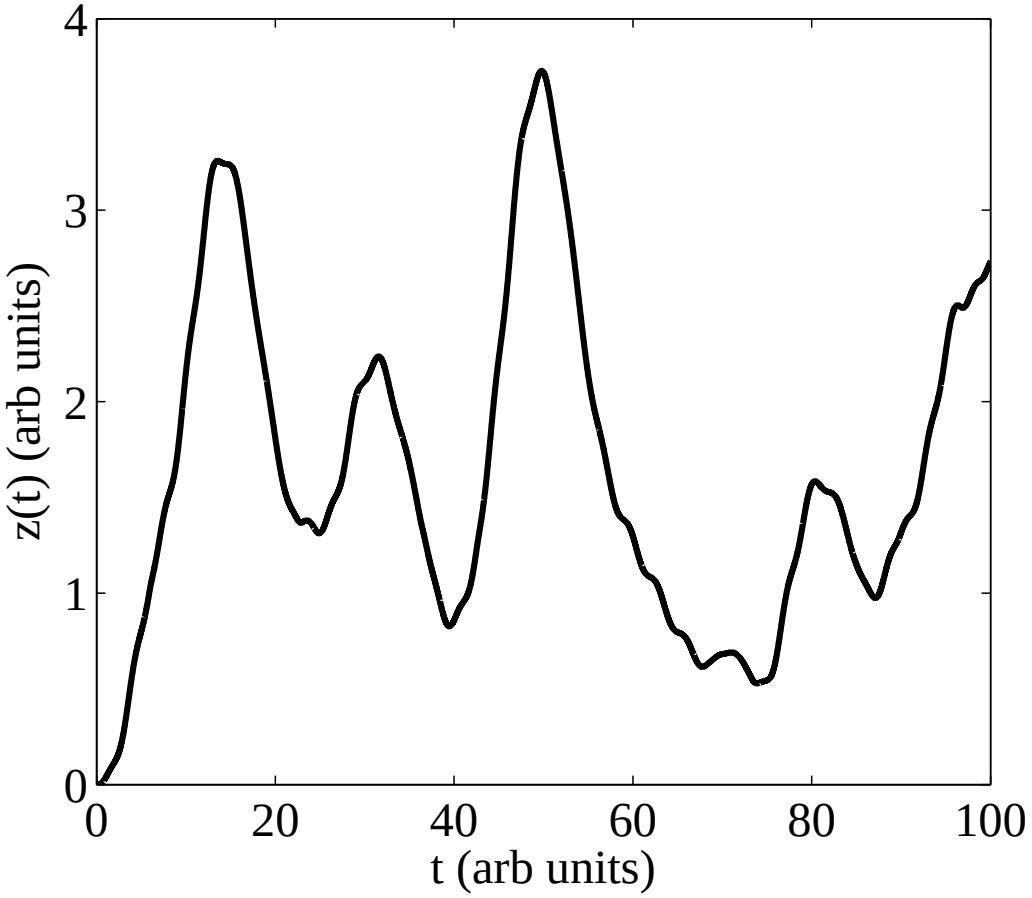

Figure 5.13 z component of electron motion for an incident electric field of strength $E_0 = 10^8 V/m$ and average phase and polarization disruption time of $\tau_{coh} = 3fs$. Frequency and linewidth parameters were chosen to be $\omega = 1$, $\omega_x = \omega_y = 1.5$, $\omega_z = 0.2$, and $\gamma_x = \gamma_y = \gamma_z = 0.3$.

Polarization jumps were assumed to take place at the same time as phase jumps, but were based on a separate random number generator. Figures 5.11 and 5.12 jointly furnish a map of the electron motion in the transverse plane. By comparing similar plots where z is nearly constant, one notices that decreases in the amplitude of motion along x invariably accompany increases in the amplitude along y and vice versa. In Fig. 5.13, the average displacement of the charge along z remains similar to that when phase-only disruptions are taken into account. It should be noted that polarization changes cannot have an effect on the z component of motion. We can see from Eq. 2.51 that the form of the forces due to the external fields is the same regardless of the choice of the polarization direction E_i. Large random excursions and oscillations are evident in Fig. 5.13 but the average offset remains similar to that in Fig. 5.5. The average offset represents the DC voltage available for extraction.

The results above clearly establish that magneto-electric charge separation is feasible with an incoherent source. It is therefore of considerable interest to find out how efficient this process can be. The charge separation described above saturates when the magnetic current density J_M attains its maximum value, namely one half the electric displacement current J_E. (See Section 2.1.3). At higher levels of excitation than this, in the so-called "'magnetic"' saturation regime, the magnetic susceptibility is

$$\chi^{(m)} = -\frac{1}{2}\chi^{(e)} \tag{5.5}$$

and the longitudinal polarization established by it is proportional to the electric field, just like the usual transverse polarization induced by the electric field component of light. As we show next, through the use of Eq. 5.5, predictions can therefore be made of the surface charge density attainable in a plane parallel dielectric slab illuminated uniformly with a specified intensity of coherent light - without knowledge of the linewidth parameters, detunings and transition moments. With this information, the electric energy density that can be stored in a magnetic optical capacitor may be accurately estimated in the undepleted pump limit.

The simplest way to calculate the energy U stored in a magnetic optical capacitor is to imagine a simple parallel plate capacitor formed by a dielectric slab of thickness L and permittivity ε through which the light propagates. Then, as is well-known,

$$U = \frac{1}{2}CV^2 \tag{5.6}$$

where C is the capacitance and V is the voltage that develops across the slab due to irradiation. The displacement charge Q that develops is given by the beam area A times the induced surface charge density σ_s.

$$Q = \sigma_s A \tag{5.7}$$

The magnitude of any surface charge density is the same as the polarization P per unit volume that causes it. Hence, making use of Eq. 5.5 and the standard formula for the capacitance of a dielectric slab, we have

$$V = \frac{Q}{C} = \frac{\sigma_s A}{\varepsilon A/L} = \frac{P^{(m)}L}{\varepsilon} = \frac{-\frac{1}{2}\chi^{(e)}EL}{\varepsilon/\varepsilon_0} = -\frac{(\varepsilon_r - 1)EL}{2\varepsilon_r} \tag{5.8}$$

where we note that in this case the polarization $P^{(m)} = -(1/2)\varepsilon_0\chi^{(e)}E$ is of magneto-electric origin and equals half the usual electric polarization. In 5.8, use has also been made of the relationship $\chi^{(e)} = \varepsilon_r - 1$ between the susceptibility $\chi^{(e)}$ and the relative permitivity $\varepsilon_r = \varepsilon/\varepsilon_0$. Plugging this result back into the equation for stored energy we find

$$U = \frac{1}{2}\frac{\varepsilon_0\varepsilon_r A}{L}\left[\frac{(\varepsilon_r - 1)EL}{2\varepsilon_r}\right]^2 \tag{5.9}$$

In the focal region of a fundamental Gaussian beam of radius ω_0, the relevant area and confocal parameter are given by

$$A = \pi w_0^2 \tag{5.10}$$

$$L_{conf} = \frac{2\pi\sqrt{\varepsilon_r}w_0^2}{\lambda} \tag{5.11}$$

Hence, if we ignore depletion of the optical pump wave, the expression for energy stored in the medium as the result of interacting with a Gaussian beam over the length L_{conf}, is

$$U_{max} = \frac{\varepsilon_0\pi^2 w_0^4}{4\lambda\sqrt{\varepsilon_r}}(\varepsilon_r - 1)^2E^2 \tag{5.12}$$

When the pump wave consists of laser light, the wavelength in Eq. 5.12 is that of the laser and ε_r is the permittivity at the laser wavelength. For solar input, representative values near the peak of the solar spectrum may be assumed. In the latter case it is important to note that the power conversion is operative at all wavelengths in the solar spectrum that fall within the transparency range of the conversion material. Hence, ε_r is determined by the off-resonance susceptibility and the entire spectrum is useful for power conversion.

For efficient optical power generation, the energy storage process that develops charge separation must be repeated as rapidly and as often as possible. Because the rise time of charge separation is faster than $100fs$ (see Figs. 5.5 and 5.10), it is virtually instantaneous compared to attanable extraction rates, Ω^{-1}. Hence power extraction via conducting electrodes applied to the surface of the slab will be chiefly limited by Ω, assuming that

the focused intensity achieves magnetic saturation. Assuming that all the stored energy is extracted during each cycle, the maximum generated power is expressible as

$$P_{max} = \frac{\varepsilon_0 \pi^2 w_0^4}{2\lambda\sqrt{\varepsilon_r}}(\varepsilon_r - 1)^2 \eta_0 \Omega I \tag{5.13}$$

where η_0 is the electromagnetic impedance of vacuum and I is the focused optical intensity.

Estimates of the power levels and efficiencies of a converter based on magnetic charge separation can be made using Eq. 5.13. This equation incorporates the relationship between the length L_{conf} of the region over which focusing of a Gaussian beam can be maintained and the corresponding focal spot size w_0. Hence, it will be applied first to estimate optical-to-electric power conversion of a single mode laser beam, under the assumption that the focused intensity is adequate to saturate the chosen magnetic conversion medium. Then, a simple extension involving guided waves will be applied to remove the constraint between sample length L and spot size. This greatly improves efficiency and makes solar power conversion possible.

To estimate the optical-to-electric power conversion possible with a 1 kW fundamental Gaussian beam switched at a rate of $\Omega = 25MHz$, we consider focusing it to a spot size of $w_0 = 50\mu m$ in a sample of sapphire of length $L_{conf} = 4.45cm$. Taking the relative permittivity and wavelength to be $\varepsilon_r = 3.115$ and $\lambda = 800nm$ respectively, an extracted power of $P_{max} = 1.04W$ is obtained. That is, the conversion efficiency is found to be just $\eta = P_{extr}/P_{in} = 0.104\%$. This estimate and the ones that follow ignore losses from coupling to external circuits with real loads, or to energy storage devices like batteries. This is because electrical coupling losses can be made quite small for capacitive energy sources using energy harvesting circuitry [30]. An example circuit is provided in Fig. 5.14.

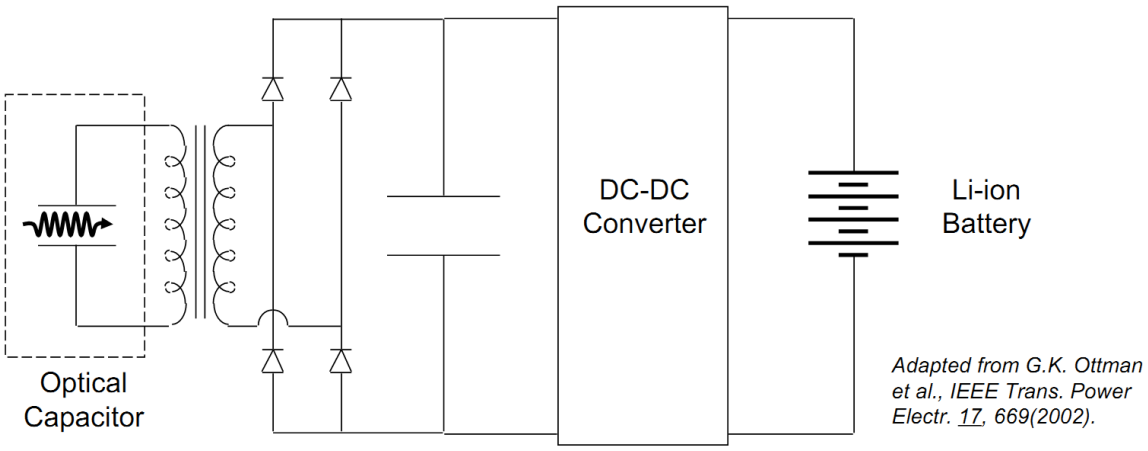

Figure 5.14 Capacitive energy harvesting circuit based on an ac-dc rectifier with an output capacitor, a load, and an adaptive control dc-dc converter that maintains optimal power transfer.

Note that if the light were focused into an optical fiber of length L, it would be confined over lengths much longer than L_{conf}, regardless of spot size. Hence, we next consider a sapphire fiber of length $L = 10m$, removing the constraint between sample length L and w_0 given by Eq.5.11. Single-crystal sapphire fibers have a favorably high index, high thermal conductivity, and can be grown in meter lengths by the laser-heated pedestal growth method [31]. In this situation, the expression for extracted power becomes

$$P_{max} = \frac{\varepsilon_0 \pi w_0^2 L}{4\varepsilon_r}(\varepsilon_r - 1)^2 \eta_0 \Omega I \tag{5.14}$$

For the same input power of $1.0kW$ and a fiber core radius of $w_0 = 50\mu m$, the extracted power is now $0.299kW$ at $\Omega = 25MHz$. Under these conditions, ignoring pump depletion, the theoretical conversion efficiency climbs to $\eta = 30\%$.

On a sunny day at low latitudes, a spherical solar concentrator of diameter $1.0m$ collects power roughly equal to that considered above, namely $1kW$. The concentrator may be assumed to be an f1 optic whose focal length equals its diameter. In practice this will focus sunlight as tightly as is practical. The sun subtends a relatively large angle $\alpha = 4.67mrad$ at earth, so sunbeams are not Gaussian beams. Instead, the focal image size w_0 is a fixed fraction of the radius R of the concentrator: $w_0 = 4.67 \times 10^{-3} R$. For collected powers in the kW range, the focal spot size is therefore much larger than in the earlier estimates for a Gaussian beam source. The available focal spot intensity is limited to approximately $I_{avail} \simeq 1.46 \times 10^7 W/m^2$, which is considerably lower than the intensity required for saturation of the optical magnetization in materials like CCl_4 that have values

of I_{sat} exceeding $10^7 W/cm^2$. Recognizing that the magnetic saturation intensity varies dramatically from one material to another, and that available intensities may be lower than I_{sat}, a formula for the electrical power that can be extracted from a material with given I_{sat} at available light intensities is needed. With these constraints, the magnetic susceptibility is $\chi^{(m)} = -(I_{avail}/I_{sat})^{1/2}(\chi^{(e)}/2)$. Hence, the expression for power output becomes

$$P_{out} = \frac{\varepsilon\pi(\varepsilon_r - 1)^2}{3\varepsilon_r} w_0^2 L \eta_0 \Omega \left(\frac{I_{avail}^2}{I_{sat}} \right) \tag{5.15}$$

The earlier discussion of Figs. (5.7)-(5.13) showed that the charge separation effect of interest here is not significantly reduced by dephasing or depolarization at rates approaching the optical frequency itself. Unlike interactions between linear oscillators, the transfer of energy between the electric and magnetic degrees of freedom of light resists disruption due to the irreversible nature of the cross product in the Lorentz force. Hence coherent light is not needed to drive the magneto-electric power generation described here. Taking this into account and using the expression for P_{out} in Eq. 5.15, the output of a solar converter based on magneto-electric conversion can be accurately predicted. As an example, we consider implementing a generator with a $\phi = 1m$ diameter concentrator, a 1-cm diameter bundle of sapphire fibers each of which has a length $L = 10m$ and external circuitry consisting of several 50/1 step-down transformers and semiconductor rectifiers with reverse breakdown voltage ratings exceeding $V_B \geq 600V$, for power conditioning. According to Eq. 5.8, and assuming $I_{avail}/I_{sat} = 0.1$ in a fiber core with the permittivity of sapphire, the end-to-end voltage generated in each fiber of the bundle is $V = 3.56 \times 10^5 V$. Using a representative wavelength of $0.6\mu m$ for sunlight, and a beam switching rate of $\Omega = 25MHz$ as before, the extractable power is 29.7 W, yielding a theoretical efficiency of nearly 3%.

This scheme for optical power conversion is basically capacitive in nature. Hence, the voltages that develop across the conversion medium approach the megavolt range when the efficiency is pushed to high values, for example by extending fiber length. Although power extraction at high voltages can be handled using transformers and robust electronics [30], the identifiication of materials with lowered intensity requirements will facilitate power generation by lowering the voltage levels that must be handled. Also, non-capacitive schemes may offer alternatives. By using pulsed or chopped input light, alternative implementations of this power generation scheme can be imagined that would exploit the transient, optical magnetization of the medium to produce current flow inductively. By passing the light through an array of conducting split rings whose diameters lie parallel to the propagation axis, single cycle voltage waves would be generated by each pulse passing through the

medium, according to Lenz's Law.

The possibility of efficient solar power generation using Transverse Optical Magnetism depends on finding a suitable conversion material. The properties of the conversion medium must be such as to achieve magnetic saturation at intensities available from sunlight. In the data of Fig. 4.12, some hints have already been seen. Delocalized electronic orbitals in molecules like benzene appear to have promise because benzene was found to be fully saturated at very low intensities ($10^7 W/cm^2$). Through the use of benzene or similar molecules it may be possible to achieve efficient solar power generation using Transverse Optical Magnetism.

Materials suitable for Transverse Optical Magnetic power generation must have properties that are very different from semiconductor solar cells. First, the material needs to be a dielectric. Bound electrons are required to efficiently couple energy from the induced electric dipole into the magnetic response. This can be seen in the structure and solutions of the Complete Lorentz Oscillator Model. With out the binding terms $\omega_i^2 x_i$, the equations of motion no longer have oscillatory solutions and they cannot be written as a Mathieu-like system indicating parametric enhancement. In fact, free charge generation, which is the basis of semiconductor solar power generation, is an energy loss for Transverse Optical Magnetism. If the molecules are ionized by the incident radiation they cannot be used to generate the optical rectification required. In theory, a semiconductor illuminated below the band gap energy would meet this condition, but dielectrics like glass are cheaper and silica has the lowest loss of any material available to manufacture so no advantage is foreseen at this time for semiconductor media.

Conversion material also needs to be transparent to the full solar spectrum. Since any wavelength illuminating the material will generate a rectification term of zero frequency they do not interfere with one another. As long as the illumination at any given wavelength is intense enough, a significant amount of rectification will be generated. This rectification will be added to the rectification generated by the next wavelength and so on. This is a much different case than for semiconductor solar cells in which the band gap defines a very narrow range of wavelengths over which the cell will operate efficiently. Longer wavelengths simple do not generate free charges and thus generate no energy. Shorter wavelengths do generate free charges, but waste energy above the bad gap by generating heat in the bulk. This restriction has resulted in multi-junction solar cells in which several different cells are stacked to cover a broader spectrum of wavelengths. This increases the cost of efficient semiconductor solar cells. In addition, energy conversion based on Transverse Optical Magnetism can, in principle, avoid the necessity of manufacturing complex microscopic structures.

Transverse Optical Magnetism does require high intensity to achieve efficient power conversion however. This is already a drawback since a solar collector is almost certainly required, but it must also be overcome in the conversion medium. The material must be able to withstand very high intensity irradiation for its entire lifetime without suffering significant degredation. Possible sources of damage include ionization by single or multiple photons, thermal stress due to backgorund optical absorption and photochemical degredation, particularly at the surfaces.

Candidate conversion materials must have appropriate point symmetry as previously outlined. We know from Chapter 2 that both an electric and magnetic dipole must be allowed simultaneously for Transverse Optical Magnetism to arise. However, a Heisenberg treatment showed that the optical field generates suitable admixtures of states in any system with centrosymmetry. Additionally, the experiments reported here have shown that molecular liquids in which the molecular point symmetry does not include inversion symmetry also gave intense signals. So the symmetry requirements do not appear to be highly restrictive.

For manufacturing it would be best if the conversion material can be drawn as a fiber. As was discussed above, focusing the light into a fiber extends the region of high intensity over a much longer distance than L_{conf} created by simply focusing the light in the conversion medium. The low cost and high purity of silica fibers should also provide a significant advantage over semiconductor solar cells.

As a complete energy generation system, Transverse Optical Magnetism holds promise. The optical recitifcation process appears to be robust even when coherence times are short. Large area collection optics already exist due to the solar thermal industry. Optical fiber is already produced in large quantities due to the telecommunications industry. The extraction of power from capacitive energy sources is a well studied problem due to energy harvesting research. Hence, the main limitation is the lack of a material that reaches magnetic saturation at concentrated solar intensities.

5.4 Perspectives on Other Fields

In this section we discuss the possible implications of Transverse Optical Magnetism for other fields.

5.4.1 High Field Magnetics

The large magnetic scattering signals presented in Chapter 4 indicate that large magnetic dipoles are induced by the optical fields. Correspondingly enhanced magnetic fields are associated with the interactions described in this thesis. It is of considerable interest to anticipate the magnitude of magnetic fields that can be produced by Transverse Optical Magnetism.

The ratio of magnetic scattering intensity to electric scattering intensity can be as large as $1/4$, based on the experimental results of Chapter 4. This agrees with the theoretical ratio of the power radiated by a magnetic dipole (1.54) and an electric dipole (1.50).

$$R = \frac{MD}{ED} = \left(\frac{m_0}{p_0 c}\right)^2 \leq \frac{1}{4} \tag{5.16}$$

By replacing the moments m_0 and p_0 with their classical expressions $m_0 = \pi r^2 I_0$ and $p_0 = qd$ we can solve for the current necessary to obtain the maximum value of the ratio R:

$$I_0 = \frac{qdc}{2\pi r^2} \tag{5.17}$$

where d is the linear displacement of the electron and r is the radius or the circular component motion of the electron. The magnetic field at the center of a loop of current is given by $B_0 = \frac{\mu_0 I_0}{2r}$ allowing us to solve for the magnetic field associated with maximum magnetic response.

$$\begin{aligned} B_0 &= \frac{\mu_0 qdc}{4\pi r^3} \\ &= 4.5 \times 10^{-18} \frac{d}{r^3} \end{aligned} \tag{5.18}$$

An estimate of the linear displacement, d, for a hydrogen atom can be made by noting that the average radial position of the electron in the first excited state is approximately $10^{-10} m$. The radius of curvature, r, required to generate a magnetic field of one Tesla can then be deduced from Eq. (5.18). Setting $B_0 = 1T$ and $d = 10^{-10} m$ in Eq. (5.18) one finds

$$r \approx 7.7 \times 10^{-10} m \tag{5.19}$$

This is an estimate of the radius of a conventional magnetic moment defined in terms of a closed circular current. Hence this calculation assumed that the magnetic moment m_0 is due to a complete circle of current. However, we have just shown that in fact only a small portion of the circle actually carries current during magneto-electric interactions in bound electron systems since $d < r$ (See for example Fig. 5.3). The fraction of the circle that contains charge is found to be approximately $1/50th$ suggesting that in the experiments discussed in Chapter 4 magnetic fields of the order $1/50$ Tesla were produced. Extrapolating our experimental result from $1/50T$ at $10^8 W/cm^2$ to the white light generation regime at $10^{13} W/cm^2$ we find that it may be possible to generate magnetic fields as high as $10T$ by this means. We conclude from this result that very large magnetic fields may be generated by Transverse Optical Magnetism at even higher intensities of light. In other words, with only the moderate, sub-relativistic, intensities achievable with tabletop lasers, it may be possible to generate magnetic fields comparable to those generated by superconducting magnets.

5.4.2 High Field Laser Physics

The intensity regime in which the results of this dissertation were obtained is sub-relativistic, involving intensities less than $10^{18} W/cm^2$. The majority of research on magnetic effects has been performed, in recent years, at or above the threshold of relativistic optics and current experiments rely on extremely high intensity lasers that reach over $10^{20} W/cm^2$. The results presented here nevertheless have important ramifications for relativistic optical experiments performed in plasmas.

To achieve extreme intensities, very short pulses on the order of ten to one hundred femtoseconds to nanoseconds in duration are used. The generation of these extremely short duration pulses does not produce a single isolated pulse. Commonly, a main pulse is surrounded by a few lower intensity pulses and the whole train of pulses rides on top of a longer duration envelope of much lower intensity as shown in Fig. 5.15.

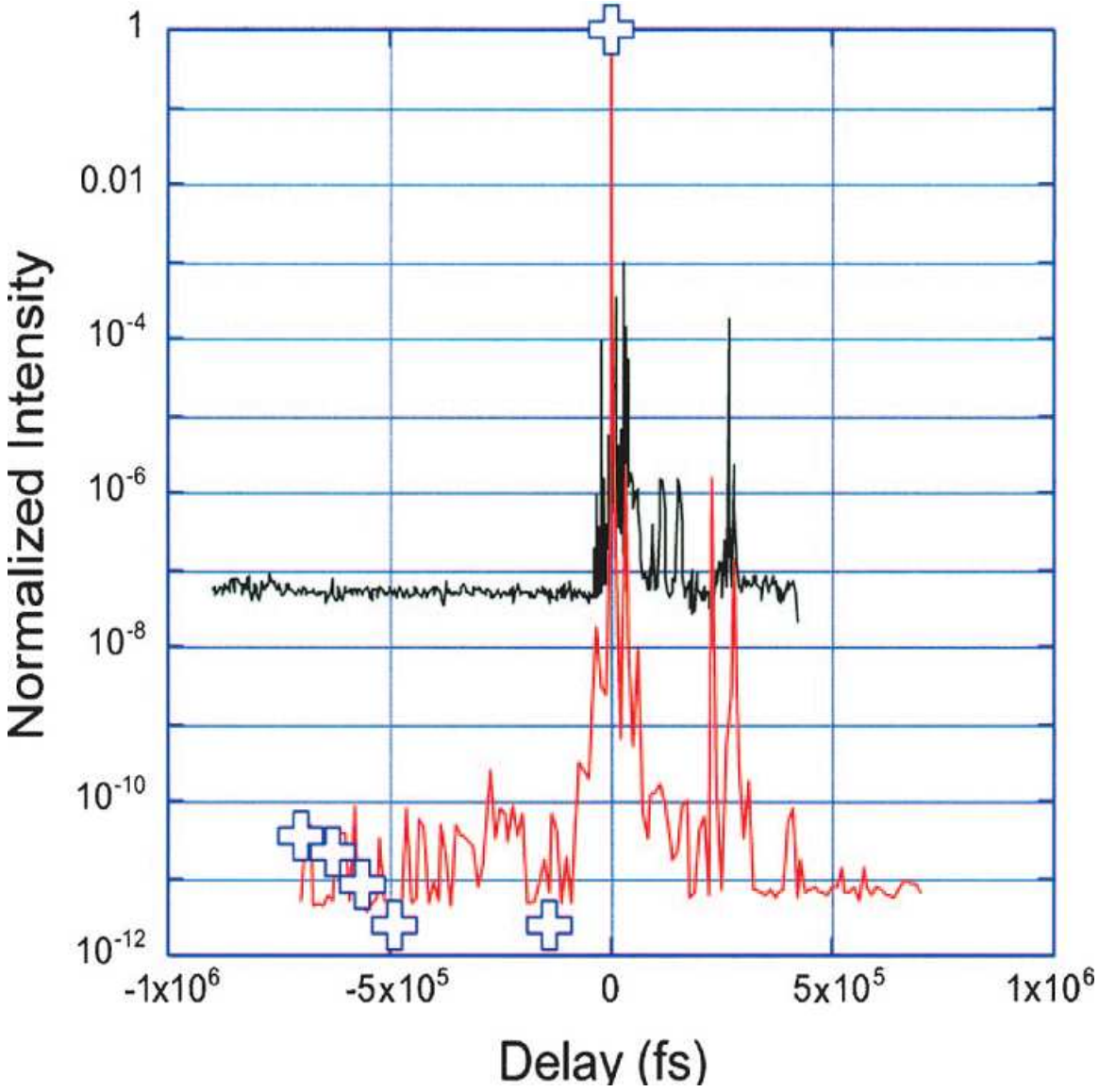

Figure 5.15 Autocorrelator trace of pulse output from Hercules laser. Black is the standard output of the petawatt stage, red is the high constrast mode. All data is normalized to the highest peak of the trace. We see both pre and post-pulses as well as a background intensity. In standard mode the pre pulse is four orders of magnitude smaller than the main pulse or still $10^{16}W/cm^2$. Even the long duration envelope is $10^{13}W/cm^2$, well into the saturation regime of Transverse Optical Magnetism reported in this thesis.

It is already well known that prepulses dramatically influence the generation of protons and ions in laser acceleration applications [32]. The intensities reached by the prepulses in these experiments are well above the saturation regime for Transverse Optical Magnetism in the studied materials. The intitial conditions of the material when the high intensity pulse arives are certainly determined by the prepulses. Even if the electric effects of the prepulse are

incorporated into models they may be missing magnetic effects that are generated at this sub-relativistic intensity.

5.4.3 Solar Power

Based on the earlier discussions, the use of optical rectification by Transverse Optical Magnetism may influence the solar power industry in the future. While the predicted efficiency of conversion is only comparable to the current state of the art in multi-junction semiconductor solar cells, the manufacturing, maintenance, and weight of Transverse Optical Magnetism based systems could be dramatically different. Using pulled optical fiber instead of large area semiconductor solar cells will change manufacturing from single crystal growth and layering to pulled fiber. Packaging changes from large area arrays to smaller fiber coils under an array of solar collectors. Maintenance and reliability of semiconductor solar cells of comes down to maintaining all of the electrical connections between the thousands of cells in a large array. Transverse Optical Magnetic fiber arrays require only two connections per array, front and back contact, and possibly zero if inductive methods are developed. Finally, using a large foil solar collector focused onto a length of optical fiber would weigh much less than a full array of standard semiconductor solar cells. If the efficiency and power output are even comparable to semiconductor solar cells, a significant weight savings is of prime interest to the space power industry. So any reduction in launched weight would translate into a massive cost savings per kilogram.

5.5 Future Work

This dissertation has presented only the initial measurements, theory, and predictions of Transverse Optical Magnetism. To conclude, suggestions for future work are made here.

In order to understand the energy transfer mechanism between electric and magnetic response the resonances in the classical model should be studied in more detail. The form of the equations of motion that seems to be of particular interest is the matrix equation 2.99. While systems of coupled Mathieu equations have been studied in the past, none has been studied in which the coupling was sinusoidal in time. The case of constant coupling has been studied for decades beginning with Bolotin and Hsu [33] [34]. The case of time periodic damping coefficients have also been studied although only as a one dimensional problem [35]. The combination and extension of these two methods may yield a better understanding of parametric resonances and energy transfer processes.

Further measurements of dipole scattering in different materials are needed to both test the quantum mechanical predictions and search for a material to use in solar power or terahertz generation. A significant hurdle to power conversion applications is that the DC voltage induced by optical rectification needs to be measured directly. The most straightforward method will be to apply transparent contacts to a dielectric material and measure the voltage developed across the material. This could be done by using a modulated laser source and measuring the induced voltage across the material with a lock-in amplifier. It may be a challenge to develop transparent contacts that can withstand the intensities needed for efficient Transverse Optical Magnetic materials however. It may also be possible to measure an induced voltage in a ring conductor placed near the pulsed laser beam as described in the previous section.

Terahertz radiation should be sought in unbiased dielectric materials rather than nonlinear optical crystals. Generation of terahertz radiation in a centrosymmetric material would be a new effect entirely. To increase efficiency of generation and detection it may be necessary to use tilted-front excitation in which the pump laser pulse is tilted to the angle that matches the Cherenkov angle, thus creating a self-reinforcing wavefront of terahertz raditation in the material [36]. By cutting the exit face of the material to match the Cherenkov angle as well, a fully formed beam of terahertz radiation should emerge for detection.

The capacitive energy harvesting circuit described in the previous section needs to be constructed and applied to the opto-magnetically induced voltage. Initial experiments should seek to harvest energy from a laser beam. The fully coherent source with very high intensities will make testing the circuitry and design much simpler. Once progress has been made the system can be coupled to a solar collector and used to generate power from an incoherent source.

Appendices

Appendix A

4-vector Formalism for Transverse Optical Magnetism

Examining Eq. 2.4 we see that the distinction between magnetization M and dynamic polarization P is subtle at best. For a complicated, time-dependent currents it is often unclear how to divide the problem into magnetic and electric sources. In reality, polarization and magnetization are components of a higher order tensor of material response. Just as an electric field can look like a magnetic field in a certain frame of reference, a polarization can look like a magnetization. The theory of Transverse Optical Magnetism may be simplified by using a more general form of material response and electromagnetic fields.

The most general way to represent classical electromagnetics is to use the 4-vector formalism typically reserved for relativistic electrodynamics. In this notation the electric and magnetic fields are simply two parts of the same higher order field. This Maxwell field tensor is written

$$F^{\mu\nu} = \begin{pmatrix} 0 & -E_x/c & -E_y/c & -E_z/c \\ E_x/c & 0 & -B_z & B_y \\ E_y/c & B_z & 0 & -B_x \\ E_z/c & -B_y & B_x & 0 \end{pmatrix} \tag{A.1}$$

and its dual

$$\mathscr{F}^{\mu\nu} = \frac{1}{2}\varepsilon^{\mu\nu\gamma\delta}F_{\gamma\delta} \begin{pmatrix} 0 & -B_x & -B_y & -B_z \\ B_x & 0 & E_z/c & -E_y/c \\ B_y & -E_z/c & 0 & E_x/c \\ B_z & E_y/c & -E_x/c & 0 \end{pmatrix} \tag{A.2}$$

Likewise, the induced polarization and magnetization can be written in 4-tensor form

$$M^{\mu\nu} = \begin{pmatrix} 0 & -cP_x & -cP_y & -cP_z \\ cP_x & 0 & M_z & -M_y \\ cP_y & -M_z & 0 & M_x \\ cP_z & M_y & -M_x & 0 \end{pmatrix} \tag{A.3}$$

and its dual

$$\mathscr{M}^{\mu\nu} = \frac{1}{2}\varepsilon^{\mu\nu\gamma\delta} M_{\gamma\delta} \begin{pmatrix} 0 & M_x & M_y & M_z \\ -M_x & 0 & cP_z & -cP_y \\ -M_y & -cP_z & 0 & cP_x \\ -M_z & cP_y & -cP_x & 0 \end{pmatrix} \tag{A.4}$$

indicating that the polarization and magnetization are two parts of the same higher order field [37]. Note the sign changes between $F^{\mu\nu}$ and $M^{\mu\nu}$. This comes from the minus sign in the relationship between magnetic field and magnetization

$$\vec{H} = \frac{1}{\mu_0} < \vec{B} > -\vec{M} \tag{A.5}$$

where brackets indicate a microscopically large volume average. The other quantities of the dynamics must also be written in 4-vector form, the most important being the 4-velocity $U_\nu = \gamma(c, \vec{v})$.

This notation allows for a fully generalized constituitive relation to be developed between all four fields. By contracting the field tensors with the 4-velocity we can find the covariant generalizations of the fields.

$$M^{\mu\nu}U_\nu = \gamma c^2 \left(\frac{\vec{v}\cdot\vec{P}}{c}, \vec{P} - \frac{\vec{v}\times\vec{M}}{c^2} \right) \tag{A.6}$$

$$F^{\mu\nu}U_\nu = \gamma \left(\frac{\vec{v}\cdot\vec{E}}{c}, \vec{E} + \vec{v}\times\vec{B} \right) \tag{A.7}$$

In each case, as the velocity approaches zero, i.e. we enter the rest frame, the result reduces to the typical 3-fields $\vec{P}$ and $\vec{E}$ respectively. This implies that we can write a fully covariant form of the typical linear constituitive relations

$$\vec{P} = \varepsilon_0 \chi_e \vec{E} \tag{A.8}$$

$$\vec{M} = \chi_m \vec{H} = \frac{\chi_m}{\mu_0(1+\chi_m)} \vec{B} \tag{A.9}$$

in the rest frame. Begining with the electric relation

$$M^{\mu\nu} U_\nu = \frac{\chi_e}{\mu_0} F^{\mu\nu} U_\nu \tag{A.10}$$

which, written in 3-vector form is

$$\vec{v} \cdot \vec{P} = \varepsilon_0 \chi_e \vec{v} \cdot \vec{E} \tag{A.11}$$

$$\vec{P} - \frac{\vec{v} \times \vec{M}}{c^2} = \varepsilon_0 \chi_e (\vec{E} + \vec{v} \times \vec{B}) \tag{A.12}$$

The first relation, the time-like component, is actually redundant (dot both sides with $\vec{v}$), so only the second relation, the space-like component is required. We can see that even for a linear relationship between $\vec{P}$ and $\vec{E}$ some magnetization is mixed in. A similar result comes from the linear magnetic relation

$$\vec{v} \cdot \vec{M} = \frac{\chi_m}{\mu_0(1+\chi_m)} \vec{v} \cdot \vec{B} \tag{A.13}$$

$$\vec{M} + \vec{v} \times \vec{P} = \frac{\chi_m}{\mu_0(1+\chi_m)} \left(\vec{B} - \frac{\vec{v} \times \vec{E}}{c^2} \right) \tag{A.14}$$

Just like the typical, non-relativistic, 3-vector form of electromagnetism, generalizations to anisotropic media and nonlinear processes are possible. Transverse Optical Magnetism, being a second order process, would require the application of two covariant fields. It can also take place in an anisotropic medium so we expect to need a susceptibility tensor $\chi_{\mu\nu\gamma}$. A combination of field tensors equivalent to an EB interaction would be

$$P_\mu = \chi_{\mu\nu\gamma} E^\nu B^\gamma = M^{\mu\nu} U_\nu = \chi_{\mu\nu\gamma} F^{\nu\delta} U_\delta \mathscr{F}^{\gamma\eta} U_\eta \tag{A.15}$$

This method of keeping electric and magnetic effects mixed at all orders may prove useful.

Keeping the electromagnetic fields combined along with the material responses does not allow any confusion about the type of source currents because in the most general case there is no distiction. Polarization and magnetization are two components of the same field tensor.

Appendix B

Graphic Approach to Solving the Complete Lorentz Oscillator Model

The dimensionless equations of motion of the Complete Lorentz Oscillator Model

$$\frac{d^2x}{dt^2} + \gamma_x \frac{dx}{dt} + \omega_x^2 x = \cos(t) - f_c \cos(t) \frac{dz}{dt} \tag{B.1}$$

$$\frac{d^2z}{dt^2} + \gamma_z \frac{dz}{dt} + \omega_z^2 z = f_c \cos(t) \frac{dx}{dt} \tag{B.2}$$

have solutions that follow a regular pattern. Hence, a diagrammatic approach is useful. It is possible to find a solution, to any order, by observing the following rules:

Notation: The order of the term is denoted by m and frequency is denoted by n. Solutions at odd orders are in the x direction and solutions of even order are in the z direction. The subscript i follows this rule; it equals x if m is odd and z if m is even.

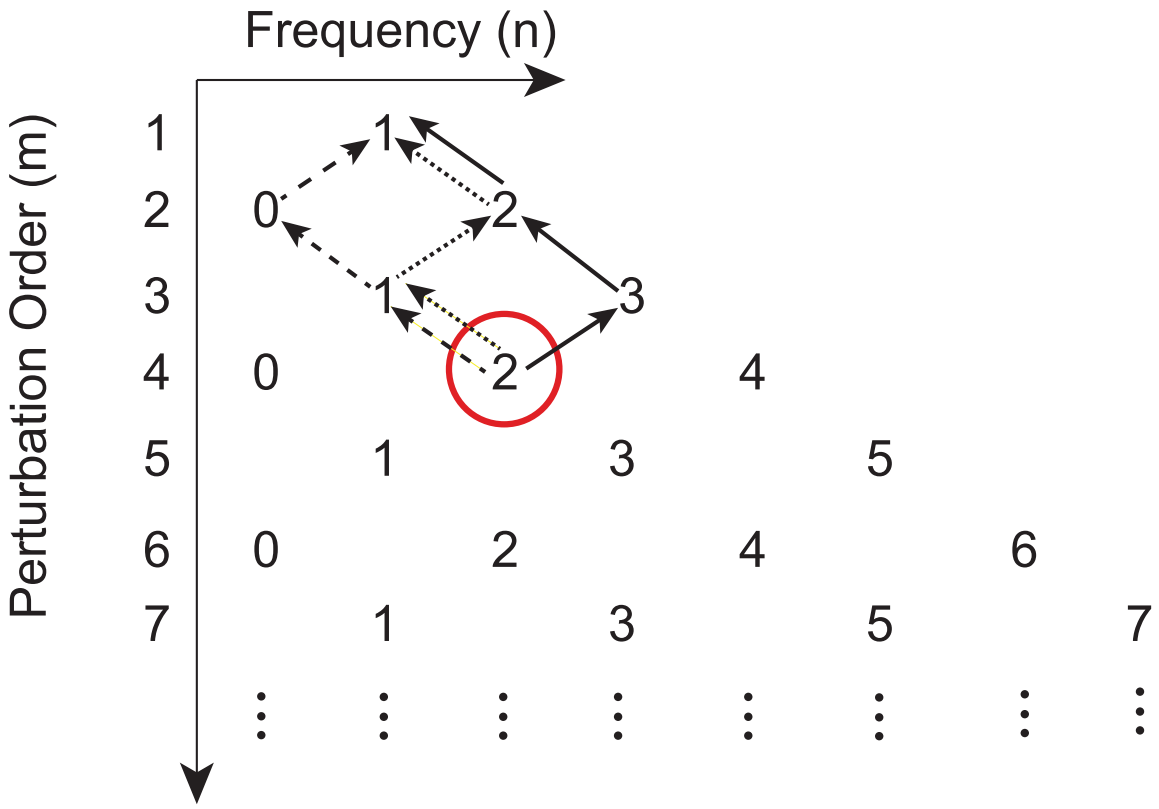

Figure B.1 Diagram of solutions to the dimensionless equations of motion. Can be extended vertically to arbitrary order following the same pattern.

Method: Select the term on the diagram that you wish to calculate. Trace a path back to the first order term always moving up one order and one frequency left or right on the diagram. All paths need to be calculated and added together to find the full solution for any term.

1: $\left(-\frac{f_c}{2}\right)^{(m-1)}$

2: Multiply by all previous numbers on the path back to first order

3: The time dependence is

$$\begin{array}{ll} \cos(nt+\phi\ldots) & \text{if } m \text{ is odd} \\ -\sin(nt+\phi\ldots) & \text{if } m \text{ is even} \end{array}$$

4: Multiply by the product of all A_n on path back to first order

$$A_n = \frac{1}{\sqrt{(\omega_i^2 - n^2)^2 + n^2\gamma_i^2}} \tag{B.3}$$

5: The phase shift $\phi\ldots$ in the time dependence is given by the sum of all ϕ_n for each number on the path

$$\phi_n = \tan^{-1}\left(\frac{-n\gamma_i}{\omega_i^2 - n^2}\right) \tag{B.4}$$

6: Repeat previous steps for each possible path back to first order and add them together

AS a specific example of this procedure, consider the frequency doubled term of 4th order. There are three possible paths: $2 \to 3 \to 2 \to 1$, $2 \to 1 \to 2 \to 1$, and $2 \to 1 \to 0 \to 1$. The solution for the first path, corresponding to the solid arrows in Fig. B.1, would be

$$\left(\frac{f_c^3}{8}\right)(3)(2)(1)A_3A_2^2A_1\sin\left(2t+\phi_3+2\phi_2+\phi_1\right) \tag{B.5}$$

By repeating this process for the large dash and small dash paths of Fig. B.1 and adding those solutions to that of B.5 the complete solution for frequency doubling at 4th order may be obtained.

Appendix C

Irreducible Representations of Electric and Magnetic Moments

Electric and magnetic dipole moments are polar and axial vectors respectively. Hence, their irreducible representations are rank 1 spherical tensors that transform like a normal vector and a cross product of vectors.

The electric dopole moment, being a normal vector, is written:

$$\vec{\mu}^{(e)} = e(x\hat{x} + y\hat{y} + z\hat{z}) \tag{C.1}$$

$$= e(r\sin\theta\cos\phi\hat{x} + r\sin\theta\sin\phi\hat{y} + r\cos\theta\hat{z}) \tag{C.2}$$

$$= -er\sqrt{\frac{4\pi}{3}}\left(Y_{1-1}\hat{\varepsilon}_+ + Y_{11}\hat{\varepsilon}_- + Y_{10}\hat{\varepsilon}_0\right) \tag{C.3}$$

$$= -\mu_-^{(e)}\hat{\varepsilon}_+ - \mu_+^{(e)}\hat{\varepsilon}_- + \mu_0^{(e)}\hat{\varepsilon}_0 \tag{C.4}$$

where θ is the polar angle and ϕ is the equatorial angle.

For the magnetic moment, consider an axial vector composed of vectors $\vec{A}$ and $\vec{B}$ according to

$$\vec{V} = \vec{A} \times \vec{B} \tag{C.5}$$

where

$$A_x = -\frac{A_1 - A_{-1}}{\sqrt{2}} \quad B_x = -\frac{B_1 - B_{-1}}{\sqrt{2}} \tag{C.6}$$

$$A_y = i\frac{A_1 + A_{-1}}{\sqrt{2}} \quad B_y = i\frac{B_1 + B_{-1}}{\sqrt{2}} \tag{C.7}$$

$$A_z = A_0 \qquad B_z = B_0 \tag{C.8}$$

then we find

$$\vec{V} = i(A_1B_0 - A_0B_1)\hat{\varepsilon}_- + i(A_0B_{-1} - A_{-1}B_0)\hat{\varepsilon}_+ + i(A_{-1}B_1 - A_1B_{-1})\hat{\varepsilon}_0 \tag{C.9}$$

Noticing that the pairs of components form a pattern we define $C_\pm \equiv A_\pm B_0$, $D_\pm \equiv A_0 B_\pm$, and $F_\pm \equiv A_\mp B_\pm$ allowing the simplification:

$$\vec{V} = -i(C_- - D_-)\hat{\varepsilon}_+ + i(C_+ - D_+)\hat{\varepsilon}_- + i(F_+ - F_-)\hat{\varepsilon}_0 \tag{C.10}$$

where we are now able to identify tensor components of the magnetic moment as

$$\mu_\pm^{(m)} \equiv (C_\pm - D_\pm) \tag{C.11}$$

$$\mu_0^{(m)} \equiv (F_+ - F_-) \tag{C.12}$$

Hence, the general form of the moment is

$$\vec{\mu}^{(m)} = i\mu_+^{(m)}\hat{\varepsilon}_- - i\mu_-^{(m)}\hat{\varepsilon}_+ + i\mu_0^{(m)}\hat{\varepsilon}_0 \tag{C.13}$$

One further result to note is that

$$F_+^* \equiv A_{-1}^* B_1^* \tag{C.14}$$

$$= (-)^2 A_1 B_{-1} = F_- \tag{C.15}$$

Appendix D
Ultrafast Depolarization Observations

During data collection for the experiments of Section 4.1.3 an unexplained effect was observed at very high powers. It is described here to motivate future experiments designed to provide some understanding of its origin.

Following the methods of Chapter 3 an amplified light beam was passed through a liquid sample of CCl_4 and the scattered light collected and detected by photomultiplier tube. The standard procedure to map the radiation pattern was implemented by rotating the input polarization while leaving the analyzing polarizer in either the vertical (electric dipole) or horizontal (magnetic dipole) orientation. In addition however, the input polarization was held fixed and the analyzing polarizer was rotated with the expectation of recording a similar dipole pattern. It was found that for small diameter beams and low powers similar dipole patterns were recorded. However, for larger diameter beams and higher than usual powers the results changed. The input polarization was held fixed in the horizontal (magnetic dipole) orientation and the analyzing polarizer rotated through 360 degrees in 10 degree increments to record the data of interest here, shown in Fig. D.1.

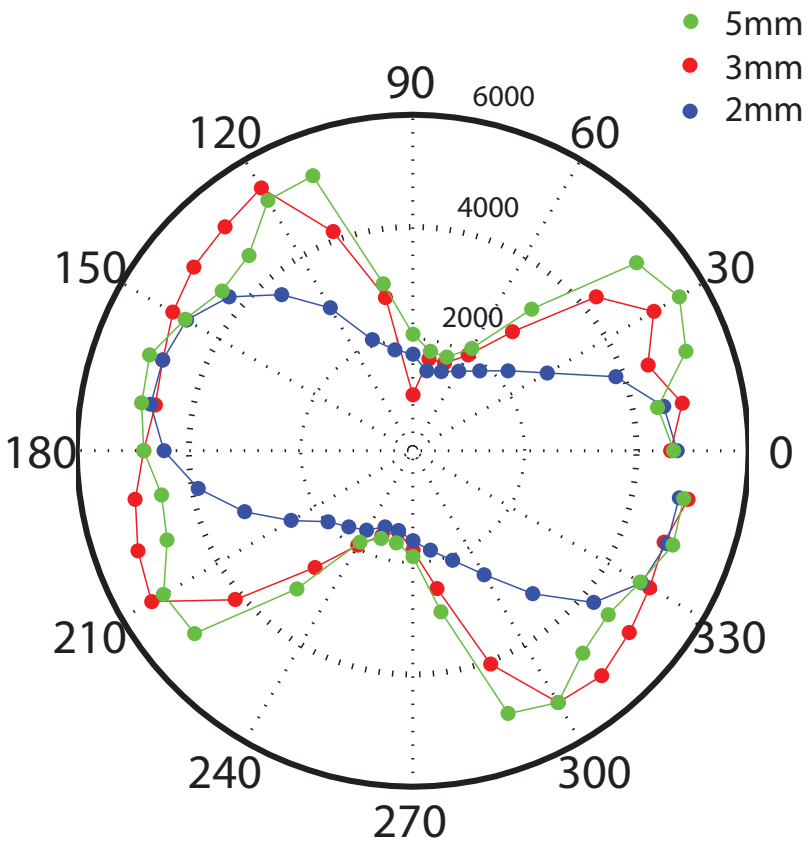

Figure D.1 Polarization states of light scattered from CCl_4 by the magnetic dipole due to different beam widths.

An offset of approximately 15 degrees of the dipole maxima from 0 degrees is shown in the figure. This feature of the plot is not of interest since it was an experimental artifact that can be ignored.

The radiation patterns of Fig. D.1 do contain other non-dipole features. First, the pattern never shows zero signal at any analyzer orientation. This implies that the time-averaged signal is partially depolarized [38]. Second, there is a beam width dependent polarization pattern superposed on top of the depolarized signal and the dipole contibution. This gave the pattern X-like shape that extends beyond the basic dipole pattern seen in blue in Fig. D.1. The beam width dependence manifested itself as the expansion of the X-like pattern to wider angles at large widths. While no X-like pattern can be seen in the 2mm signal, an X with approximately 90 degrees between the arms can be seen for the 3mm beam, and an X of 110 degrees for the 5mm beam.

An initial conjecture about the origin of the polarization X pattern was dynamic Faraday

rotation. The static Faraday effect was derived in Chapter 1 and the susceptibility tensor was found in Eq. 1.32. This effect arises when a magnetic field is applied along the direction of propagation of light causing the material to become optically active. The result is a rotation of the linear polarization state of the light. The amount of rotation is determined by the formula

$$\beta = \mathscr{V} B d \tag{D.1}$$

where B is the applied static magnetic field flux density. β is the angle that the polarization has rotated from its initial orientation, $\mathscr{V}$ is the Verdet constant, and d is the distance the light has travelled in the interaction region. A generalization of this rotation effect to time dependent magnetic field might be expected to rotate the polarization one way when the magnetic field is positive and the opposite way when the magnetic field is negative. If this oscillating polarization were to be measured as a time-average, the turning points of the motion would yield the largest signal, resulting in an X-like pattern.

This conjecture was tested by using a phase stable interferometer to perform a pump probe experiment. This work was done in the laboratory of Prof. Dantus at Michigan State to exploit the dispersion compensation available through the use of Multiphoton Intrapulse Interference Phase Scan (MIIPS). This system provided us with two beams of pulses of $< 10 fs$, one of vertical polarization and one of horizontal polarization. The timing between the two pulses was controllable with femtosecond accuracy using the MIIPS technique. A perpendicular geometry was chosen for the pump-probe experiment to imitate the geometry of the scattered light experiment. By varying the delay between the pump and probe pulses it was hoped that a time dependence of the polarization pattern in Fig. D.1 would be found. Unfortunately, no such modification of the probe beam was observed and no insight was provided on this strange effect.

Appendix E

Coupled Mode Analysis of Lorentz Force Coupling

To examine the efficiency of nonlinear processes it is often necessary to perform a coupled mode calculation. Here we attempt to extend the theory of coupled modes to include Transverse Optical Magnetism. First, the notation of nonlinear optics must be generalized to include mixtures of fields. There are two possible material responses, polarization and magnetization, as well as two possible fields, electric and magnetic, for each order of the interaction. This means, for example, that at second order there are 8 possible interactions:

$$\begin{array}{ll} P = \chi EE & M = \chi EE \\ P = \chi EH & M = \chi EH \\ P = \chi HE & M = \chi HE \\ P = \chi HH & M = \chi HH \end{array}$$

Table E.1 All possible second order effects

It can be seen immediately that each χ must have different units in order for the equations to be true. It is necessary to keep track of them very carefully by identifying every other input in the equation. We must also keep track of the frequency of the interaction as is typical in nonlinear optics. Sum frequency generation of an EH type would read

$$P_i(\omega_n + \omega_m) = \varepsilon_0 D \chi_{ijk}^{(P;EH)}(\omega_n + \omega_m; \omega_n, \omega_m) E_j(\omega_n) H_j(\omega_m) \tag{E.1}$$

In this notation the superscript $(P;em)$ indicates that the result of the interaction is a polarization, the first field to act is an electric field, and the second field to act is a magnetic field. D is the degeneracy, the number of distinct combinations of frequencies ω_n and ω_m.

Time-dependent polarizations and magnetizations are the sources of radiation. In order to find the radiation due to any source the wave equation for the electromagnetic fields must be solved. The case of nonlinear response requires solving the wave equation with nonlinear sources which typically involves solving Eq. (1.44). This is not sufficient for

our discussion because (1.44) does not contain magnetization as a source. To include it a procedure similar to that of Sec. 1.3 is used but without the assumption that the medium is non-magnetic, $\vec{B} = \mu_0 \vec{H}$. The general wave equations for all possible nonlinear sources in a lossless, dispersionless medium are

$$\nabla^2 \vec{E} - \frac{\varepsilon^{(1)}}{c^2} \frac{\partial^2 \vec{E}}{\partial t^2} = \frac{1}{\varepsilon_0 c^2} \left(\frac{\partial^2 \vec{P}^{NL}}{\partial t^2} + \nabla \times \frac{\partial \vec{M}}{\partial t} \right) \tag{E.2}$$

$$\nabla^2 \vec{H} - \frac{\mu_0 \mu^{(1)}}{c^2} \frac{\partial^2 \vec{H}}{\partial t^2} = -\frac{1}{\varepsilon_0 c^2} \nabla \times \frac{\partial \vec{P}}{\partial t} + \frac{\mu_0}{c^2} \frac{\partial^2 \vec{M}^{NL}}{\partial t^2} \tag{E.3}$$

We are only interested in the nonlinear response and since the wave equations are linear in the fields, only nonlinear sources need to be considered.

We specialized to the problem of one dimensional propagation along the $\hat{z}$ direction as a plane wave allowing the simplification

$$\nabla^2 \to \frac{\partial^2}{\partial z^2} \tag{E.4}$$

We also consider only second order processes, limiting the problem to three frequencies and two input fields. The fields are written

$$E_i^{(\omega_1)}(z,t) = \frac{1}{2} \left[E_{1i}(z) e^{i(\omega_1 t - k_1 z)} + c.c. \right] \tag{E.5}$$

$$E_j^{(\omega_2)}(z,t) = \frac{1}{2} \left[E_{2j}(z) e^{i(\omega_2 t - k_2 z)} + c.c. \right] \tag{E.6}$$

$$E_k^{(\omega_3)}(z,t) = \frac{1}{2} \left[E_{3k}(z) e^{i(\omega_3 t - k_3 z)} + c.c. \right] \tag{E.7}$$

$$H_i^{(\omega_1)}(z,t) = \frac{1}{2} \left[H_{1i}(z) e^{i(\omega_1 t - k_1 z)} + c.c. \right] \tag{E.8}$$

$$H_j^{(\omega_2)}(z,t) = \frac{1}{2} \left[H_{2j}(z) e^{i(\omega_2 t - k_2 z)} + c.c. \right] \tag{E.9}$$

$$H_k^{(\omega_3)}(z,t) = \frac{1}{2} \left[H_{3k}(z) e^{i(\omega_3 t - k_3 z)} + c.c. \right] \tag{E.10}$$

where the first subscript of E_{1i} indicates the frequency and the second is an index that can take any of the cartesian directions. The nonlinear sources are defined similar to (E.1) by

$$\left[P_1^{NL}(z,t)\right]_i = \chi_{ijk}^{(P;EH)} E_{3j}(z) H_{2k}^*(z) e^{i[(\omega_3-\omega_2)t-(k_3-k_2)z]} + c.c. \tag{E.11}$$

$$\left[M_1^{NL}(z,t)\right]_i = \chi_{ijk}^{(M;EH)} E_{3j}(z) H_{2k}^*(z) e^{i[(\omega_3-\omega_2)t-(k_3-k_2)z]} + c.c. \tag{E.12}$$

$$\vdots$$

where $\omega_1 = \omega_3 - \omega_2$.

Plugging these fields into the wave equations (E.3) we find the ith component of electric field. The Laplacian, taking the direction of propagation to be $\hat{z}$, becomes

$$\nabla E_{1i}(z,t) = \frac{d^2}{dz^2} E_{1i}(z,t) = \frac{1}{2}\frac{d^2}{dz^2}\left[E_{1i}(z)e^{i(\omega_1 t - k_1 z)} + c.c.\right] \tag{E.13}$$

We assume the amplitude of the wave does not vary on the time scale of one optical cycle allowing us to make the slowly varying amplitude approximation

$$k_1 \frac{dE_{1i}}{dz} \gg \frac{d^2 E_{1i}}{dz^2} \tag{E.14}$$

simplifying the Laplacian to

$$\nabla^2 E_{1i} = -\frac{1}{2}\left[k_1^2 E_{1i}(z) + 2ik_1 \frac{dE_{1i}}{dz}\right] e^{i(\omega_1 t - k_1 z)} + c.c. \tag{E.15}$$

plugging in the nonlinear sources and realizing that $\frac{\omega_1^2 \varepsilon^{(1)}}{c^2} = k_1^2$, $\omega_3 - \omega_2 = \omega_1$, $e^{i\omega_1 t}$ is in each term, and dropping the complex conjugates results in the final coupled mode equation for E_{1i}

$$\frac{dE_{1i}}{dz} = \frac{1}{\varepsilon_0 c^2}\left[-\frac{i\omega_1^2}{k_1}\chi_{ijk}^{(P;EH)} E_{3j} H_{2k}^* e^{-i(k_3-k_2-k_1)z} - \varepsilon_{ijk} e^{ik_1 z}\partial_j \frac{\omega_1}{k_1}\chi_{klm}^{(M;EH)} E_{3l} H_{2m}^* e^{-i(k_3-k_2)z}\right] \tag{E.16}$$

similar equations can be found for E_{2j}, E_{3k}, H_{1i}, H_{2j}, and H_{3k}.

Specializing to the case discussed in Chapter 2 in which the incoming wave is polarized along $\hat{x}$ we can simplify further. The electric field must be E_x, the magnetic field must be H_y, and since the only spatial dependences of the waves are in the $\hat{z}$ direction, the ∇ of the

curl must simplify to $\frac{\partial}{\partial z}$. Eq. (E.16) simplifies to

$$\frac{dE_{1i}}{dz} = \frac{1}{\varepsilon_0 c^2}\left[-\frac{i\omega_1^2}{k_1}\chi_{ijk}^{(P;EH)}E_{3j}H_{2k}^{*}e^{-i(k_3-k_2-k_1)z} + \varepsilon_{izk}\chi_{kxy}^{(M;EH)}\frac{i\omega_1(k_3-k_2)}{k_1}E_{3x}H_{2y}^{*}e^{-i(k_3-k_2-k_1)z}\right] \tag{E.17}$$

This equation combined with the other five coupled mode equations for E_{2j}, E_{3k}, H_{1i}, H_{2j}, and H_{3k} can be solved to yield the spatial dependence of a general second order process for nonlinear magnetizations and polarizations.

Bibliography

[1] S. L. Oliveira and S. C. Rand, "Intense nonlinear magnetic dipole radiation at optical frequencies:molecular scattering in a dielectric liquid," *Physical Review Letters*, vol. 98, no. 093901, pp. 1–4, 2007.

[2] S. C. Rand, W. M. Fisher, and S. L. Oliveira, "Optically induced magnetization in homogeneous undoped dielectric media," *Journal of the Optical Society of America B*, vol. 25, no. 7, pp. 1106–1117, 2008.

[3] J. C. Maxwell, "A dynamical theory of the electromagnetic field," *Proceedings of the Royal Society of London*, vol. 13, pp. 531–536, 1865.

[4] H. A. Lorentz, "Versuch einer theorie der electrischen und optischen erscheinungen in bewegten korpern," *Teubner*, 1906.

[5] L. D. Landau, E. M. Lifshitz, and L. P. Pitaevskii, *Electrodynamics of Continuous Media*. Headington Hill Hall Oxford OX3 0BW, England: Pergamon Press, 1984.

[6] G. R. Fowles, *Introduction to Modern Optics*. 31 East 2nd Street, Mineola, NY 11501: Dover, 1975.

[7] R. W. Boyd, *Nonlinear Optics*. 30 Corporate Drive Suite 400, Burlington, MA 01803: Elsevier, 2008.

[8] C. W. P. P. A. Franken, A. E. Hill and G. Weinreich, "Generation of optical hamonics," *Physical Review Letters*, vol. 7, no. 5, pp. 118–119, 1961.

[9] G. B. Arfken and H. J. Weber, *Mathematical Methods for Physicists*. 525 B Street, Suite 1900, San Diego, CA 92101-4495: Harcourt Academic Press, 2001.

[10] D. J. Griffiths, *Introduction to Electrodynamics*. Upper Sadle River, New Jersey 07458: Prentice Hall, 1999.

[11] J. Jackson, *Classical Electrodynamics*. 111 River Street Hoboken, NJ 07030-5774: John Wiley & Sons, Inc., 1999.

[12] M. P. Wolfgang K. H. Panofsky, *Classical Electricity and Magnetism*. 31 East 2nd Street, Mineola, NY 11501: Dover, 2005.

[13] K. E. Oughstun and R. A. Albanese, "Magnetic field contribution to the lorentz model," *Journal of the Optical Society of America A*, vol. 23, no. 7, pp. 1751–1756, 2006.

[14] M. Born and E. Wolf, *Principles of Optics*. Cambridge: Cambridge University Press, 1999.

[15] W. M. Fisher and S. C. Rand, "Light-induced dynamics in the lorentz oscillator model with magnetic forces," *Physical Review A*, vol. 82, p. 013802, 2010.

[16] D. W. Jordan and P. Smith, *Nonlinear Ordinary Differential Equations*. Oxford: Oxford University Press, 2007.

[17] M. Cartmell, *Introduction to linear, parametric, and nonlinear vibrations*. New York: Chapman and Hall, 1990.

[18] E. I. Butikov, "Parametric resonance," *Computing in Science and Engineering*, vol. 1, no. 3, pp. 76–83, 1999.

[19] R. N. Jazar, M. Mahinfalah, N. Mahmoudian, and M. A. Rastgaar, "Energy-rate method and stability chart of parametric vibrating systems," *J. of the Braz. Soc. of Mech. Sci. and Eng.*, vol. XXX, no. 3, pp. 182–188, 2008.

[20] D. B. Batchelor, "Parametric resonance of systems with time-varying dissipation," *Appl. Phys. Lett.*, vol. 29, no. 5, pp. 280–281, 1976.

[21] A. H. Nayfeh and D. T. Mook, *Nonlinear Oscillations*. New York: John Wiley & Sons, Inc., 1979.

[22] S. C. Rand, "Quantum theory of coherent transverse optical magnetism," *JOSA B*, vol. 26, p. B120, 2009.

[23] P. S. P. J. P. van der Ziel and L. D. Malmstrom, "Optically-induced magnetization resulting from the inverse faraday effect," *Physical Review Letters*, vol. 15, pp. 190–193, 1965.

[24] E. Merzbacher, *Quantum Mechanics*. 111 River Street Hoboken, NJ 07030: Wiley, 1998.

[25] M. C. F. E. J. K. R. W. Cahn, Bernhard Ilschner and K. H. J. Buschow, eds., *Encyclopedia of Material: Science and Technology*. Headington Hill Hall Oxford OX3 0BW, England: Pergamon Press, 2001.

[26] C. F. S. C. H. F. Courvoisier, V. Bouton and J. P. Wolf, "Plasma formation dynamics within a water microdroplet on femtosecond time scales," *Optics Letters*, vol. 28, pp. 206–208, 2003.

[27] W. M. Fisher and S. C. Rand, "Dependence of optical magnetic response on molecular structure," *Journal of Luminescence*, vol. 128, pp. 1407–1409, 2009.

[28] M. Tonouchi, "Cutting-edge terahertz technology," *Nature Photonics*, vol. 1, pp. 97–105, 2007.

[29] R. W. Hamming, *Numerical Methods for Scientists and Engineers*. 31 East 2nd Street, Mineola, NY 11501: Dover, 1986.

[30] A. C. B. G. K. Ottman, H. F. Hofmann and G. A. Lesieutre, "Adaptive piezoelectric energy harvesting circuit for wireless remote power supply," *IEEE Trans. Power Electron*, vol. 17, p. 669, 2002.

[31] R. Nubling and J. A. Harrington, "Optical properties of single-crystal sapphire fibers," *Applied Optics*, vol. 36, p. 5934, 1997.

[32] D. Batani, R. Jafer, M. Veltcheva, R. Dezulian, O. Lundh, F. Lindau, A. Persson, K. Osvay, C.-G. Wahlstrm, D. C. Carroll, P. McKenna, A. Flacco, and V. Malka, "Effects of laser prepulses on laser-induced proton generation," *New Journal of Physics*, vol. 12, no. 4, p. 045018, 2010.

[33] V. V. Bolotin, *The dynamic stability of elastic systems*. San Francisco: Holden-Day, 1964.

[34] C. S. Hsu, "On the parametric excitation of a dynamic system having multiple degrees of freedom," *Journal of Applied Mechanics*, vol. 30, pp. 367–374, 1963.

[35] Hartono and A. van der Burgh, "A linear differential equation with a time-periodic damping coefficient: stability diagram and an application," *Journal of Engineering Mathematics*, vol. 49, pp. 99–112, 2004. 10.1023/B:ENGI.0000017475.20596.cb.

[36] J. Hebling, K.-L. Yeh, M. C. Hoffmann, B. Bartal, and K. A. Nelson, "Generation of high-power terahertz pulses by tilted-pulse-front excitation and their application possibilities," *J. Opt. Soc. Am. B*, vol. 25, pp. B6–B19, Jul 2008.

[37] C. A. Brau, *Modern problems in classical electrodynamics*. New York: Oxford University Press, 2004.

[38] M. Kerker, *The scattering of light and other electromagnetic radiation*. New York: Academic Press, 1969.